UNIVERSITY OF OKLAHOMA

GRADUATE COLLEGE

MODELING AND COMPENSATION OF CDMA POWER AMPLIFIERS

A Dissertation

SUBMITTED TO THE GRADUATE FACULTY

in partial fulfillment of the requirements for the

degree of

Doctor of Philosophy

By

John Walter Wustenberg
Norman, Oklahoma
2001

UMI Number: 3004890

MODELING AND COMPENSATION OF CDMA POWER AMPLIFIERS

A Dissertation APPROVED FOR THE
SCHOOL OF ELECTRICAL AND COMPUTER ENGINEERING

BY

Marilyn Breen

Arthur M. Breipohl

ACKNOWLEDGMENTS

Many people have provided me with assistance during my long journey to acquire a doctorate. I want to express my gratitude to them for all their help. I would like to begin by thanking my graduate committee members: Drs. Marilyn J. Breen, Arthur M. Breipohl, John Y. Cheung, Fred N. Lee, and J.R. Cruz. They deserve my thanks, not just for serving on my graduate committee, but for all that I have learned from them during the years I have been their student. My committee chairman and advisor, Dr. Cruz, deserves special recognition. Dr. Cruz has gone out of his way to provide me with financial support during my acquisition of two advanced degrees. Thank you Dr. Cruz for all the too numerous to mention things you have done for me during our acquaintance.

I want to thank Danny Pinckley, Motorola Inc., for providing the data sets used to develop and validate my nonlinear amplifier model. Danny spent long hours setting up the test equipment and taking the measurements needed to prepare the data sets.

I also want to thank Helen Jun Xing, a fellow graduate student, for writing the IS-2000 forward link simulator used to measure the performance of my compensation scheme. Helen's simulator allowed me to test the performance under actual operating conditions – or at least as close to actual operating conditions as you can get without access to a cellular telephone base station.

Most of all, I want to express my love and gratitude to my parents, Walter J. and Peggy L. Wustenberg. I would not be where I am today without the love, support, and encouragement they provided me throughout my life. These words are similar to those I

wrote in my 1989 thesis, however, they are even more true today than then. For all they have given me, I want to say, I love you!

TABLE OF CONTENTS

LIST OF TABLES

LIST OF ILLUSTRATIONS

ABSTRACT

The efficient operation of a linear high power amplifier (HPA) often results in enhancing its inherent *nonlinear* behavior. This nonlinear behavior causes co-channel and adjacent channel interference due to intermodulation distortion and spectral regrowth of the sidebands. These deleterious effects, especially the sideband regrowth, are of great concern in present second generation cellular telephone systems such as IS-95 and will have an even greater impact in the new wideband third generation cellular telephone systems such as IS-2000.

Compensation (linearization) allows an HPA to operate efficiently while mitigating the effects of its nonlinear behavior. A digital baseband predistorter based on the "fixed point" approach (FPPD) is developed to compensate the wideband HPA in a CDMA cellular telephone system. The FPPD incorporates a memoryless nonlinear HPA model derived from samples of the HPA's input and output signals to overcome shortcomings in previous FPPDs. The FPPD's performance is evaluated using an IS-2000 forward link simulator. The link performance for a *perfectly* linear HPA, nonlinear HPA, and compensated HPA are compared. The FPPD's effect on reducing sideband regrowth, as compared to just backing off the HPA's input signal, is also examined.

CHAPTER 1 INTRODUCTION

A linear high power amplifier (HPA) is a critical component in many modern mobile wireless systems because it has such a major impact on a system's overall performance. An HPA's *nonlinear* behavior is one of the most significant factors in determining this performance. This chapter begins by discussing the motivation to model and compensate for an HPA's nonlinear behavior. The characteristics, desired and undesired, of an HPA operating in a mobile wireless system are then examined. The chapter concludes with a list of the research objectives that are the subject of this dissertation.

1.1 RESEARCH MOTIVATION

The impetus for the research underlying this dissertation is the need to accurately model, and eventually compensate for, the nonlinear behavior of an HPA located in a cellular telephone base station utilizing CDMA (code division multiple access). CDMA relies on specialized codes to provide multiple users simultaneous access to a communications channel. An introductory tutorial focusing on the implementation of CDMA for the North American cellular telephone market is given in [1]. The present standard for North American based CDMA cellular telephone systems is IS-95 (a second-generation wireless technology). IS-95 is a digital standard in which the spectrum of a user's narrowband signal is spread (widened) by multiplying it by a wideband signal (spreading code). In this context, narrowband and wideband indicate the relative bandwidth of each signal vis-à-vis the other. The spreading code used in the forward link, i.e., the base station to mobile subscriber link, consists of 64 "chips" having a chip rate 64 times greater than the original symbol rate [2]. There are several national and international standards being proposed for the next generation of wireless technologies. The International Telecommunication Union's (ITU's) new third generation global standard for mobile telecommunications is IMT-2000. IS-2000 is a third-generation wireless technology proposal submitted to the ITU that is backward compatible with IS-95. W-CDMA (wideband CDMA) is another third generation standard being offered to the ITU.

The development of a wideband compensated HPA for an IS-95 system is important for a number of reasons – regulatory, financial, and technical. This development is even more crucial for the proposed third generation systems. For example, the forward link in an IS-95 system is approximately 1.23 MHz wide [1], whereas many of the proposed third generation systems employ channels having greater than 4 MHz bandwidth.

1.2 HPA OPERATING CHARACTERISTICS

The last decade has seen an explosive growth in the demand for mobile wireless services such as cellular telephone. Once a novelty, a cellular telephone handset is now a common sight in the hands of many ordinary people. This tremendous growth in the number of users is coupled with the delivery of new services requiring higher data rates. These new services can provide high-speed data traffic such as multimedia content in addition to standard voice traffic. Accommodating all these users and providing higher data rates results in the need to make the most efficient use of currently available frequency allocations.

Constant envelope modulation methods, such as frequency modulation (FM) and phase modulation (PM), have been used for many years in mobile wireless systems and have the advantage of allowing the use of a nonlinear RF power amplifier. These constant envelope modulation methods are, however, spectrally inefficient. Modulation methods having a varying envelope such as the filtered $\pi/4$-shifted DQPSK (differential quadrature phase-shift keying) used by the North American digital cellular telephone system and M-QAM (M-ary quadrature amplitude modulation), and multiple access methods such as CDMA when modulated using filtered QPSK (quadrature phase-shift keying), are more spectrally efficient than the constant envelope modulation methods. Unfortunately, a linear HPA must be used to preserve the amplified signal's varying envelope. Failure to use a linear HPA causes co-channel and adjacent channel interference due to intermodulation distortion (IMD) and spectral regrowth of the sidebands [3]. This failure in a base station utilizing CDMA also leads to code domain interference [4]. Throughout the remainder of this dissertation, the term HPA stands for a linear high power amplifier unless the context indicates otherwise, e.g., an ultra-linear HPA.

An HPA's power efficiency is lower than that of a nonlinear RF power amplifier. Power efficiency is important in mobile and portable equipment where battery capacity is often limited as well as a base station where heat dissipation is a concern [5]. Driving the input signal harder, in effect, operating the HPA in its saturation region increases an

HPA's power efficiency. This efficient operation of an HPA often results in enhancing its inherent nonlinear behavior. Although an HPA having nonlinear behavior is an apparent oxymoron, even the most ultra-linear HPA exhibits some nonlinear behavior. This nonlinear behavior manifests itself by causing IMD and sideband regrowth as previously described. These deleterious effects, especially the sideband regrowth, are of great concern in present second-generation cellular telephone systems such as IS-95 and the new wideband third generation cellular telephone systems such as IS-2000.

An HPA's input signal in a spectrally efficient system, such as IS-95 or IS-2000, is characterized by a high peak-to-average power ratio. An IS-95 system, for instance, has a peak-to-average power ratio of about 10 to 12 dB [6]. This results in poor power efficiency if the HPA operates in the linear region of its gain characteristic even during periods of peak input signal amplitude. For example, an HPA operating totally in the linear region of its gain characteristic would need a peak power rating of over 160 watts to produce 20 watts of average output power for an input signal with a peak-to-average power ratio of 9 dB [6]. Driving the input signal harder to increase the power efficiency, thereby clipping the input signal's peak amplitudes by operating in the saturation region of the HPA's gain characteristic, results in the nonlinear behavior described above. Consequently, the input signal is usually backed off to allow the HPA to operate at a point significantly backed off from its 1 dB compression point, thus reducing the HPA's nonlinear behavior [6]. This reduction in nonlinear behavior is achieved at the expense of lower power efficiency – a vicious circle.

One possible solution to this quandary is to use an ultra-linear HPA. An ultra-linear HPA is not as inherently nonlinear as a normal HPA. An ultra-linear HPA is, however, more difficult to design than a similarly rated HPA and therefore much more expensive. The tremendous growth in the number of cellular telephone users results in the need to keep the price of each HPA as low as possible because additional base stations must be added to a cellular telephone system by creating new cells and/or splitting larger cells into smaller cells to accommodate the additional users. Thus, a better solution may be to use a less expensive HPA instead of an ultra-linear HPA and then compensate for the HPA's nonlinear behavior. Compensation (linearization) allows the HPA to operate efficiently while mitigating the effects of its nonlinear behavior. An essential component of many compensation schemes is the ability to accurately model an HPA's nonlinear behavior.

An HPA's nonlinear behavior is often characterized by its gain compression (AM/AM conversion) and phase distortion (AM/PM conversion) [7]. This characterization is premised on the HPA's nonlinear behavior being only a function of the HPA's input signal's complex envelope magnitude. These characteristics are often derived with a network analyzer using a continuous wave (CW) power sweep [3]. The HPA's measured AM/AM conversion and AM/PM conversion then become the basis for a nonlinear model that predicts the HPA's output signal given its input signal [3], [7]-[8]. An example of a solid-state HPA's AM/AM conversion and AM/PM conversion measured at 1950 MHz using a network analyzer is shown in Figs. 1 and 2, respectively.

Once an HPA's nonlinear behavior is modeled, that information can be used by a compensation scheme to mitigate the HPA's nonlinear behavior.

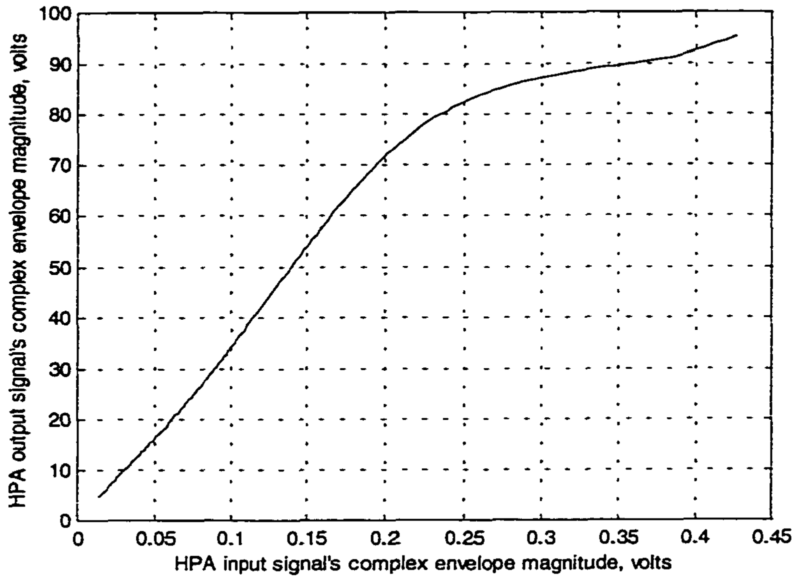

Fig. 1. Solid-state HPA's AM/AM conversion measured at 1950 MHz.

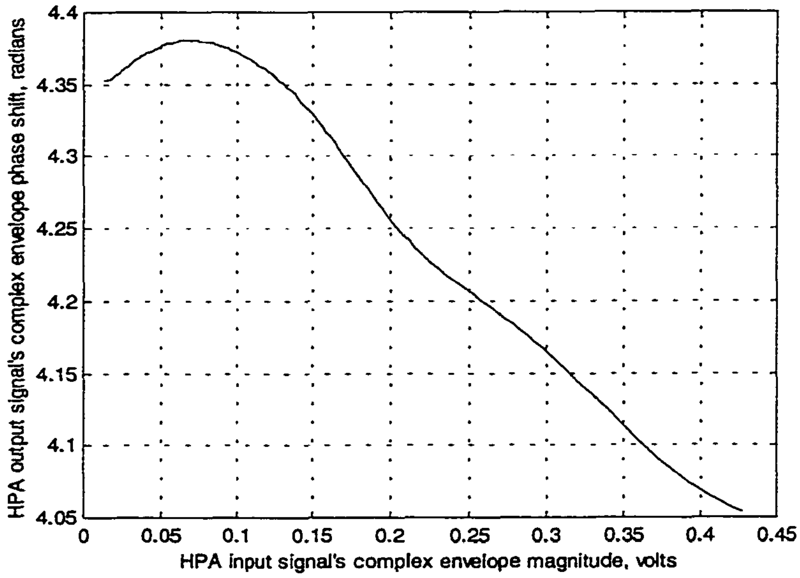

Fig. 2. Solid-state HPA's AM/PM conversion measured at 1950 MHz.

Compensation schemes can be broadly grouped into two categories. The first category includes those schemes wherein the HPA's input signal retains its varying envelope. In one such technique known as feedforward linearization, the IMD generated by the HPA's nonlinear behavior is isolated and then subtracted from the HPA's distorted output signal to yield a nondistorted output signal. In another technique known as predistortion, the HPA's input signal is distorted in such a manner that the resulting amplified output signal is essentially IMD free. The second category includes those techniques that provide the HPA with an input signal having a constant envelope so that the HPA's nonlinear behavior is no longer a factor. In one such technique two constant envelope signals having varying phase are formed from the original varying envelope input signal, each constant envelope signal is then amplified by a separate HPA, and the two amplified signals are finally combined to form a nondistorted, amplified replica of the original input signal (LINC) [9]. Any particular compensation technique such as predistortion can have many different variations.

1.3 RESEARCH OBJECTIVES

The ultimate objective of this research is to design a compensator for the wideband HPAs used in CDMA cellular telephone systems such as IS-95 and IS-2000. To realize this ultimate objective three other objectives must be achieved. The first objective is to derive a simple yet accurate model of an HPA's nonlinear behavior. Ideally, this model will use the HPA's actual modulated input and output signals instead of network analyzer data to determine the model's parameters. The next objective is to design a compensator that incorporates this nonlinear model. The final objective is to evaluate the compensator's performance by incorporating it into an IS-2000 forward link simulator. The compensator's performance is to be evaluated by comparing the forward link performance obtained using an uncompensated HPA to the forward link performance obtained using the compensator to linearize the HPA.

CHAPTER 2 NONLINEAR HPA MODELS

Unlike a linear time-invariant (LTI) system having an input/output relationship completely described by its transfer function (or unit impulse response), a nonlinear time-invariant (NLTI) system does not have such a simple representation. Consequently, an NLTI system's input/output relationship, e.g., an HPA's nonlinear behavior, is often described using a nonlinear model to predict the system's output signal given its input signal. Nonlinear models can be broadly grouped into two categories: memory models and memoryless models. In a memory model the present value of the output signal may depend not only on the present value of input signal but also on past values of the input signal. The present value of the output signal in a memoryless model, however, depends only on the present value of the input signal. This chapter begins by examining a memory model based on Volterra series. Various memoryless models are then examined and the chapter concludes with a discussion of the tapped-delay-line (TDL) model – a modified memoryless model that incorporates memory effects.

2.1 VOLTERRA SERIES

An LTI system's input/output relationship is given by the convolution integral

$$y(t) = x(t) * h(t) = \int_{-\infty}^{+\infty} h(\tau)x(t-\tau)d\tau\,, \tag{1}$$

where $x(t)$ is the continuous-time input signal, $y(t)$ is the continuous-time output signal, and $h(t)$ is the unit impulse response of the LTI system. An LTI system's output signal can be determined for any given input signal once its impulse response is known [10]. A memoryless NLTI system's input/output relationship can be expressed by a Taylor series expansion, assuming the series converges, as

$$y(t) = \sum_{n=0}^{\infty} c_n x^n(t), \tag{2}$$

where c_n are the Taylor series' coefficients [10]. The Volterra series is an extension of (2) that describes the input/output relationship of an NLTI system as

$$\begin{aligned} y(t) = h_0 &+ \int_{-\infty}^{+\infty} h_1(\tau_1)x(t-\tau_1)d\tau_1 + \int_{-\infty}^{+\infty}\int_{-\infty}^{+\infty} h_2(\tau_1,\tau_2)x(t-\tau_1)x(t-\tau_2)d\tau_1 d\tau_2 + \\ &\int_{-\infty}^{+\infty}\int_{-\infty}^{+\infty}\int_{-\infty}^{+\infty} h_3(\tau_1,\tau_2,\tau_3)x(t-\tau_1)x(t-\tau_2)x(t-\tau_3)d\tau_1 d\tau_2 d\tau_3 + \cdots, \end{aligned} \tag{3}$$

where $h_n(\tau_1,\ldots,\tau_n)$ are the system's Volterra kernels [10]. The Volterra kernel h_0, if it exists, is the system's output signal in the absence of an input signal. The Volterra kernels are a generalization of an LTI system's unit impulse response since they allow determination of the NLTI system's output signal for certain input signals [11]. There is no loss of generality if the Volterra kernels are assumed to be symmetric functions of their arguments [11]. A Volterra kernel is symmetric if it remains unchanged regardless of which one of the $n!$ permutations of its argument $(\tau_1,\tau_2,\ldots,\tau_n)$ is used, e.g., $h_2(\tau_1,\tau_2) = h_2(\tau_2,\tau_1)$ [10].

Using a Volterra series to model an NLTI system with memory is constrained by convergence of the series, as is the use of a Taylor series to model a memoryless NLTI system. This occurs since the Volterra series is essentially a Taylor series that incorporates memory. As a result, a nonlinear HPA model based on a Volterra series representation may not exist for all input signals since the Volterra series may not converge for one or more input signals. Another limitation of Volterra series is the difficulty in measuring the Volterra kernels of a general NLTI system [10]. The Volterra series model thus has limited suitability for use in simulations involving many operations due to these and other limitations [12].

A Volterra series is an infinite series of multidimensional integrations. To be of practical use, however, a Volterra series must be expressible in terms of a finite series of summations with each summation having a finite number of terms, i.e., a truncated Volterra series. In [13], Hermann derives a truncated Volterra series representation of a magnetic saturation recording channel by exploiting the physical characteristics of the channel and its input signal. Hermann's model will serve as the basis for a truncated Volterra series model of a nonlinear HPA – a bandpass system – even though a magnetic saturation recording channel is a baseband NLTI system.

The following description of Hermann's model uses a slightly modified version of the notation found in [13]. Hermann exploits the fact that a magnetic saturation recording channel's output signal is a function of only a limited number L of consecutive input data symbols. The input data symbols are a bipolar sequence $x_k = \pm 1$ since the write current polarity changes only at time kT, $k = 0, \pm 1, \pm 2, \cdots$. The channel's output signal $y(t)$, also known as the readback signal, is sampled to yield what Hermann calls the signal chips $y(i,\tau) = y(t = iT + \tau)$, $\tau \in [0,T)$. Since a signal chip is a function of only $L = u + v + 1$ input data symbols $(x_{i-u}, \ldots, x_{i+v})$, the signal chip can be represented by the truncated Volterra series

$$y[i,\tau]=f^{(0)}(\tau)+\sum_{k_1=u}^{-v}x_{i-k_1}f_{k_1}^{(1)}(\tau)+\sum_{k_1=u}^{-v+n-1}\sum_{k_2=k_1-1}^{-v+n-2}\cdots\sum_{k_n=k_{n-1}-1}^{-v}x_{i-k_1}x_{i-k_2}\cdots x_{i-k_n}f_{k_1,\ldots,k_n}^{(n)}(\tau)+\cdots$$
$$\cdots+x_{i-u}x_{i-u+1}\cdots x_{i+v}f_{u,u-1,\ldots,-v}^{(L)}(\tau), \tag{4}$$

where $f_{\ldots}^{(n)}(\tau)$, $\tau=[0,T)$ are the system's Volterra kernel chips.

Hermann notes that the signal chip $y[i,\tau]$ is defined for $i=\cdots,-1,0,1,\cdots$ and is non-zero only on the interval $\tau=[0,T)$. The channel's output signal $y(t)$ can thus be written as a summation of signal chips given by

$$y(t)=\sum_{i=-\infty}^{+\infty}y[i,t-iT], \tag{5}$$

where each signal chip is shifted by iT. There is no $f^{(0)}(\tau)$ kernel chip in a magnetic saturation recording channel so (5) can be written as

$$y(t)=\sum_{k}x_k c^{(1)}(t-kT)+\sum_{k}\sum_{d_1=1}^{u+v-n+2}\cdots\sum_{d_{n-1}=d_{n-2}+1}^{u+v}x_k x_{k-d_1}\cdots x_{k-d_{n-1}}c_{d_1,\ldots,d_{n-1}}^{(n)}(t-kT)+\cdots$$
$$\cdots+\sum_{k}x_k x_{k-1}\cdots x_{k-u-v}c_{1,\ldots,u+v}^{(L)}(t-kT), \tag{6}$$

where

$$c^{(1)}(t)=\sum_{k=-v}^{u}f_k^{(1)}(t-kT), \tag{7}$$

and

$$c_{d_1,\ldots,d_{n-1}}^{(n)}(t)=\sum_{k=-v}^{u-d_{n-1}}f_{k+d_{n-1},\ldots,k+d_1,k}^{(n)}(t-kT),\quad n=2,\ldots,L. \tag{8}$$

The system, therefore, has a total of 2^{L-1} Volterra kernels $c_{\ldots}^{(n)}(t)$ that are derived from the kernel chips $f_{\ldots}^{(n)}(\tau)$. Hermann does not show how he derives his equations from the fundamental Volterra series equation shown in (3). The following paragraphs provide a detailed derivation of Hermann's equations using (3) and the physical characteristics of a magnetic saturation recording channel and its input signal.

The input data symbols are a bipolar sequence that changes polarity only at discrete times so the system's input signal can be written as

$$x(t)=\sum_{k} x_k p(t-kT), \tag{9}$$

where $p(t)=u(t)-u(t-T)$ and $u(t)$ is the unit step function. The input signal (9) allows the Volterra series (3) to be written as

$$\begin{aligned} y(t) = h_0 &+ \sum_{k_1} x_{k_1} \int_{t-(k_1+1)T}^{t-k_1T} h_1(\tau_1)\,d\tau_1 + \\ &\sum_{k_1}\sum_{k_2} x_{k_1}x_{k_2} \int_{t-(k_2+1)T}^{t-k_2T} \int_{t-(k_1+1)T}^{t-k_1T} h_2(\tau_1,\tau_2)\,d\tau_1 d\tau_2 + \cdots \\ &\cdots + \sum_{k_1}\cdots\sum_{k_n} x_{k_1}\cdots x_{k_n} \int_{t-(k_n+1)T}^{t-k_nT} \cdots \int_{t-(k_1+1)T}^{t-k_1T} h_n(\tau_1,\ldots,\tau_n)\,d\tau_1\cdots d\tau_n + \cdots . \end{aligned} \tag{10}$$

If $y(t)$ is sampled at $t=iT+\tau$, where $\tau=[0,T)$, (10) becomes

$$\begin{aligned} y[i,\tau] = h_0 &+ \sum_{k_1} x_{k_1} \int_{(i-k_1-1)T+\tau}^{(i-k_1)T+\tau} h_1(\tau_1)\,d\tau_1 + \\ &\sum_{k_1}\sum_{k_2} x_{k_1}x_{k_2} \int_{(i-k_2-1)T+\tau}^{(i-k_2)T+\tau} \int_{(i-k_1-1)T+\tau}^{(i-k_1)T+\tau} h_2(\tau_1,\tau_2)\,d\tau_1 d\tau_2 + \cdots \\ &\cdots + \sum_{k_1}\cdots\sum_{k_n} x_{k_1}\cdots x_{k_n} \int_{(i-k_n-1)T+\tau}^{(i-k_n)T+\tau} \cdots \int_{(i-k_1-1)T+\tau}^{(i-k_1)T+\tau} h_n(\tau_1,\ldots,\tau_n)\,d\tau_1\cdots d\tau_n + \cdots . \end{aligned} \tag{11}$$

Recall that the system's memory length is $L=u+v+1$ input data symbols. In other words, only the previous u input data symbols, the present input data symbol, and the future v input data symbols contribute to the output signal. Hence, (11) can be written as

$$
\begin{aligned}
y[i,\tau] = h_0 + \sum_{k_1=u}^{-v} x_{i-k_1} \int_{(k_1-1)T+\tau}^{k_1T+\tau} h_1(\tau_1)d\tau_1 + \\
\sum_{k_1=u}^{-v}\sum_{k_2=u}^{-v} x_{i-k_1}x_{i-k_2} \int_{(k_2-1)T+\tau}^{k_2T+\tau}\int_{(k_1-1)T+\tau}^{k_1T+\tau} h_2(\tau_1,\tau_2)d\tau_1 d\tau_2 + \cdots \\
\cdots + \sum_{k_1=u}^{-v}\sum_{k_2=u}^{-v}\cdots\sum_{k_L=u}^{-v} x_{i-k_1}\cdots x_{i-k_L} \int_{(k_L-1)T+\tau}^{k_LT+\tau}\cdots\int_{(k_1-1)T+\tau}^{k_1T+\tau} h_L(\tau_1,\ldots,\tau_L)d\tau_1\cdots d\tau_L .
\end{aligned}
\tag{12}
$$

The bipolar nature of the input data symbols is the key to reducing the complexity of (12). For any positive integer m and input data symbol $x_k = \pm 1$, a product of input data symbols having the same index is simplified by noting that $(x_k)^{2m} = 1$ and $(x_k)^{2m+1} = x_k$. This property allows a sequence of input data symbols containing symbols having the same index to be simplified as shown in Table 1.

Original Sequence	Simplified Sequence
$x_{i-2}x_{i+2}$	$x_{i-2}x_{i+2}$
$x_{i-2}x_ix_ix_{i+2}$	$x_{i-2}x_{i+2}$
$x_{i-2}x_{i-2}x_{i-2}x_{i+2}$	$x_{i-2}x_{i+2}$
$x_{i-2}x_ix_ix_{i+2}x_{i+2}x_{i+2}$	$x_{i-2}x_{i+2}$

Table 1. Example of input data symbol sequences that simplify to the same sequence.

The signal chip (12) is simplified by combining all terms having the same simplified input data symbol sequences into one term [14]. For example, all the input data symbol sequences in (13) simplify to $x_{i-2}x_{i+2}$. Note that the limits of integration are not shown for simplicity,

$$\int\int x_{i-2}x_{i+2}h_2(\tau_1,\tau_2)d\tau_1 d\tau_2 \tag{13a}$$

$$\int\int x_{i+2}x_{i-2}h_2(\tau_1,\tau_2)d\tau_1 d\tau_2 \tag{13b}$$

$$\iiiint x_{i-2}x_ix_ix_{i+2}h_4(\tau_1,\tau_2,\tau_3,\tau_4)d\tau_1d\tau_2d\tau_3d\tau_4 \tag{13c}$$

$$\iiiint x_{i-2}x_{i-2}x_{i-2}x_{i+2}h_4(\tau_1,\tau_2,\tau_3,\tau_4)d\tau_1d\tau_2d\tau_3d\tau_4 \tag{13d}$$

$$\int\!\!\int\!\!\int\!\!\int\!\!\int\!\!\int x_{i-2}x_ix_ix_{i+2}x_{i+2}x_{i+2}h_6(\tau_1,\tau_2,\tau_3,\tau_4,\tau_5,\tau_6)d\tau_1d\tau_2d\tau_3d\tau_4d\tau_5d\tau_6\,. \tag{13e}$$

The terms in (13) plus all the other terms in (12) that have input data symbol sequences that simplify to $x_{i-2}x_{i+2}$ are combined to yield

$$x_{i-2}x_{i+2}\begin{bmatrix} \iint h_2(\tau_1,\tau_2)d\tau_1d\tau_2 + \iint h_2(\tau_1,\tau_2)d\tau_1d\tau_2 + \cdots \\ \cdots + \iiiint h_4(\tau_1,\tau_2,\tau_3,\tau_4)d\tau_1d\tau_2d\tau_3d\tau_4 + \cdots \\ \cdots + \iiiint h_4(\tau_1,\tau_2,\tau_3,\tau_4)d\tau_1d\tau_2d\tau_3d\tau_4 + \cdots \\ \cdots + \int\!\!\int\!\!\int\!\!\int\!\!\int\!\!\int h_6(\tau_1,\tau_2,\tau_3,\tau_4,\tau_5,\tau_6)d\tau_1d\tau_2d\tau_3d\tau_4d\tau_5d\tau_6 + \cdots \end{bmatrix}. \tag{14}$$

The sum of integrals in (14) contains Volterra kernels of all orders between 2 and L. These integrals are combined to form a single Volterra kernel chip that describes the contribution of the two input data symbols x_{i-2} and x_{i+2}, independent of the other $L-2$ input data symbols, to the output signal. Using the Volterra kernel chip notation results in (14) being written as

$$x_{i-2}x_{i+2}f_{2,-2}^{(2)}(\tau). \tag{15}$$

Therefore, the terms with unique indices in (12) are the only ones that need to be generated since all other terms are simplified and combined as (13) was simplified and combined to form (15). Using only the terms with unique indices results in the signal chip (4) when (12) is written as

$$y[i,\tau]=f^{(0)}(\tau)+\sum_{k_1=u}^{-v}x_{i-k_1}f_{k_1}^{(1)}(\tau)+\sum_{k_1=u}^{-v+n-1}\sum_{k_2=k_1-1}^{-v+n-2}\cdots\sum_{k_n=k_{n-1}-1}^{-v}x_{i-k_1}x_{i-k_2}\cdots x_{i-k_n}f_{k_1,\ldots,k_n}^{(n)}(\tau)+\cdots$$
$$\cdots+x_{i-u}x_{i-u+1}\cdots x_{i+v}f_{u,u-1,\ldots,-v}^{(L)}(\tau) \tag{16}$$

by defining $h_0=f^{(0)}(\tau)$.

The following derivations show that the channel's output signal $y(t)$ can be derived from the Volterra kernels $c_{...}^{(n)}(t)$ that are derived from the Volterra kernel chips $f_{...}^{(n)}(\tau)$. Recall that $y(t)$ can be written as a summation of shifted signal chips as shown in (5) and that there is no $f^{(0)}(\tau)$ kernel chip in a magnetic saturation recording channel. This allows (4) and (5) to be combined as

$$y(t)=\sum_{i=-\infty}^{+\infty}\left[\begin{array}{l}\sum_{k_1=u}^{-v}x_{i-k_1}f_{k_1}^{(1)}(t-iT)+\sum_{k_1=u}^{-v+n-1}\sum_{k_2=k_1-1}^{-v+n-2}\cdots\sum_{k_n=k_{n-1}-1}^{-v}x_{i-k_1}\cdots x_{i-k_n}f_{k_1,\ldots,k_n}^{(n)}(t-iT)+\cdots\\ \cdots+x_{i-u}x_{i-u+1}\cdots x_{i+v}f_{u,u-1,\ldots,-v}^{(L)}(t-iT)\end{array}\right]. \tag{17}$$

Making the substitution $i=i+k_1$ into the first summation in (17) yields

$$\sum_{i=-\infty}^{+\infty}\sum_{k_1=u}^{-v}x_{i-k_1}f_{k_1}^{(1)}(t-iT)=\sum_{i=-\infty}^{+\infty}\sum_{k_1=u}^{-v}x_if_{k_1}^{(1)}(t-(i+k_1)T). \tag{18}$$

This can be simplified by defining

$$c^{(1)}(t)=\sum_{k_1=u}^{-v}f_{k_1}^{(1)}(t-k_1T), \tag{19}$$

which results in

$$c^{(1)}(t-iT)=\sum_{k_1=u}^{-v}f_{k_1}^{(1)}(t-(i+k_1)T). \tag{20}$$

The first summation in (17) can, therefore, be written as

$$\sum_{i=-\infty}^{+\infty} x_i c^{(1)}(t-iT). \tag{21}$$

The next step is to confirm that the second summation in (17) is equivalent to the second summation in (6), i.e.,

$$\begin{aligned}&\sum_{i=-\infty}^{+\infty}\sum_{k_1=u}^{-v+n-1}\sum_{k_2=k_1-1}^{-v+n-2}\cdots\sum_{k_n=k_{n-1}-1}^{-v} x_{i-k_1}x_{i-k_2}\cdots x_{i-k_n} f^{(n)}_{k_1,\ldots,k_n}(t-iT)=\\&\sum_{i=-\infty}^{+\infty}\sum_{d_1=1}^{u+v-n+2}\sum_{d_2=d_1+1}^{u+v-n+3}\cdots\sum_{d_{n-1}=d_{n-2}+1}^{u+v} x_i x_{i-d_1}\cdots x_{i-d_{n-1}} c^{(n)}_{d_1,\ldots,d_{n-1}}(t-iT).\end{aligned} \tag{22}$$

All sequences of n input data symbols having unique indices that occur within a memory length of L are generated by the two summations in (22). Therefore, proving that there is a one-to-one mapping between the terms in each summation shows equivalence of these two summations. The proof consists of letting $i=i_0$ in the second summation and showing that the two terms generated using the lower and upper summation limits in the second summation occur – only once – in the first summation. The two terms generated using the extreme values of the summation limits are the only ones used in the interest of brevity.

The first term examined in the second summation corresponds to $i=i_0$ and $d_1=1, d_2=2,\ldots, d_{n-1}=n-1$. This term can be written, using (8), as

$$\begin{aligned}&x_{i_0}x_{i_0-1}x_{i_0-2}\cdots x_{i_0-n+1}\, c^{(n)}_{1,2,\ldots,n-1}(t-i_0T)=\\&x_{i_0}x_{i_0-1}x_{i_0-2}\cdots x_{i_0-n+1}\sum_{k_n=u-n+1}^{-v} f^{(n)}_{k_n+n-1,\ldots,k_n+2,k_n+1,k_n}(t-(i_0+k_n)T).\end{aligned} \tag{23}$$

Since the term (23) also includes a summation, only the two terms generated using the lower and upper summation limits, $k_n = u-n+1$ and $k_n = -v$, respectively, are examined. Hence, (23) is written as

$$x_{i_0} x_{i_0-1} x_{i_0-2} \cdots x_{i_0-n+1} \begin{bmatrix} f^{(n)}_{u,\ldots,u-n+3,u-n+2,u-n+1}\left(t-\left(i_0+u-n+1\right)T\right)+\cdots \\ \cdots + f^{(n)}_{-v+n-1,\ldots,-v+2,-v+1,-v}\left(t-\left(i_0-v\right)T\right) \end{bmatrix}. \tag{24}$$

Setting $i = i_0 + u - n + 1$ in the first summation in (22) results in

$$\sum_{k_1=u}^{-v+n-1} \sum_{k_2=k_1-1}^{-v+n-2} \cdots \sum_{k_{n-1}=k_{n-2}-1}^{-v+1} \sum_{k_n=k_{n-1}-1}^{-v} x_{i_0+u-n+1-k_1} \cdots x_{i_0+u-n+1-k_n} f^{(n)}_{k_1,\ldots,k_n}\left(t-\left(i_0+u-n+1\right)T\right). \tag{25}$$

Note that $k_1 = u, \ldots, k_{n-2} = u-n+3, k_{n-1} = u-n+2, k_n = u-n+1$ are valid indices in (25) since the lower summation limits can be written as $k_m = u-(m)+1$ for $m = 1,2,\ldots,n$. Thus,

$$x_{i_0-n+1} \cdots x_{i_0-2} x_{i_0-1} x_{i_0} f^{(n)}_{u,\ldots,u-n+3,u-n+2,u-n+1}\left(t-\left(i_0+u-n+1\right)T\right) \tag{26}$$

is a valid term in (25) and is equal to the first term in (24).

Setting $i = i_0 - v$ in the first summation in (22) results in

$$\sum_{k_1=u}^{-v+n-1} \sum_{k_2=k_1-1}^{-v+n-2} \cdots \sum_{k_{n-1}=k_{n-2}-1}^{-v+1} \sum_{k_n=k_{n-1}-1}^{-v} x_{i_0-v-k_1} \cdots x_{i_0-v-k_n} f^{(n)}_{k_1,\ldots,k_n}\left(t-\left(i_0-v\right)T\right). \tag{27}$$

Using the upper summation limits $k_1 = -v+n-1, \ldots, k_{n-2} = -v+2, k_{n-1} = -v+1, k_n = -v$ in (27) yields the term

$$x_{i_0-n+1} \cdots x_{i_0-2} x_{i_0-1} x_{i_0} f^{(n)}_{-v+n-1,\ldots,-v+2,-v+1,-v}\left(t-\left(i_0-v\right)T\right). \tag{28}$$

This term is equal to the second term in (24) proving that the term corresponding to $i=i_0$ and $d_1=1, d_2=2,\ldots, d_{n-1}=n-1$ in the second summation in (22) is also a term that occurs only once in the first summation in (22).

The second term examined in the second summation corresponds to $i=i_0$ and $d_1=u+v-n+2, d_2=u+v-n+3,\ldots, d_{n-1}=u+v$. This term can be written, using (8), as

$$\begin{aligned}&x_{i_0}x_{i_0-u-v+n-2}x_{i_0-u-v+n-3}\cdots x_{i_0-u-v}\,c^{(n)}_{u+v-n+2,u+v-n+3,\ldots,u+v}\left(t-i_0T\right)=\\&x_{i_0}x_{i_0-u-v+n-2}x_{i_0-u-v+n-3}\cdots x_{i_0-u-v}\sum_{k_n=u-u-v}^{-v}f^{(n)}_{k_n+u+v,\ldots,k_n+u+v-n+3,k_n+u+v-n+2,k_n}\left(t-\left(i_0+k_n\right)T\right).\end{aligned}\tag{29}$$

Since the term (29) includes a summation having the same lower and upper summation limits, it is written as

$$x_{i_0}x_{i_0-u-v+n-2}x_{i_0-u-v+n-3}\cdots x_{i_0-u-v}\,f^{(n)}_{u,\ldots,u-n+3,u-n+2,-v}\left(t-\left(i_0-v\right)T\right).\tag{30}$$

Setting $i=i_0-v$ in the first summation in (22) results in

$$\sum_{k_1=u}^{-v+n-1}\sum_{k_2=k_1-1}^{-v+n-2}\cdots\sum_{k_{n-1}=k_{n-2}-1}^{-v+1}\sum_{k_n=k_{n-1}-1}^{-v}x_{i_0-v-k_1}\cdots x_{i_0-v-k_n}f^{(n)}_{k_1,\ldots,k_n}\left(t-\left(i_0-v\right)T\right).\tag{31}$$

Using the summation limits $k_1=u,\ldots, k_{n-2}=u-n+3, k_{n-1}=u-n+2, k_n=-v$ in (31) yields the term

$$x_{i_0-v-u}\cdots x_{i_0-v-u+n-3}x_{i_0-v-u+n-2}x_{i_0}\,f^{(n)}_{u,\ldots,u-n+3,u-n+2,-v}\left(t-\left(i_0-v\right)T\right).\tag{32}$$

This term is equal to the term (30) proving that the term corresponding to $i=i_0$ and $d_1=u+v-n+2, d_2=u+v-n+3,\ldots, d_{n-1}=u+v$ in the second summation in (22) is also a term that occurs only once in the first summation in (22). Therefore, there is a one-to-one mapping between the terms in the two summations in (22). The second summation in (17) can then be written as

$$\sum_{i=-\infty}^{+\infty} \sum_{d_1=1}^{u+v-n+2} \sum_{d_2=d_1+1}^{u+v-n+3} \cdots \sum_{d_{n-1}=d_{n-2}+1}^{u+v} x_i x_{i-d_1} \cdots x_{i-d_{n-1}} c_{d_1,\ldots,d_{n-1}}^{(n)}(t-iT), \tag{33}$$

where

$$c_{d_1,\ldots,d_{n-1}}^{(n)}(t) = \sum_{k=-v}^{u-d_{n-1}} f_{k+d_{n-1},\ldots,k+d_1,k}^{(n)}(t-kT), \quad n=2,\ldots,L. \tag{34}$$

Finally, substituting $i = i - v$ into the last summation in (17) gives

$$\sum_{i=-\infty}^{+\infty} x_{i-u} x_{i-u+1} \cdots x_{i+v} f_{u,u-1,\ldots,-v}^{(L)}(t-iT) = \sum_{i=-\infty}^{+\infty} x_i x_{i-1} \cdots x_{i-u-v} f_{u,u-1,\ldots,-v}^{(L)}(t-(i-v)T). \tag{35}$$

Substituting $n = L$ into (34) to yield

$$c_{1,\ldots,u+v}^{(L)}(t-iT) = \sum_{k=-v}^{u-(u+v)} f_{k+u+v,\ldots,k+1,k}^{(L)}(t-(i+k)T) = f_{u,\ldots,-v+1,-v}^{(L)}(t-(i-v)T), \tag{36}$$

allows the last summation in (17) to be written as

$$\sum_{i=-\infty}^{+\infty} x_i x_{i-1} \cdots x_{i-u-v} c_{1,\ldots,u+v}^{(L)}(t-iT). \tag{37}$$

The magnetic saturation recording channel's output signal $y(t)$ as expressed by (6) can thus be written as the combination of (21), (33), and (37).

Hermann's model determines a magnetic saturation recording channel's output signal for an arbitrary sequence of input data symbols once the Volterra kernels – which are derived from the Volterra kernel chips – are known. Recall that the truncated Volterra series representation of a signal chip given in (4) is a function of L input data symbols $(x_{i-u},\ldots,x_{i+v})$. The 2^L signal chips generated by the set of distinct binary L-tuples

$(x_{i-u},\ldots,x_{i+v})$ provide a set of 2^L linear equations that relate 2^L signal chips to 2^L unknown kernel chips [13]. The kernel chips can be found using a direct approach by writing the set of linear equations in matrix form as $\mathbf{Y}=\mathbf{XF}$ and then solving for $\mathbf{F}=\mathbf{X}^{-1}\mathbf{Y}$ if $\mathbf{X}^{-1}$ exists. For example, the inverse of a 512 by 512 matrix must be computed to find the 512 unknown kernel chips when $L=9$. Inverting a matrix this size is feasible using programs such as MATLAB®, but the inversion's accuracy depends of the condition number of the matrix. A method that exploits the characteristics of $\mathbf{X}$, thereby avoiding the need to find $\mathbf{X}^{-1}$, is preferable.

Hermann describes just such a method in [13] that uses a special binary, periodic pseudo-random sequence (PRS) of length $M=2^L-1$ for the input data symbols. This particular PRS is known as a maximal-length shift-register sequence. A characteristic of a maximal-length PRS of length M known as the window property states that a window of length L slid along the sequence allows each nonzero binary L-tuple to be seen exactly once as shown in Fig. 3 [15]. A copy of the PRS placed at both the beginning and the end of the original sequence is used when the window extends past either end of the original sequence. The PRS is generated from a primitive polynomial $p(x)$ of degree L. For example, $p(x)=x^9+x^4+1$ for $L=9$. This primitive polynomial can be implemented using the feedback shift-register shown in Fig. 4. Each block in the feedback shift-register is a flip-flop and the adder is a modulo-2 adder. The initial state of the shift-register's flip-flops can be any value except all zeros. Each flip-flop's value is shifted to the right when the flip-flops are clocked and the shift-register goes through all $M = 2^L - 1$ distinct nonzero states before repeating.

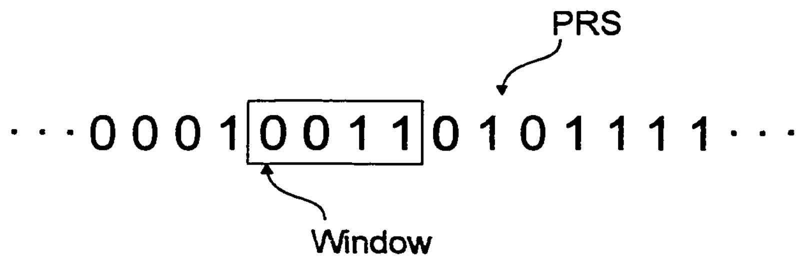

Fig. 3. The window property from [15]: every nonzero 4-tuple is seen exactly once.

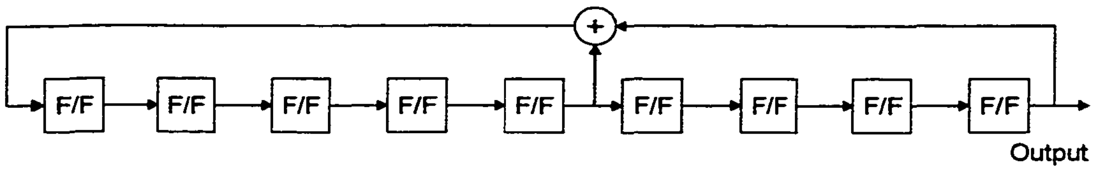

Fig. 4. Feedback shift-register from [15] for $p(x) = x^9 + x^4 + 1$.

Hermann's method exploits the fact that a magnetic saturation recording channel's input data symbols are a bipolar sequence $x_k = \pm 1$. The input data symbols are obtained from the binary PRS described above by mapping 0 to +1 and +1 to −1. Recall that the PRS generates only the nonzero binary L-tuples, hence there is no binary L-tuple that is mapped to all +1s. If one period of the mapped PRS is denoted by $\{\tilde{x}_k\} = (\tilde{x}_0, \tilde{x}_1, \ldots, \tilde{x}_{M-1})$, the set $(\tilde{x}_{(k-u)\mathrm{MOD}M}, \ldots, \tilde{x}_{(k+v)\mathrm{MOD}M})$, $k = 0, \cdots, M-1$, where MOD is the modulo operation, encompasses all distinct binary L-tuples except the one mapped to all +1s by virtue of the window property. However, the characteristics of a magnetic saturation recording channel are such that the signal chip vanishes for the binary L-tuple mapped to all +1s.

Therefore, all relevant signal chips are obtained using one period of $\{\tilde{x}_k\}$ as the input data symbols [13].

Hermann defines the output signal obtained using one period of $\{\tilde{x}_k\}$ as the input data symbols by $\{\tilde{y}_k\}=(\tilde{y}_0,\tilde{y}_1,\cdots,\tilde{y}_{MF-1})$, where the integer F is the number of samples measured per signal chip. The sets $\{\tilde{x}_k\}$ and $\{\tilde{y}_k\}$ must be causally aligned with each other before the kernel chips are computed. Using (4) and a Hadamard transformation, the kernel chips are then obtained from

$$f_{k_1,\ldots,k_n}^{(n)}(\tau=\frac{sT}{F})=\frac{1}{M+1}\sum_{k=0}^{M-1}\tilde{y}_{kF+s}\prod_{i=1}^{n}\tilde{x}_{(k-k_i)\mathrm{MOD}M}\,, \tag{38}$$

for $n=1,\cdots,L$; $s=0,\cdots,F-1$; and $M=2^L-1$. Note that (38) allows individual kernel chips to be computed without finding the inverse of a large matrix. This is advantageous because the output signal given by (6) needs to be expressible using only a handful of the 2^{L-1} Volterra kernels to be of practical use and not having to compute the kernel chips of the unneeded Volterra kernels saves much time [13].

Hermann's model characterizes a magnetic saturation recording channel – a baseband NLTI system. Recall that our first research objective is to derive a simple yet accurate model of an HPA's nonlinear behavior. The question then is whether Hermann's model and the techniques for measuring a system's Volterra kernel chips described above can be modified to characterize an HPA – a bandpass NLTI system? The following steps were taken to answer this question. First, develop the software to find the kernel chips of a baseband NLTI system using the direct approach and a maximal-length PRS input signal. Second, validate this software using a set of synthetic Volterra kernels to generate an output signal from which the system's kernel chips are derived. The Volterra kernels derived from these kernel chips are then compared with the synthetic Volterra kernels to determine how well the software performs. Finally, determine how well the software can model an HPA's nonlinear behavior using actual input and output signals.

The software development in the first step requires consideration of a magnetic saturation recording channel's characteristics vis-à-vis those of an HPA. For example, Hermann's method of utilizing (38) to determine a system's kernel chips relies on the orthogonality of a Hadamard matrix resulting from the bipolar nature of the input data symbols. Generating an actual HPA input signal limited to precisely ± 1 volt from a maximal-length PRS is, however, highly unlikely. In addition, Hermann's method cannot determine the $f^{(0)}(\tau)$ kernel chip that may exist for an HPA. Therefore, the direct approach using matrix inversion to solve a set of 2^L linear equations that relate 2^L signal chips to 2^L unknown kernel chips was chosen.

Although the $f^{(0)}(\tau)$ kernel chip can be determined using the direct approach, 2^L signal chips are needed to do so. Using a maximal-length PRS input signal to excite an HPA, however, only generates $2^L - 1$ signal chips, i.e., only the nonzero binary L-tuples are generated. A proposed solution to this limitation is to assume that the signal chip corresponding to an input data symbol sequence of L zeros has identical magnitude and opposite sign to the signal chip corresponding to an input data symbol sequence of L ones. Note that instead of mapping the input data symbols from 0 to +1 and +1 to −1 as Hermann did, the software maps them from 0 to −1 and +1 to +1. This was done to conform to the format of the actual HPA input and output signals used to test the software.

The software validation in the second step requires creating a set of synthetic Volterra kernels. Next, an output signal is generated according to (6) using the synthetic Volterra kernels and a maximal-length PRS as an input signal. The software then calculates the kernel chips by processing the output signal. Finally, the Volterra kernels are derived from the kernel chips according to (7) and (8). The derived Volterra kernels should match the synthetic Volterra kernels used to generate the output signal if the software performs properly.

Five synthetic Volterra kernels were created to represent an NLTI system having the parameters $L = 5$ and $F = 5$, namely: $c^{(1)}(t)$, $c_1^{(2)}(t)$, $c_2^{(2)}(t)$, $c_3^{(2)}(t)$, and $c_{1,2}^{(3)}(t)$. Table 2 lists the samples of each of the five actual (synthetic) Volterra kernels in one column and the Volterra kernels derived from the output signal in the adjacent column. Even thought the derived Volterra kernels are not an "exact" match, how accurate are they? To answer this question, an output signal was generated according to (6) using the derived Volterra kernels and the same maximal-length PRS as an input signal. This output signal was subtracted from the actual output signal to form the error signal shown in the bottom plot of Fig. 5. The actual output signal is also shown in the top plot of Fig. 5. A possible source of this error could be the assumption the software makes about the signal chip corresponding to an input data symbol sequence of L zeros.

$c^{(1)}(t)$		$c_1^{(2)}(t)$		$c_2^{(2)}(t)$		$c_3^{(2)}(t)$		$c_{1,2}^{(3)}(t)$	
Actual	**Derived**	**Actual**	**Derived**	**Actual**	**Derived**	**Actual**	**Derived**	**Actual**	**Derived**
0.700	0.711	0.070	0.059	0.040	0.029	0.009	-0.002	0.079	0.090
0.960	0.971	0.085	0.074	0.048	0.037	0.015	0.004	0.081	0.092
0.990	0.999	0.090	0.081	0.050	0.041	0.015	0.006	0.099	0.108
0.800	0.807	0.083	0.076	0.048	0.041	0.005	-0.002	0.099	0.106
0.470	0.475	0.058	0.053	0.040	0.035	-0.004	-0.009	0.094	0.099
0.120	0.131	0.025	0.014	0.025	0.014	-0.003	-0.014	0.075	0.086
-0.120	-0.109	0	-0.011	0.010	-0.001	0	-0.011	0.048	0.059
-0.120	-0.111	-0.015	-0.024	-0.005	-0.014	0	-0.009	0.020	0.029
0.030	0.037	-0.012	-0.019	-0.010	-0.017	0	-0.007	-0.010	-0.003
0.100	0.105	-0.004	-0.009	-0.010	-0.015	0	-0.005	-0.019	-0.014
0.070	0.081	0.006	-0.005	-0.003	-0.014			-0.012	-0.001
-0.040	-0.029	0.006	-0.005	0.007	-0.004			0.008	0.019
-0.040	-0.031	-0.001	-0.010	0.009	0			0.011	0.020
0.030	0.037	-0.001	-0.008	0.005	-0.002			0	0.007
0.020	0.025	0	-0.005	-0.001	-0.006			-0.005	0
-0.020	-0.009	0	-0.011						
0.040	0.051	0	-0.011						
0	0.009	0	-0.009						
-0.020	-0.013	0	-0.007						
0	0.005	0	-0.005						
0	0.011								
0	0.011								
0	0.009								
0	0.007								
0	0.005								

Table 2. Volterra kernels derived for $L=5$ and $F=5$ using original software.

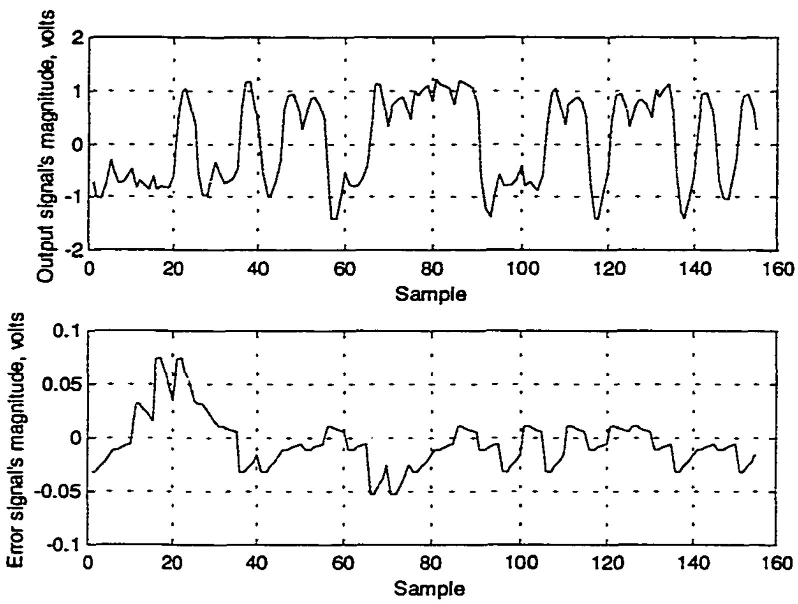

Fig. 5. Actual output signal (top) and error signal (bottom) for Volterra kernels shown in Table 2.

Recall that the software assumes that the signal chip corresponding to an input data symbol sequence of L zeros has identical magnitude and opposite sign to the signal chip corresponding to an input data symbol sequence of L ones. Generating the signal chip produced by an input data symbol sequence of L zeros tested this assumption. The software was modified to calculate the kernel chips using this new signal chip in addition to the previous signal chips generated using the maximal-length PRS. The resulting Volterra kernels derived from these kernel chips are not shown as they were in Table 2 since they are essentially identical to the actual Volterra kernels.

These results indicate that the software accurately models a baseband NLTI system when the signal chip corresponding to an input data symbol sequence of L zeros is known. The original assumption that the signal chip corresponding to an input data symbol sequence of L zeros has identical magnitude and opposite sign to the signal chip corresponding to an input data symbol sequence of L ones, although not entirely correct, appears to have "minimal" effect on the model's overall accuracy. This is important since the actual HPA output signal used to validate the software in the next step was derived using only a maximal-length PRS, i.e., the signal chip corresponding to an input data symbol sequence of L zeros was not available.

The actual HPA output signal used in the final step was generated using an input signal derived from a maximal-length PRS having parameters $L=9$ and $F=8$. The output signal was downconverted from approximately 1.9 GHz to 10 MHz and sampled at 40 MHz to yield 130,816 samples, i.e., 32 cycles of the 4088 sample maximal-length PRS. The output signal was converted to baseband by first averaging it to form a 4088 sample signal, multiplying the averaged signal by a 10 MHz sinusoid, and then lowpass filtering the resulting signal to form the baseband signal. The lowpass filter's cutoff frequency was approximately 8 MHz.

The software then calculated the kernel chips by processing the baseband output signal. The kernel chips were examined by hand to determine which Volterra kernels contributed significantly to the output signal. The seven most significant Volterra kernels in order of decreasing significance were: $c^{(1)}(t)$, $c_5^{(2)}(t)$, $c_{1,3,8}^{(4)}(t)$, $c_{1,2}^{(3)}(t)$, $c_4^{(2)}(t)$, $c_{2,3,7,8}^{(5)}(t)$, and $c_{1,5}^{(3)}(t)$. An output signal was generated using only the $c^{(1)}(t)$ Volterra kernel as a first approximation. Note that the $c^{(0)}(t)$ Volterra kernel, i.e., the $f^{(0)}(\tau)$ kernel chip, was also used to generate this and all subsequent approximations to the output signal. A power spectral density (PSD) comparison between the actual output signal and its first approximation is shown in Fig. 6. This approximation is not very accurate below the lowpass filter's cutoff frequency and is very inaccurate above it. A second approximation was generated by including the next most significant Volterra kernel $c_5^{(2)}(t)$. The PSD comparison between the actual output signal and its second approximation is shown in Fig. 7. This approximation is very accurate below the lowpass filter's cutoff frequency and much more accurate above it than the first approximation. A final approximation was generated using the remaining five Volterra kernels. The PSD comparison between the actual output signal and its final approximation is shown in Fig. 8. This approximation is extremely accurate below the lowpass filter's cutoff frequency and slightly more accurate above it than the second approximation. A time domain comparison between 100 samples of the output signal and its three approximations is shown in Figs. 9-11. Note how including just one "nonlinear" Volterra kernel results in an very good approximation as shown by the PSD and time domain comparisons in Figs. 7 and 10.

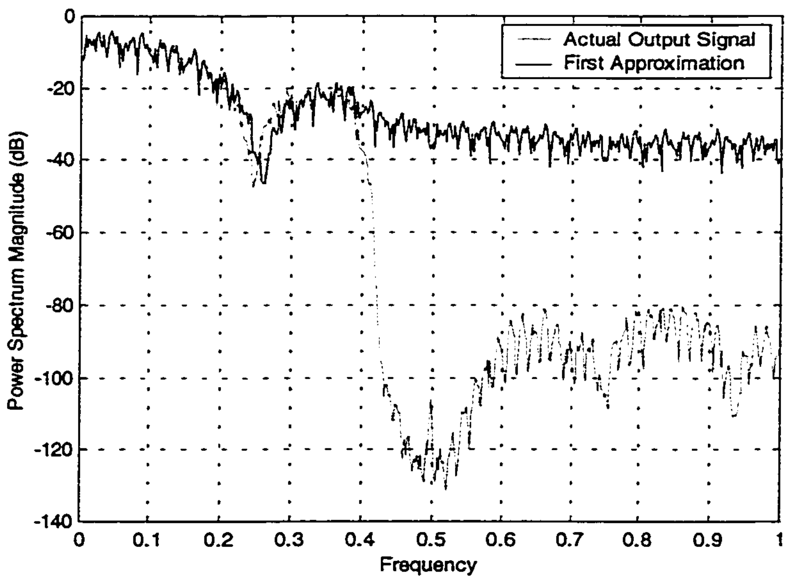

Fig. 6. PSD comparison between actual output signal (light) and its first approximation (dark) using one significant Volterra kernel.

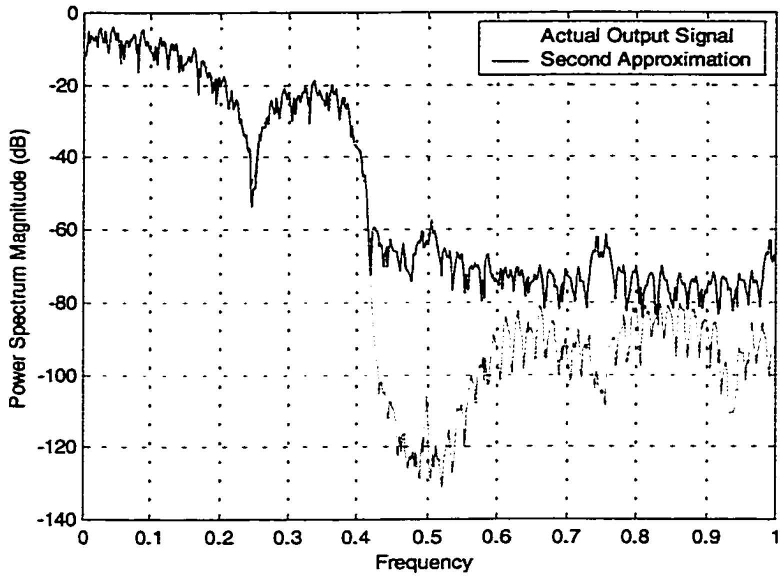

Fig. 7. PSD comparison between actual output signal (light) and its second approximation (dark) using two significant Volterra kernels.

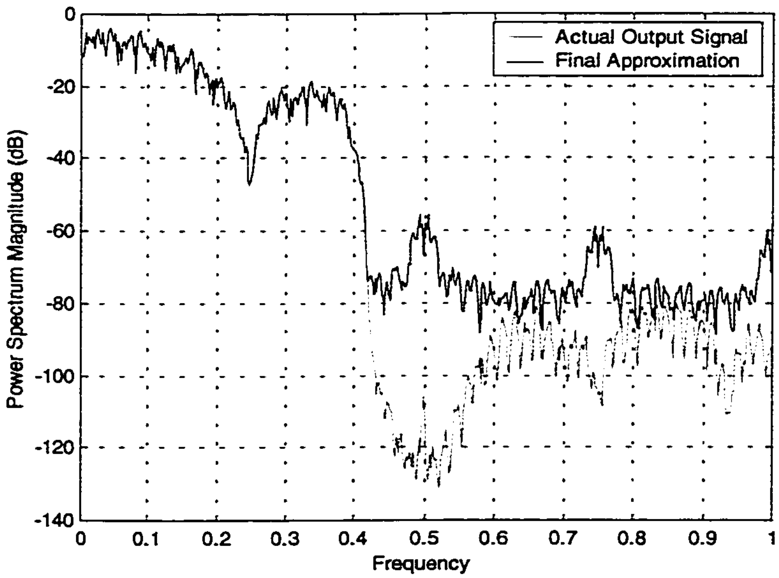

Fig. 8. PSD comparison between actual output signal (light) and its final approximation (dark) using seven significant Volterra kernels.

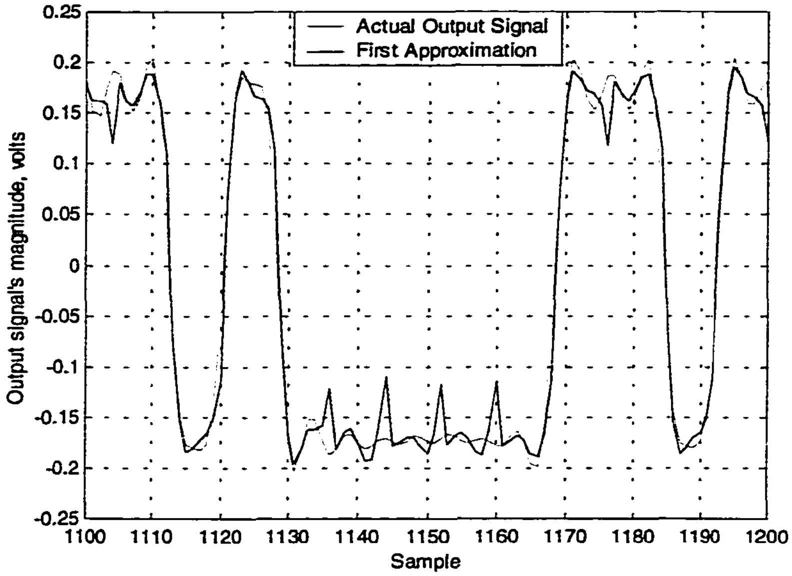

Fig. 9. Time domain comparison between actual output signal (light) and its first approximation (dark) using one significant Volterra kernel.

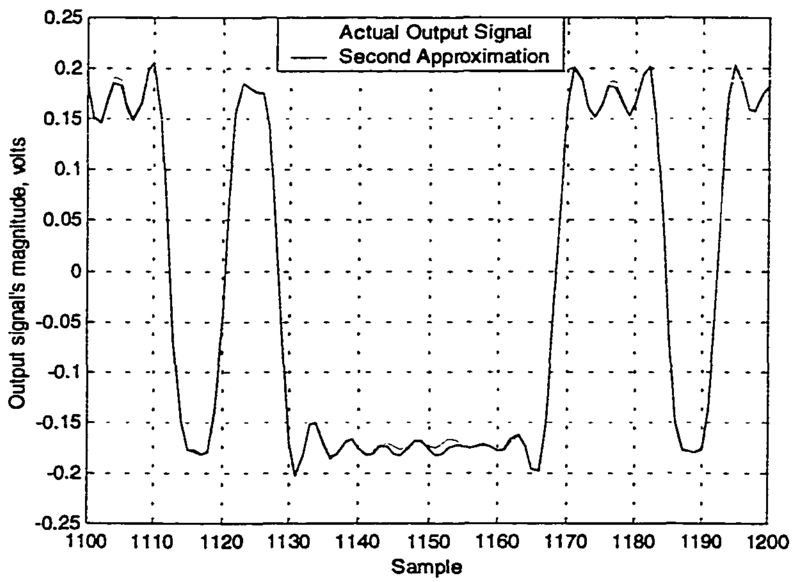

Fig. 10. Time domain comparison between actual output signal (light) and its second approximation (dark) using two significant Volterra kernels.

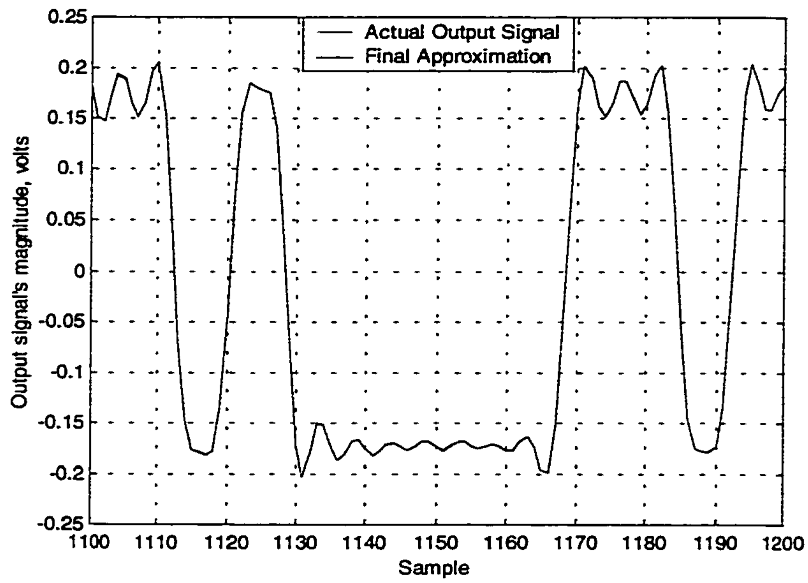

Fig. 11. Time domain comparison between actual output signal (light) and its final approximation (dark) using seven significant Volterra kernels.

The output signal was then subtracted from its three approximations to form a set of error signals. The error signals' power, referenced to 50Ω, are listed in Table 3.

Output Signal Approximation	Error Signal's Power, μW
First	11.88
Second	0.18
Final	0.02

Table 3. Error signals' power for the three output signal approximations shown in Figs. 6-11.

The final output signal approximation used 8 out of 256 Volterra kernels composed of 32 out of 512 kernel chips. This resulted in a 27.3 dB reduction in the error signal's power compared to the first output signal approximation using just the $c^{(0)}(t)$ and $c^{(1)}(t)$ kernel chips. Even though a very good output signal approximation is obtained using just a handful of Volterra kernels, the truncated Volterra series model was abandoned in favor of a simpler model for a number of reasons.

One reason the truncated Volterra series model was abandoned is that it requires a special input signal in the form of a maximal-length PRS to determine the model's parameters. One of the research objectives, however, is to use an HPA's actual modulated input signal, i.e., not a special input signal, to determine the model's parameters. The maximal-length PRS also results in a constant envelope input signal that does not fully exercise the HPA's nonlinear behavior. Another reason for abandonment is the subjective nature of choosing which Volterra kernels are significant. Just how many Volterra kernels are necessary to provide an "accurate" approximation and does this number change from one HPA to another? These reasons and others led to the investigation of the simpler, and potentially less accurate, memoryless models.

2.2 MEMORYLESS MODELS

The memoryless nonlinear models described in this and the following sections and the IS-2000 forward link simulations presented in a later chapter use the complex baseband representation of real valued narrowband bandpass signals. An IS-2000 CDMA signal uses a carrier frequency in the 2 GHz band and has a bandwidth at least 1.25 MHz – it is by definition a narrowband bandpass signal. A real valued narrowband bandpass signal $x(t)$ can be expressed as

$$x(t) = a(t)\cos(2\pi f_c t + \phi(t)), \tag{39}$$

where $a(t)$ is known as either the magnitude, amplitude, or envelope of $x(t)$ and $\phi(t)$ is its phase. This signal can also be expressed using its complex baseband representation as

$$\begin{aligned} x(t) &= x_I(t)\cos(2\pi f_c t) - x_Q(t)\sin(2\pi f_c t) \\ &= \Re\left\{\left[x_I(t) + j\,x_Q(t)\right]e^{j2\pi f_c t}\right\} \\ &= \Re\left[\tilde{x}(t)e^{j2\pi f_c t}\right], \end{aligned} \tag{40}$$

where $x_I(t)$ and $x_Q(t)$ are the in-phase and quadrature components of $x(t)$, respectively, and $\tilde{x}(t)$ is the complex envelope of $x(t)$. Its magnitude and phase uniquely describe the complex envelope $\tilde{x}(t)$.

Blachman presented an early analysis and characterization of bandpass nonlinearities in [16]-[17]. A mathematically elegant but computationally intensive nonlinear model of a traveling-wave tube's (TWT's) intermodulation effects was developed about the same time by Shimbo [18]. Shimbo's model uses the TWT's AM/AM conversion and AM/PM conversion to determine its intermodulation effects. About two years after Shimbo's paper, Kaye *et al.* developed a simpler nonlinear model based on an NLTI system's AM/AM conversion and AM/PM conversion [8]. This model is the basis for most of the nonlinear HPA models used today.

Kaye's model, shown in Fig. 12, is a quadrature arrangement consisting of two parallel memoryless nonlinearities. Each nonlinearity has an input signal having statistics identical to the original input signal and their output signals are linearly independent. In addition, each nonlinearity exhibits only amplitude distortion. This model, as do most memoryless nonlinear models, requires the NLTI system to have a flat frequency response over the input signal's bandwidth. The output signal is a function only of the input signal's complex envelope magnitude since each nonlinearity's amplitude distortion is derived from the NLTI system's AM/AM conversion and AM/PM conversion [8].

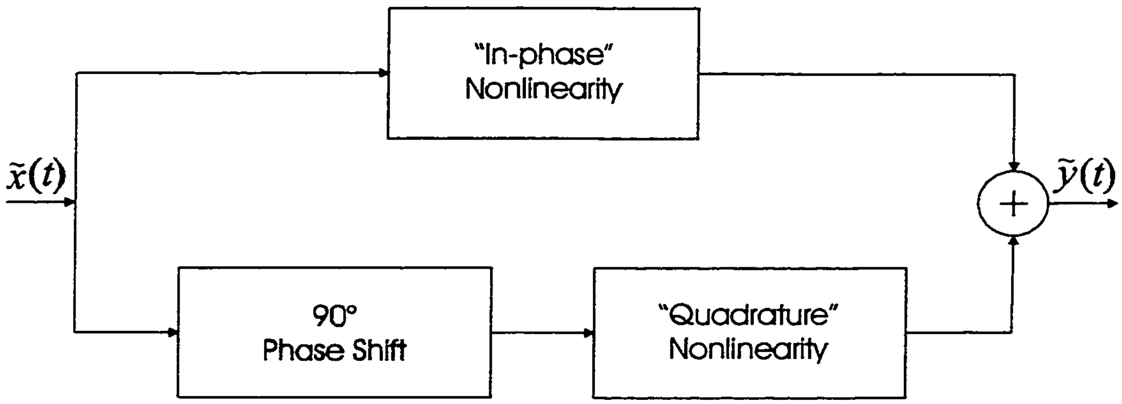

Fig. 12. Kaye's "in-phase-quadrature" nonlinear model from [8].

Kaye's model is described by

$$\tilde{y}(t) = g\left(\left|\tilde{x}(t)\right|\right)e^{j\left[p\left(\left|\tilde{x}(t)\right|\right)+\angle\left(\tilde{x}(t)\right)\right]}, \tag{41}$$

where $\tilde{y}(t)$ and $\tilde{x}(t)$ are the NLTI system's output and input signals' complex envelope, respectively, and the AM/AM conversion $g(\cdot)$ and AM/PM conversion $p(\cdot)$ depend only on the modulus (magnitude) of the input signal's complex envelope [8]. Kaye implements (41) in terms of the real and imaginary parts of the combined complex function [19]. The amplitude distortion exhibited by the nonlinearities is derived using an iterative technique to fit a Bessel series composed of Bessel functions of the first kind of order one to the AM/AM conversion along with information provided by the AM/PM conversion [8].

Saleh developed another memoryless model that is widely used to simulate a traveling-wave tube amplifier (TWTA) [7]. Saleh's model defines the AM/AM conversion $g(\cdot)$ and AM/PM conversion $p(\cdot)$ in (41) as rational polynomials. The AM/AM conversion and AM/PM conversion are given, respectively, by

$$g(|\tilde{x}(t)|) = \alpha_g |\tilde{x}(t)| / \left(1 + \beta_g |\tilde{x}(t)|^2\right) \tag{42}$$

and

$$p(|\tilde{x}(t)|) = \alpha_p |\tilde{x}(t)|^2 / \left(1 + \beta_p |\tilde{x}(t)|^2\right), \tag{43}$$

where α_g, β_g, α_p, and β_p are constants determined using a minimum mean squared error curve fitting procedure. Saleh's model uses closed-form expressions for the AM/AM conversion and AM/PM conversion, but unfortunately, it cannot be used to model solid-state HPAs [12]. A review comparing and contrasting various nonlinear HPA models, including both memory models as well as memoryless models, is presented in [19].

Probably the most popular memoryless nonlinear model used today is the "envelope-phase" model. The series envelope-phase model, shown in Fig. 13, is preferred over the parallel in-phase-quadrature model as it is a direct implementation of (41) [19]. This model is computationally efficient and can predict adjacent channel power rejection (ACPR), noise power ratio (NPR), two-tone IMD, and CDMA waveform quality [3].

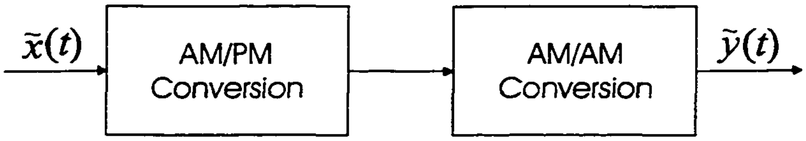

Fig. 13. "Envelope-phase" nonlinear model from [19].

The envelope-phase model requires mathematical expressions for the HPA's AM/AM conversion $g(\cdot)$ and AM/PM conversion $p(\cdot)$. An example of a solid-state

(LDMOS) HPA's AM/AM conversion and AM/PM conversion measured at 1950 MHz was previously shown in Figs. 1 and 2, respectively. Each plot in Figs. 1 and 2 consists of 201 data points. Note that the network analyzer did not record any data points when the input signal had a complex envelope magnitude of zero volts. Recall that the argument of either $g(\cdot)$ or $p(\cdot)$ is the input signal's complex envelope magnitude. Thus, interpolation must be performed whenever the argument of either $g(\cdot)$ or $p(\cdot)$ lies between any two values at which the input signal's complex envelope magnitude was measured to derive the AM/AM conversion or AM/PM conversion, respectively. An initial data point corresponding to a zero volt input signal complex envelope magnitude was added to both the AM/AM conversion data set and AM/PM conversion data set by extending each curve to the origin to increase the accuracy of the interpolation process. The points $(0,0)$ and $(0,4.3425)$ were thus added to the AM/AM conversion data set and the AM/PM conversion data set, respectively.

One of two curve fitting techniques is usually employed to provide the interpolation described above: polynomial approximation or cubic spline approximation. Polynomial approximation utilizes an n^{th} degree polynomial to fit the measured data points in a least-squares sense. A naïve assumption would be to arbitrarily increase the order n of the polynomial to achieve a better approximation. This assumption is not necessarily true as the polynomial approximation may begin to oscillate more and more between the measured data points as n increases. This tendency is overcome using cubic spline approximation. A cubic spline approximation consists of cubic polynomial approximations, having continuous first and second derivatives, defined in each interval between the measured data points. When evaluated at a measured data point, the cubic spline approximation produces the same value as the measured data point [20]. Despite the benefits of using cubic spline approximation, polynomial approximation is the preferred method to represent an HPA's AM/AM conversion and AM/PM conversion [21]-[22].

A polynomial approximation can accurately fit an HPA's AM/AM conversion and AM/PM conversion derived from a network analyzer. The question is what polynomial order n should the approximation use? The polynomial order should not be too large as mentioned earlier but it must be large enough to accurately fit the data set. A series of polynomial approximations of increasing order n was fitted to the AM/AM conversion and AM/PM conversion shown in Figs. 1 and 2, respectively. The actual AM/AM conversion and AM/PM conversion were then subtracted from the appropriate polynomial approximations to form a set of error signals. The error signals' power, referenced to 50Ω, for the AM/AM conversion and AM/PM conversion are listed in Tables 4 and 5, respectively. A 13th order polynomial approximation was chosen to represent both the AM/AM conversion and AM/PM conversion, thus to balance the approximations' accuracy with the desire to use as small a polynomial order as possible to increase the envelope-phase model's speed. A comparison of the actual AM/AM conversion and AM/PM conversion with their 13th order polynomial approximations is not shown since they are essentially identical.

Polynomial Order – AM/AM Conversion	**Error Signal's Power, μW**
15	1.4
13	1.8
11	35.2
9	157.8

Table 4. Error signals' power for various order AM/AM conversion polynomial approximations.

Polynomial Order – AM/PM Conversion	**Error Signal's Power, nW**
13	1.7
11	10.6
9	30.6
7	71.8

Table 5. Error signals' power for various order AM/PM conversion polynomial approximations.

Actual input/output signal data sets from the solid-state HPA having the AM/AM conversion and AM/PM conversion shown in Figs. 1 and 2, respectively, are needed to validate the software implementation of the envelope-phase model. The input signal used to generate an output signal consists of the summation of 250 randomly phased sinusoids spaced 5 kHz apart and having a center frequency of 1950 MHz. This quasi-CDMA signal has a bandwidth of approximately 1.25 MHz. The HPA's input and output signals are both downconverted to 10.24 MHz and sampled at 40.96 MHz. The two signals are not sampled synchronously causing an unknown phase shift between the two sampled signal data sets.

The raw data samples of the HPA's input and output signals are pre-processed to convert them into a form suitable for use by the envelope-phase model. For illustrative purposes the pre-processing of the HPA's input signal is discussed with the understanding that the steps are the same for pre-processing the output signal. The input signal is periodic with a period consisting of 8192 samples at the aforementioned sampling rate. The input signal data set consists of 65,536 samples, i.e., eight periods containing 8192 samples each. The first step is to average the input signal to lessen the impact of measurement noise, thus obtaining one period containing 8192 samples. The next step is to remove any d.c. component present in the input signal. The input signal is then filtered using an inverse filter.

Inverse filtering is done to mitigate the effects of the analog filters and other devices in the downconversion path between the HPA and the analog-to-digital converter (ADC). Only one downconversion path is used – it is switched between the HPA's input and output – resulting in the input and output signals not being sampled synchronously. The inverse filtering technique makes use of the manner in which a data set is gathered. Recall that the HPA's input signal is sampled at 40.96 MHz and is periodic such that each period contains 8192 samples. This results in a 5 kHz spacing between frequency bins when the signal's fast Fourier transform (FFT) is computed. The downconversion path's frequency response had previously been measured using a network analyzer at 5 kHz increments from 1.24 to 19.24 MHz. Inverse filtering can thus be performed using the following technique.

The first step is to compute the FFT of the signal to be "equalized". The second step is to pad the downconversion path's frequency response from d.c. to 1.235 MHz and from 19.245 to 20.475 MHz, i.e., fill in the frequency response's missing values. The values used to pad the frequency response will be discussed shortly. The third step is to "fold" the frequency response about the foldover frequency and form the complex conjugate of the folded portion. An item of consideration is what value to assign to the foldover frequency. The fourth step is to take the inverse of the extended frequency response at each frequency. This requires the frequency response to be nonzero at all frequencies. The next step is to multiply the input signal's FFT by the inverse of the extended frequency response term by term. Finally, the real part of the inverse FFT of this product yields the equalized input signal.

The downconversion path's measured frequency response gain is shown in Fig. 14. The frequency response was padded using the first and last measured values, e.g., the value at 1.24 MHz was extended to d.c. and the value at 19.24 MHz was extended to 20.475 MHz. These padded frequency bins could not be made zero or even values close to zero since this would introduce large discontinuities in the frequency response and lead to problems when inverting the frequency response. The downconversion path's padded frequency response gain is shown in Fig. 15.

The step of folding and conjugating the padded frequency response requires the selection of a value to assign to the foldover frequency. The value of the padded frequency response at 20.475 MHz was chosen for the foldover frequency instead of setting the value to zero for the reasons discussed above. The downconversion path's extended frequency response gain is shown in Fig. 16. Inverting the extended frequency response yields an inverted frequency response having the gain characteristic shown in Fig. 17.

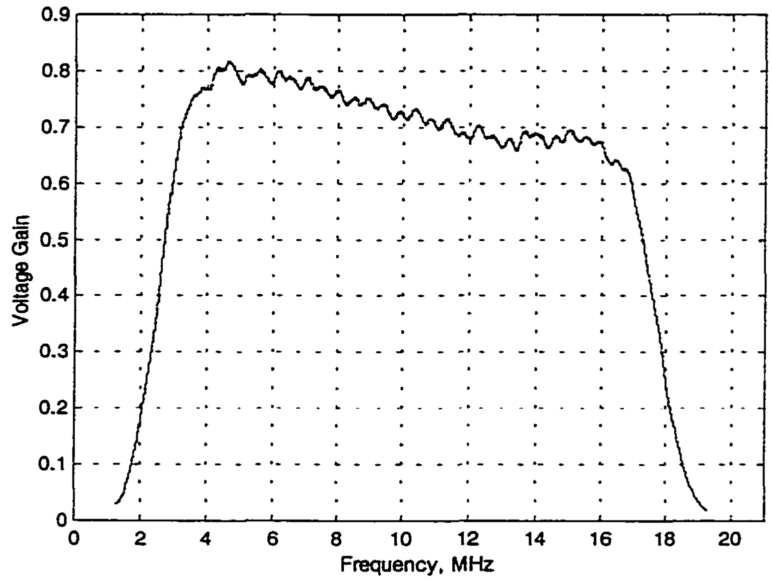

Fig. 14. Downconversion path's frequency response gain.

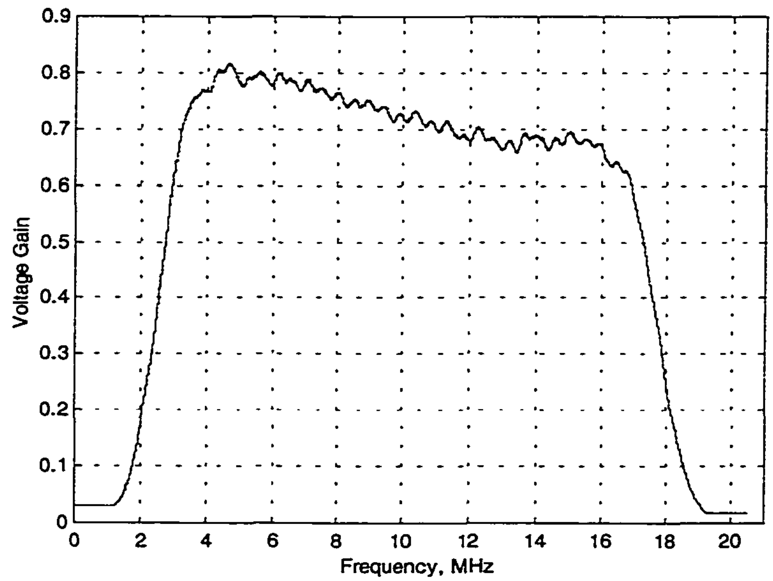

Fig. 15. Downconversion path's padded frequency response gain.

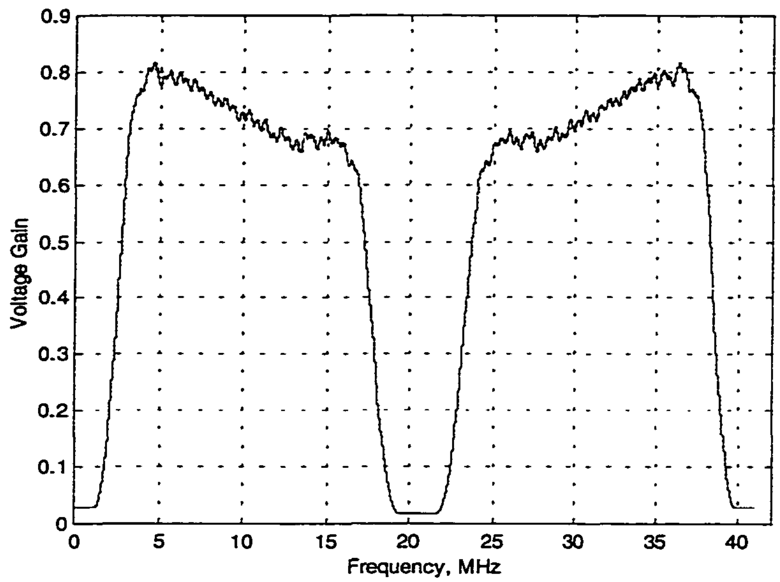

Fig. 16. Downconversion path's extended frequency response gain.

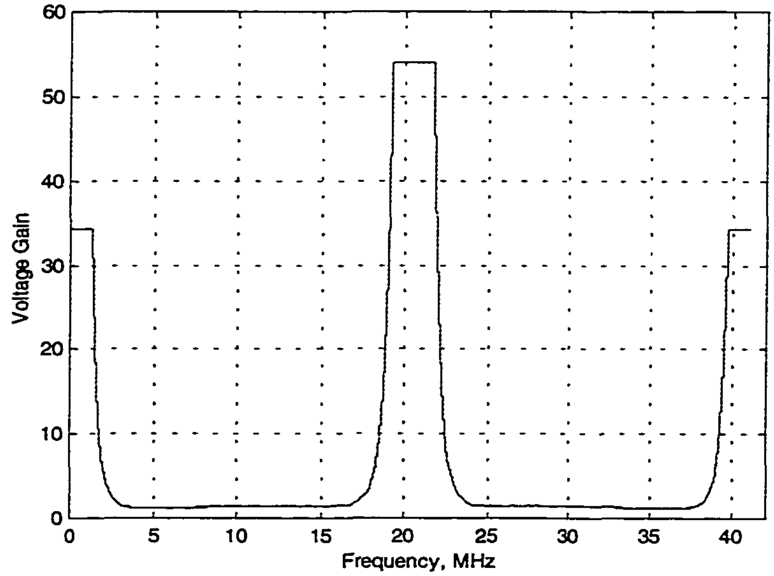

Fig. 17. Downconversion path's inverted frequency response gain.

This inverted frequency response causes problems due to the extremely large gain near d.c. and the foldover frequency. The resulting enhancement of the low and high frequency content of the signal being equalized can be avoided by limiting the inverted frequency response gain to a more reasonable value near d.c. and the foldover frequency. The gain near the foldover frequency is about 55 while the passband gain is less than 2. Limiting the maximum downconversion path's inverted frequency response gain to a value slightly less than 2 results in the modified inverted frequency response gain shown in Fig. 18. This modified inverted frequency response is used to equalize the HPA's input signal.

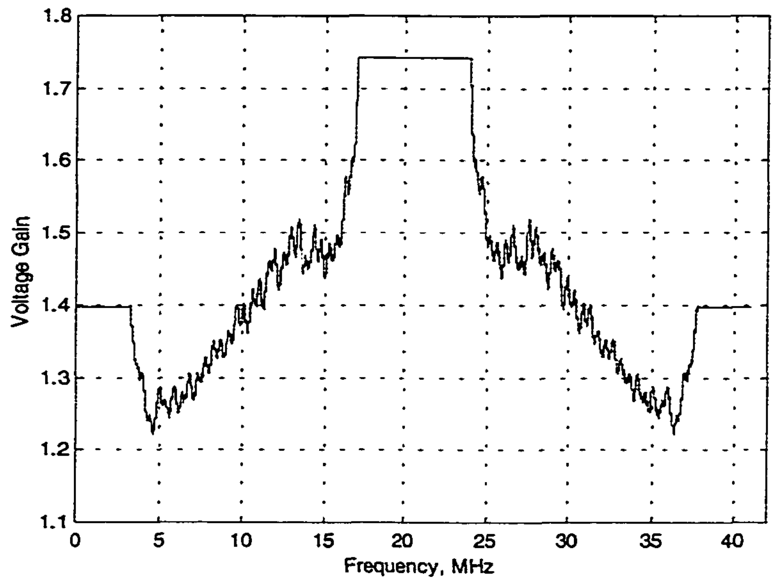

Fig. 18. Downconversion path's modified inverted frequency response gain.

The final pre-processing step is to scale the input signal's data samples so that the signal has the proper average power. The 16 bit ADC produces an integer output between –32,768 and +32,767, of which only the 12 most significant bits are used. The ADC's output is not the actual input signal's amplitude but a scaled version of it. However, the signal can be properly scaled since its actual average power is known. Even though not required, one more step is usually included. The signal is interpolated by a factor such as eight so that its time domain representations are more meaningful. The envelope-phase model's output can be decimated by the same factor when frequency domain representations are needed.

The pre-processed input signal and the polynomial approximations of the AM/AM conversion and AM/PM conversion are the envelope-phase model's input parameters. The bandpass pre-processed input signal is first converted to an analytic signal using MATLAB's Hilbert transform algorithm. Then the analytic signal is converted to a complex envelope signal by multiplying it with a complex sinusoid having a 10.24 MHz carrier frequency. Next, (41) is implemented using the complex envelope signal and the AM/AM conversion and AM/PM conversion. The resulting complex envelope output signal is then converted to an analytic signal by multiplying it with a complex sinusoid having a 10.24 MHz carrier frequency and a phase to be determined. Finally, the model generates a bandpass output signal by taking the real part of the analytic output signal.

The unknown phase shift between the actual input and output signals caused by non-synchronous sampling is problematic. The envelope-phase model is validated by comparing the actual output signal with the output signal derived using the actual input signal and the polynomial approximations of the AM/AM conversion and AM/PM conversion. Even if the model was able to perfectly model the HPA, the derived output signal would not be an exact replica of the actual output signal due to this unknown phase shift. The solution to this problem is to introduce an additional phase shift when converting the derived analytic output signal into a complex envelope signal. This additional phase shift is chosen by minimizing the power of the error signal formed by subtracting the actual output signal from the derived output signal.

Two input/output signal data sets were used to validate the software implementation of the envelope-phase model. Both input signals have a 10 dB peak-to-average power ratio. The input signal in the first data set has an average power of –9.0 dBm and the corresponding output signal has an average power of +41.5 dBm. The input and output signals in the second data set have an average power 1 dBm higher. Note that these signals' average power are referenced to 50Ω. An interpolation/decimation factor of eight was used in all the model tests performed in this and the following section.

The first model test used the first input/output signal data set and the 13th order polynomial approximations chosen to represent both the AM/AM conversion and AM/PM conversion based on the considerations discussed previously. An additional phase shift of 296° resulted in the lowest error signal power. A PSD comparison between the actual output signal and the derived output signal is shown in Fig. 19. The same PSD comparison limited to a 4 MHz bandwidth around the carrier frequency is shown in Fig. 20. The derived output signal's PSD accurately models the actual output signal's PSD within the approximately 1.25 MHz bandwidth of the actual input signal. The derived output signal's PSD also predicts the actual output signal's sideband regrowth within approximately 3-5 dB. A time domain comparison between two different 100 sample segments of the actual output signal and the derived output signal is shown in Figs. 21 and 22. The time domain error signal's maximum value is 6.28 volts.

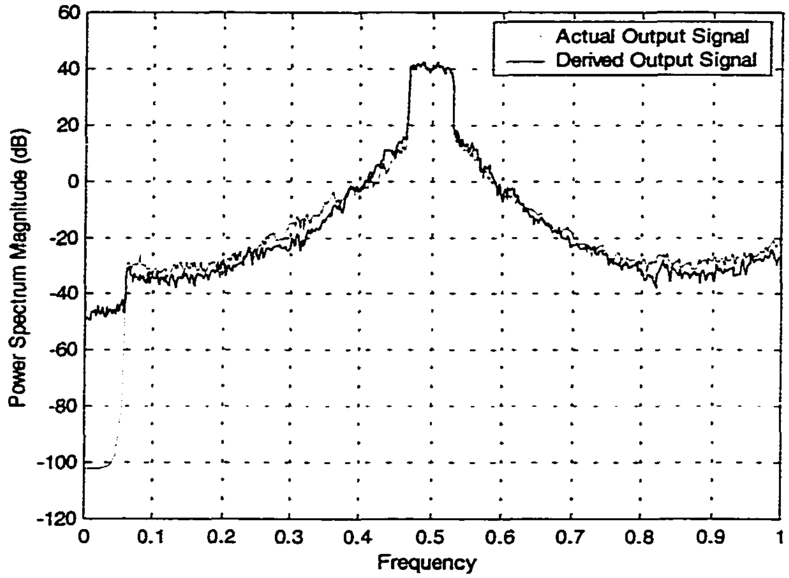

Fig. 19. PSD comparison between actual output signal (light) and output signal derived using 13^{th} order polynomial approximations for both the AM/AM conversion and AM/PM conversion (dark). First data set.

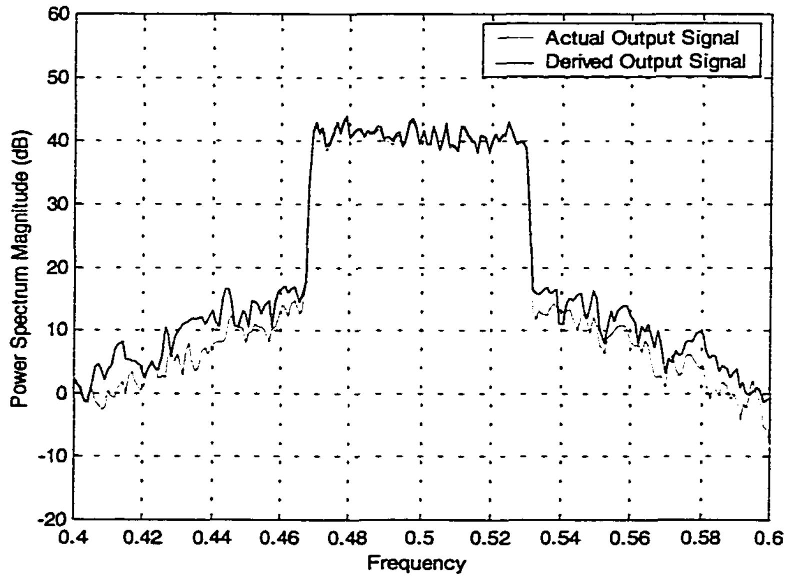

Fig. 20. PSD comparison between actual output signal (light) and output signal derived using 13^{th} order polynomial approximations for both the AM/AM conversion and AM/PM conversion (dark) limited to a 4 MHz bandwidth around the carrier frequency. First data set.

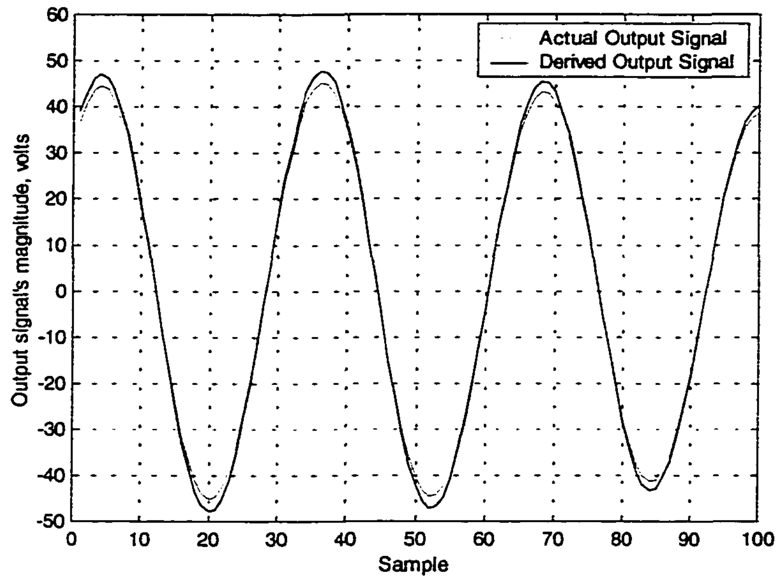

Fig. 21. Time domain comparison between 100 samples of actual output signal (light) and output signal derived using 13th order polynomial approximations for both the AM/AM conversion and AM/PM conversion (dark). First data set.

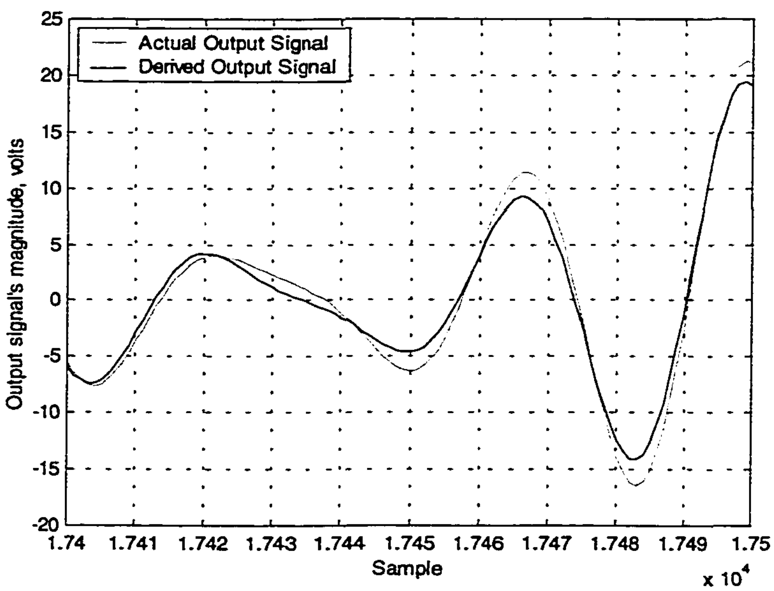

Fig. 22. Time domain comparison between another 100 samples of actual output signal (light) and output signal derived using 13th order polynomial approximations for both the AM/AM conversion and AM/PM conversion (dark). First data set.

The time domain comparison between the actual output signal and the derived output signal, or the equivalent time domain error signal, provide one measure of the model's effectiveness. Another method of measuring the model's effectiveness is to examine the frequency domain representation of the error signal by comparing the magnitude of the output signal's FFT with the magnitude of the error signal's FFT as is done in Fig. 23. Note that the actual output signal's maximum PSD magnitude has been scaled to approximately 0 dB compared to the approximately 40 dB value shown in the earlier figures. The maximum error signal PSD magnitude is about 20 dB down from that of the actual output signal.

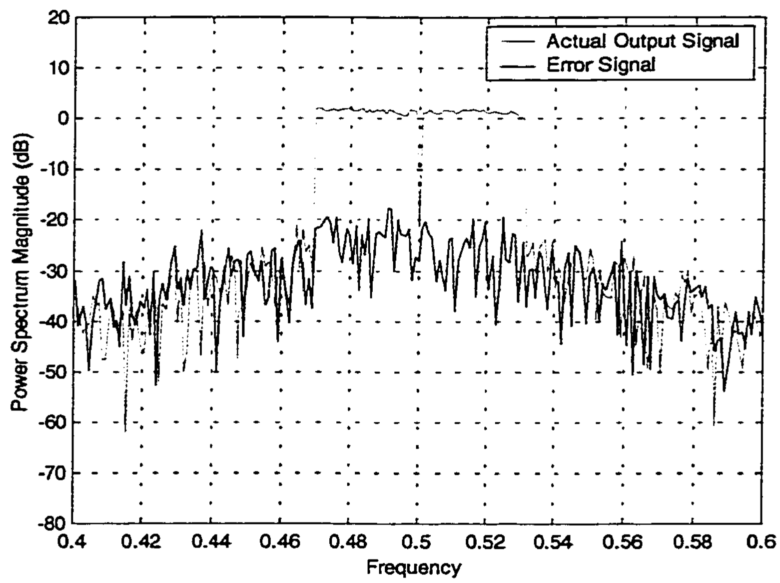

Fig. 23. PSD comparison between actual output signal (light) and error signal derived using 13th order polynomial approximations for both the AM/AM conversion and AM/PM conversion (dark) limited to a 4 MHz bandwidth around the carrier frequency. First data set.

Recall that 13th order polynomial approximations were chosen to represent the AM/AM conversion and AM/PM conversion based on the error signals' power listed in

Tables 4 and 5. Additional model tests were performed using lower order polynomial approximations to determine how sensitive the model is to variations in its parameters. Table 6 lists the time domain error signals' power, referenced to 50Ω, for various order AM/AM conversion and AM/PM conversion polynomial approximations. The envelope-phase model seems to be rather insensitive to the polynomial approximation order used for either the AM/AM conversion or the AM/PM conversion as long as reasonable values are used since the error signal power increased by only 0.3 mW when changing from both 13th order polynomial approximations to 9th and 7th order polynomial approximations for the AM/AM conversion and AM/PM conversion, respectively. Referring to Table 4, the error signal's power changed by two orders of magnitude for the same change in polynomial order. Note that the error signals referred to in Table 6 are the difference between the actual output signal and the derived output signals and the error signals referred to in Tables 4 and 5 are the difference between the actual AM/AM conversion and AM/PM conversion and their respective polynomial approximations.

Polynomial Order – AM/AM Conversion	Polynomial Order – AM/PM Conversion	Error Signal's Power, mW
13	13	68.1
13	11	68.1
11	9	68.1
9	7	68.4

Table 6. Error signals' power for various order AM/AM conversion and AM/PM conversion polynomial approximations. First data set.

The next model test used the second input/output signal data set that has the same peak-to-average power ratio as the first data set but a 1 dBm higher average power. The same 13th order polynomial approximations chosen to represent the AM/AM conversion and AM/PM conversion were also used. An additional phase shift of 298° was needed to minimize the error signal power. A PSD comparison between the actual output signal and the derived output signal is shown in Fig. 24. The same PSD comparison limited to a 4 MHz bandwidth around the carrier frequency is shown in Fig. 25. As before, the derived output signal's PSD very accurately models the actual output signal's PSD within the approximately 1.25 MHz bandwidth of the actual input signal and predicts the actual output signal's sideband regrowth within approximately 3-5 dB. Time domain comparisons between segments of the actual output signal and the derived output signal are not shown since they are similar to those shown in Figs. 21 and 22. The time domain error signal's maximum value is 5.81 volts and the maximum error signal PSD magnitude is about 20 dB down from that of the actual output signal as shown in Fig. 26.

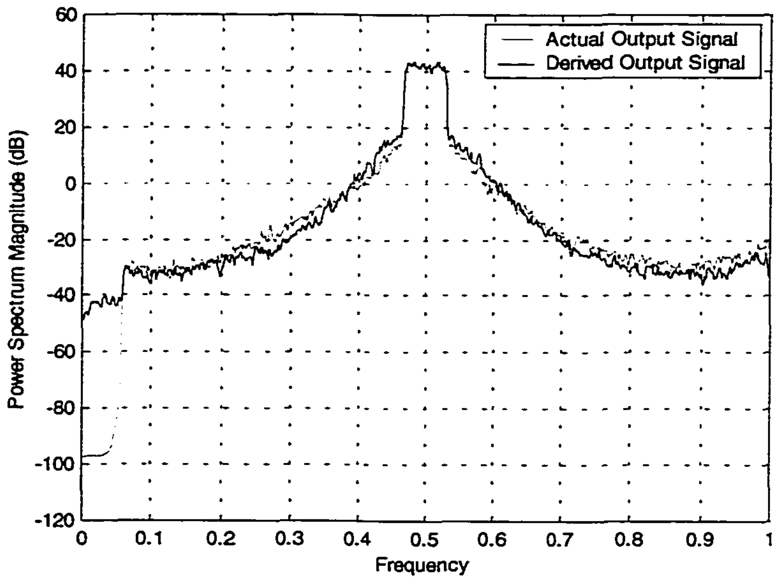

Fig. 24. PSD comparison between actual output signal (light) and output signal derived using 13^{th} order polynomial approximations for both the AM/AM conversion and AM/PM conversion (dark). Second data set.

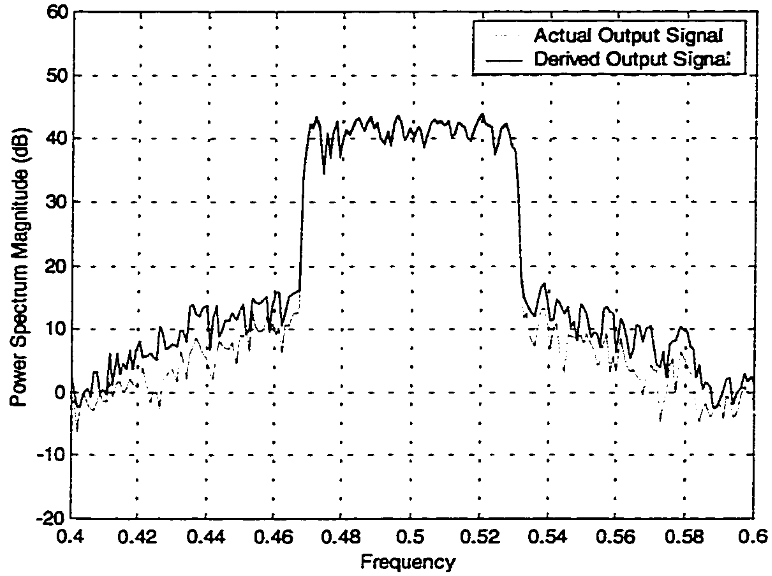

Fig. 25. PSD comparison between actual output signal (light) and output signal derived using 13th order polynomial approximations for both the AM/AM conversion and AM/PM conversion (dark) limited to a 4 MHz bandwidth around the carrier frequency. Second data set.

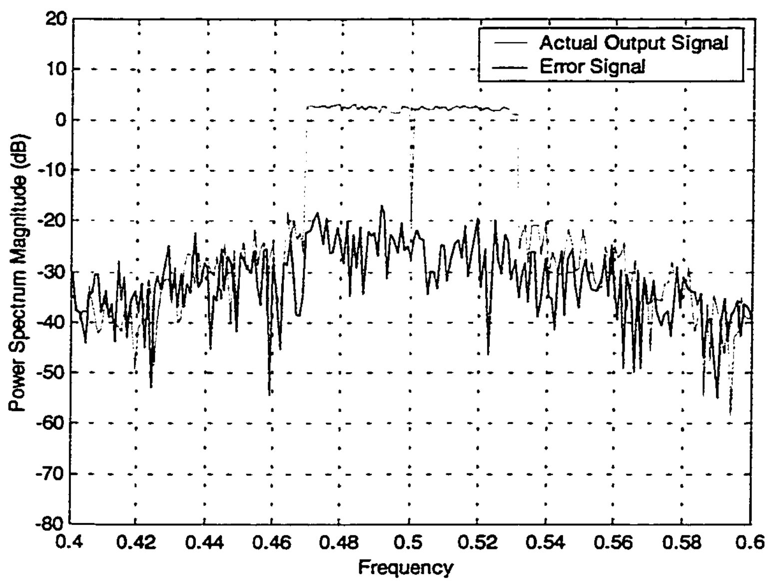

Fig. 26. PSD comparison between actual output signal (light) and error signal derived using 13th order polynomial approximations for both the AM/AM conversion and AM/PM conversion (dark) limited to a 4 MHz bandwidth around the carrier frequency. Second data set.

Once again, additional model tests were performed using various lower order AM/AM conversion and AM/PM conversion polynomial approximations with Table 7 listing the time domain error signals' power referenced to 50Ω. The error signal power remained the same when changing from both 13th order polynomial approximations to 9th and 7th order polynomial approximations for the AM/AM conversion and AM/PM conversion, respectively. Interestingly, the error signal power was 0.1 mW lower for the two intermediate order polynomial approximations.

Polynomial Order – AM/AM Conversion	**Polynomial Order – AM/PM Conversion**	**Error Signal's Power, mW**
13	13	64.2
13	11	64.1
11	9	64.1
9	7	64.2

Table 7. Error signals' power for various order AM/AM conversion and AM/PM conversion polynomial approximations. Second data set.

The envelope-phase model, using polynomial approximations of the HPA's AM/AM conversion and AM/PM conversion derived from network analyzer measurements, appears capable of producing a maximum error signal PSD magnitude about 20 dB down from that of the actual output signal. Research and development engineers would prefer to have a model capable of producing a maximum error signal PSD magnitude about 50 to 60 dB down from that of the actual output signal. Two possible causes of modeling error are inaccurate network analyzer data and inaccurate measurement of the input signal's average power. Inaccurate network analyzer data would lead to AM/AM conversion and AM/PM conversion polynomial approximations that do not represent the HPA's true nonlinear characteristics. This in turn would cause the magnitude and/or phase of the derived complex envelope output signal to be in error. Likewise, using the wrong average power to scale the input signal would cause the magnitude and/or phase of the derived complex envelope output signal to be in error. Even if the network analyzer accurately measures the AM/AM conversion and AM/PM conversion, do they truly represent the HPA's nonlinear characteristics when it is driven by a modulated signal? Inasmuch as an HPA's 1 dB compression point can be 1-2 dB lower when measured with a CDMA signal as when measured with a CW power sweep [3], the answer is probably not, especially when the HPA is driven hard. A solution to this problem, and one of the research objectives, is to derive the HPA's AM/AM conversion and AM/PM conversion from its actual modulated input and output signals.

Heutmaker describes a technique in [23] to derive an HPA's AM/AM conversion and AM/PM conversion using a binary phase-shift keying (BPSK) signal to drive the HPA. A vector signal analyzer then captures the HPA's input and output signals from which its AM/AM conversion and AM/PM conversion are derived. However, it is not feasible to measure an HPA's input and output signals, either periodically or continuously, using a vector signal analyzer when the HPA is operating in a base station. The research for this dissertation resulted in the development of an alternative technique that foregoes using a vector signal analyzer and instead derives the HPA's AM/AM conversion and AM/PM conversion from samples of the HPA's input and output signals when it is driven by a CDMA or quasi-CDMA signal. The following steps describe this technique using the previous input/output signal data sets.

The first step is to convert the bandpass pre-processed input and output signals to analytic signals using MATLAB's Hilbert transform algorithm. Second, the analytic signals are converted to complex envelope signals by multiplying them with a complex sinusoid having a 10.24 MHz carrier frequency. Third, the magnitude and phase of the respective input and output signals' complex envelope are determined. The fourth step is to align the input signal's complex envelope magnitude with the output signal's complex envelope magnitude using a correlation algorithm. The output signal's complex envelope phase is then shifted the same number of samples its magnitude was shifted to align it with the input signal's complex envelope magnitude.

The next step is to find the HPA's AM/AM conversion by plotting the output signal's complex envelope magnitude vs. the input signal's complex envelope magnitude on a point-by-point basis. Similarly, the HPA's AM/PM conversion is found by plotting the difference between the output signal's complex envelope phase and the input signal's complex envelope phase vs. the input signal's complex envelope magnitude on a point-by-point basis. Finally, $g(\cdot)$ and $p(\cdot)$ are determined by fitting a polynomial approximation to the AM/AM conversion's and AM/PM conversion's "scatter plot", respectively, found in the previous step.

Initially, the bandpass pre-processed input and output signals were aligned and not their complex envelope signals. The two signals must be aligned because they are not sampled synchronously. The resulting scatter plots bore little resemblance to the HPA's AM/AM conversion and AM/PM conversion and were thus unusable. Although there is no harm in first aligning the pre-processed input and output signals, the key to obtaining usable scatter plots is alignment based on their complex envelope signals' magnitude. A possible explanation is that a complex envelope signal's magnitude does not change as rapidly as its corresponding bandpass signal's amplitude does. This finer "resolution" may let the correlation algorithm do a better job of aligning the complex envelope signals than the bandpass signals.

The above described technique was used on the first input/output signal data set to derive the AM/AM conversion and AM/PM conversion of the solid-state HPA with the nonlinear characteristics, as measured by a network analyzer, previously shown in Figs. 1 and 2. The data points comprising the AM/AM (AM/PM) conversion derived using this technique are referred to as the AM/AM (AM/PM) scatter plot. A comparison between the AM/AM scatter plot and the network analyzer derived AM/AM conversion is shown in Fig. 27. There is general agreement between the "curves" with a notable exception: the AM/AM scatter plot has a larger linear region. A comparison between the AM/PM scatter plot and the network analyzer derived AM/PM conversion is shown in Fig. 28. Shifting the AM/PM conversion by adding a constant value of –64° to each data sample results in the AM/PM conversion more or less overlaying the AM/PM scatter plot as shown in Fig. 29. As before, there is general agreement between the curves with the exception of the phase shift. Note that a phase shift of –64°, i.e., 296°, is the same phase shift that was required to minimize the error signal power during the first model test using the network analyzer derived AM/AM conversion and AM/PM conversion polynomial approximations.

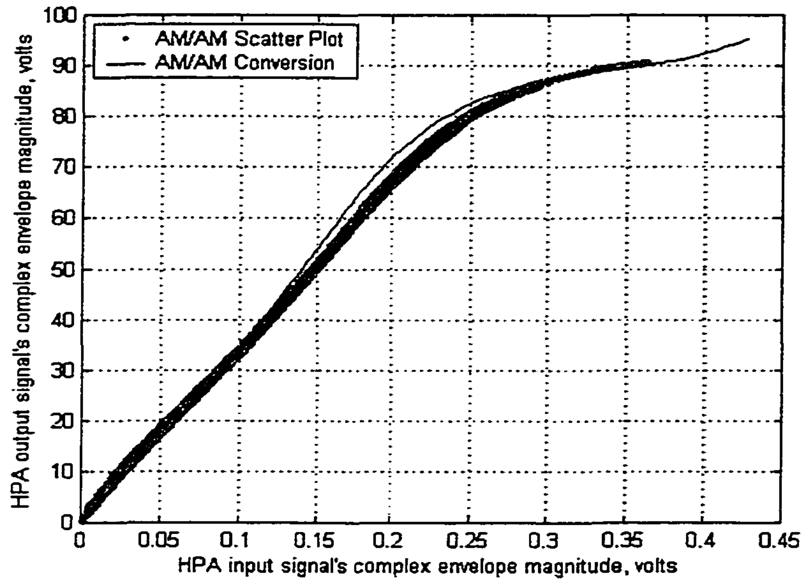

Fig. 27. Comparison between AM/AM scatter plot (light) and network analyzer derived AM/AM conversion (dark). First data set.

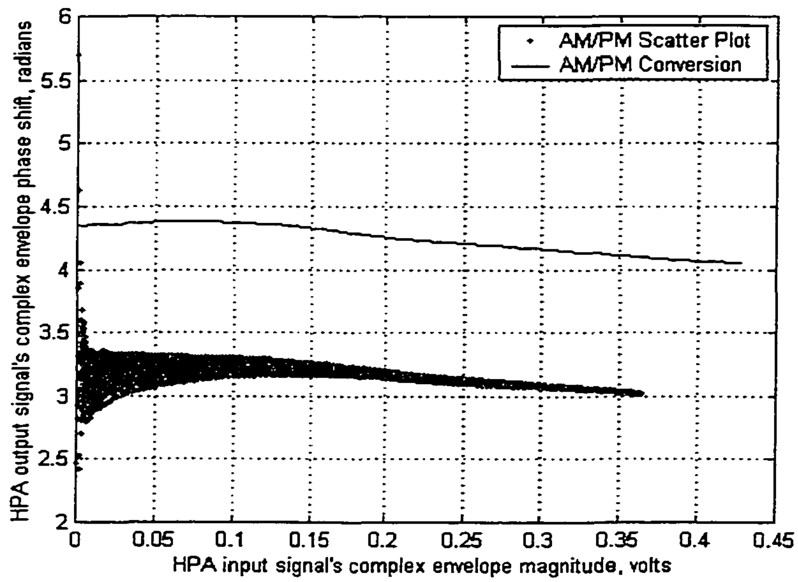

Fig. 28. Comparison between AM/PM scatter plot (light) and network analyzer derived AM/PM conversion (dark). First data set.

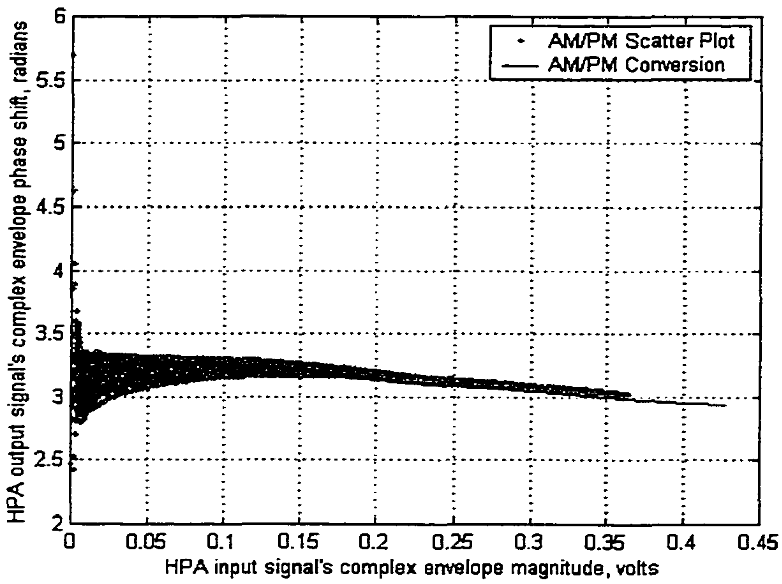

Fig. 29. Comparison between AM/PM scatter plot (light) and network analyzer derived AM/PM conversion (dark) shifted by –64°. First data set.

A series of polynomial approximations having the same order as those fitted to the AM/AM conversion and AM/PM conversion was fitted to the AM/AM scatter plot and AM/PM plot, respectively. A comparison between the 13th order polynomial approximations of the AM/AM scatter plot and AM/AM conversion and between the 13th order polynomial approximations of the AM/PM scatter plot and AM/PM conversion is shown in Figs. 30 and 31, respectively. The AM/AM scatter plot's polynomial approximation clearly shows a larger linear region as compared to the AM/AM conversion's polynomial approximation. The AM/PM scatter plot's polynomial approximation shows signs of oscillation – possibly from using too large a polynomial order or possibly the result of the rather large variance in the AM/PM scatter plot at low input signal magnitudes.

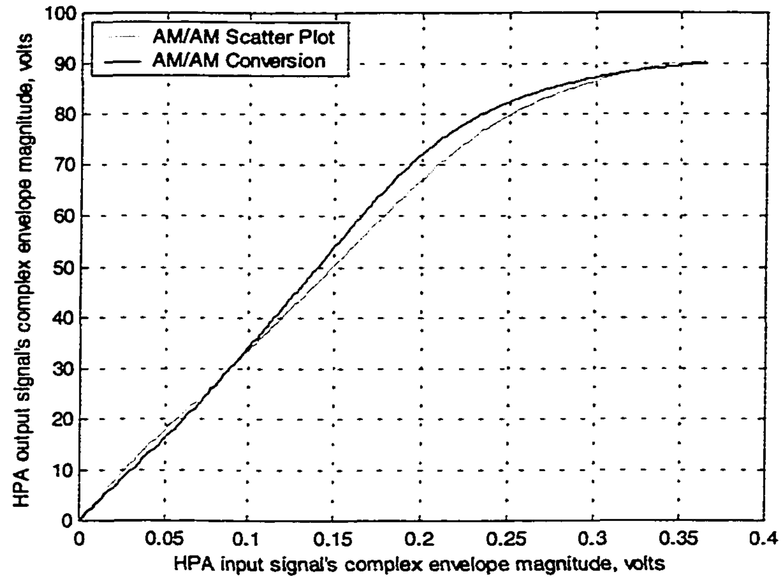

Fig. 30. Comparison between 13th order AM/AM scatter plot polynomial approximation (light) and network analyzer derived 13th order AM/AM conversion polynomial approximation (dark). First data set.

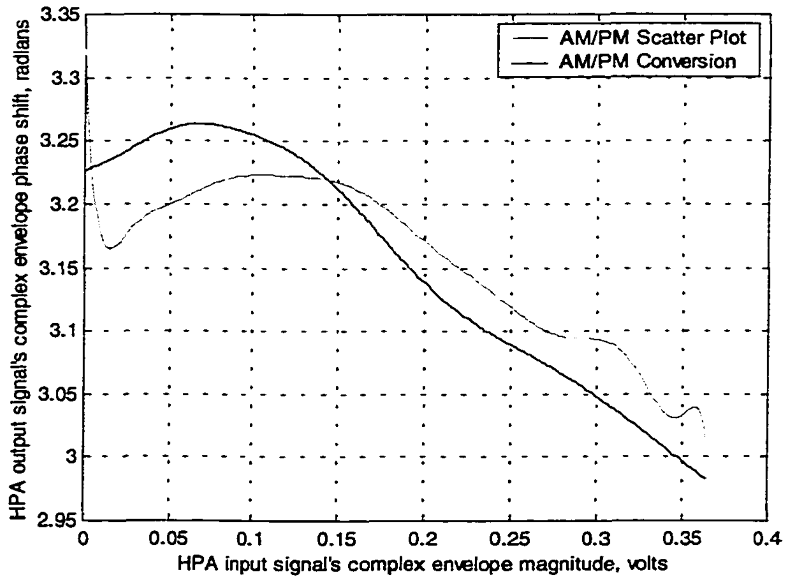

Fig. 31. Comparison between 13th order AM/PM scatter plot polynomial approximation (light) and network analyzer derived 13th order AM/PM conversion polynomial approximation shifted by –64° (dark). First data set.

The next model test used the first input/output signal data set and 13th order polynomial approximations of the AM/AM scatter plot and AM/PM scatter plot. No additional phase shift was required to achieve the lowest error signal power. A PSD comparison between the actual output signal and the derived output signal is shown in Fig. 32. The same PSD comparison limited to a 4 MHz bandwidth around the carrier frequency is shown in Fig. 33. The derived output signal's PSD almost exactly models the actual output signal's PSD within the approximately 1.25 MHz bandwidth of the actual input signal. The derived output signal's PSD also predicts the actual output signal's sideband regrowth within approximately 1 dB. Compare Figs. 32 and 33 with Figs. 19 and 20 to see the improvement achieved by deriving the HPA's AM/AM conversion and AM/PM conversion from its modulated input and output signals. A time domain comparison between the same two 100 sample segments of the actual output signal and the derived output signal shown in Figs. 21 and 22 for the network analyzer derived nonlinear characteristics is shown in Figs. 34 and 35 for the scatter plot derived nonlinear characteristics. Notice the dramatic improvement between Fig. 21 and Fig. 34. The time domain error signal's maximum value is 2.82 volts. The maximum error signal PSD magnitude is about 30 dB down from that of the actual output signal as shown in Fig. 36 – a 10 dB improvement over the error signal shown in Fig. 23 for the network analyzer derived nonlinear characteristics.

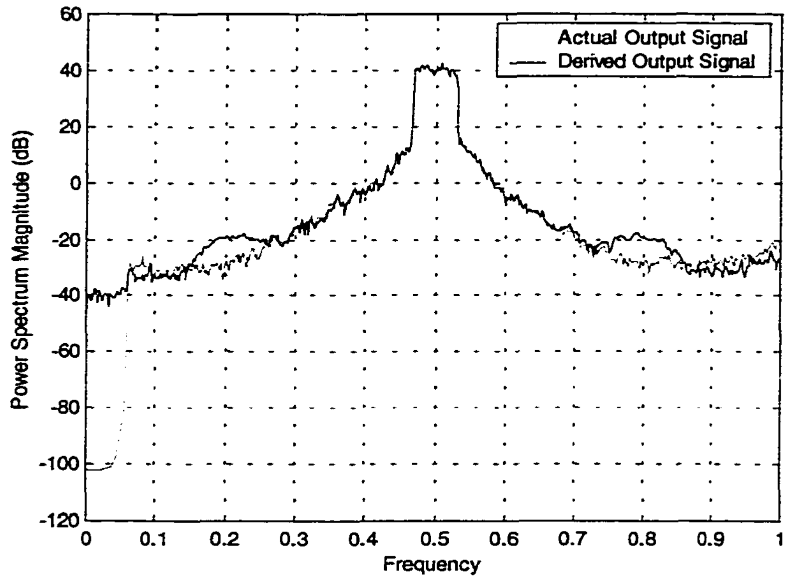

Fig. 32. PSD comparison between actual output signal (light) and output signal derived using 13th order polynomial approximations for both the AM/AM scatter plot and AM/PM scatter plot (dark). First data set.

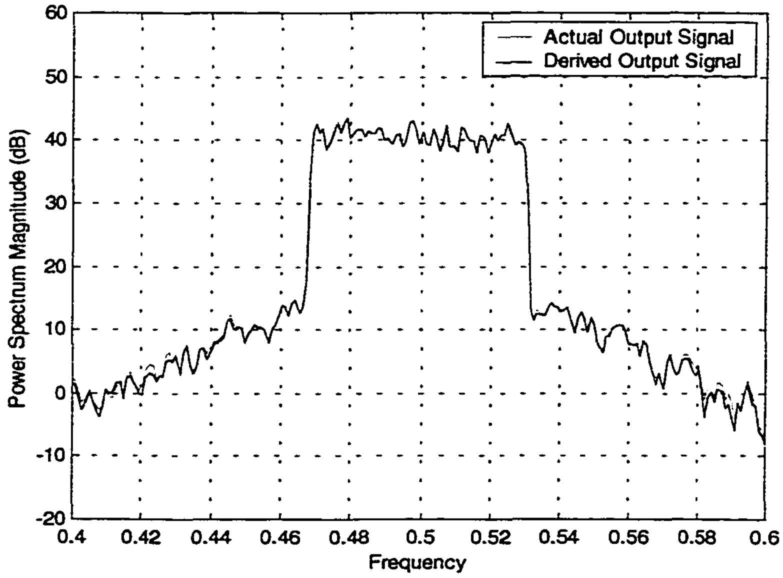

Fig. 33. PSD comparison between actual output signal (light) and output signal derived using 13th order polynomial approximations for both the AM/AM scatter plot and AM/PM scatter plot (dark) limited to a 4 MHz bandwidth around the carrier frequency. First data set.

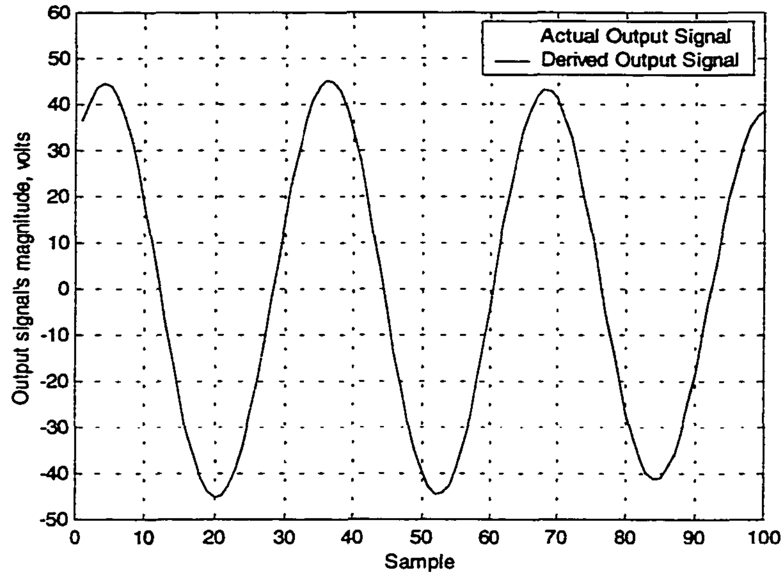

Fig. 34. Time domain comparison between 100 samples of actual output signal (light) and output signal derived using 13th order polynomial approximations for both the AM/AM scatter plot and AM/PM scatter plot (dark). First data set.

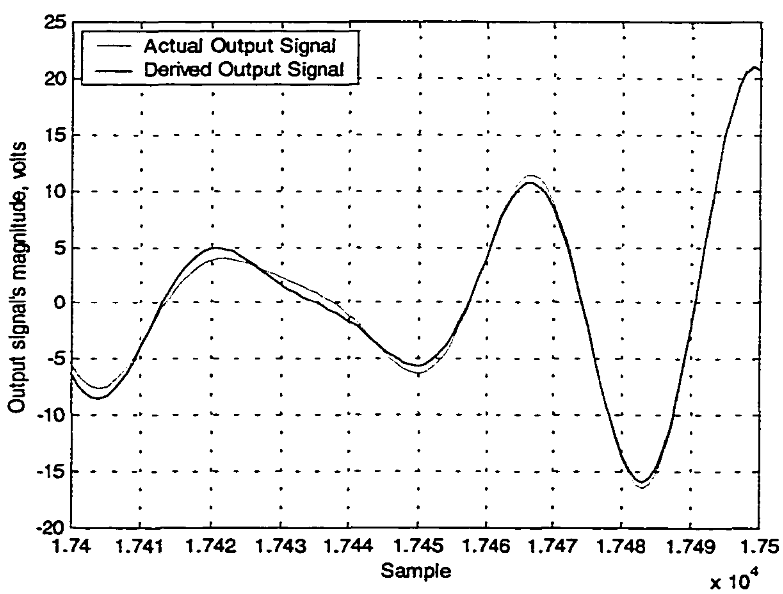

Fig. 35. Time domain comparison between another 100 samples of actual output signal (light) and output signal derived using 13th order polynomial approximations for both the AM/AM scatter plot and AM/PM scatter plot (dark). First data set.

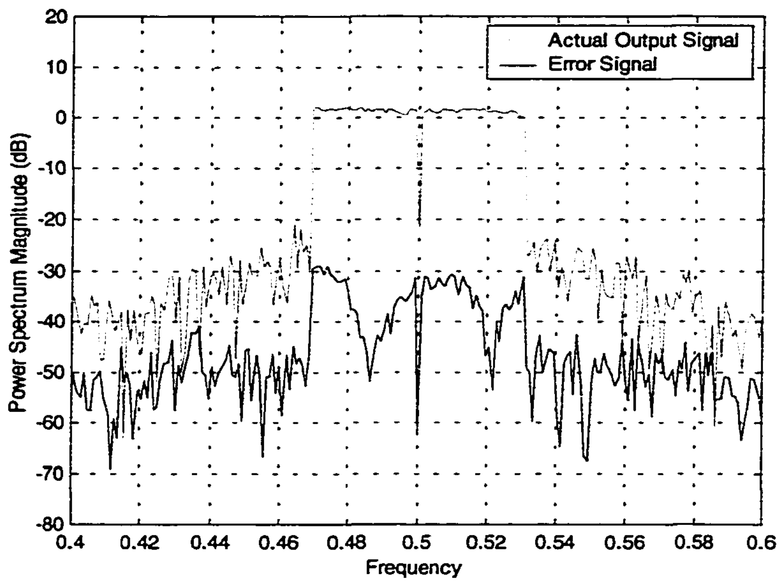

Fig. 36. PSD comparison between actual output signal (light) and error signal derived using 13th order polynomial approximations for both the AM/AM scatter plot and AM/PM scatter plot (dark) limited to a 4 MHz bandwidth around the carrier frequency. First data set.

Table 8 lists the time domain error signals' power, referenced to 50Ω, for various lower order AM/AM scatter plot and AM/PM scatter plot polynomial approximations. The previous comments made concerning the envelope-phase model's sensitivity when using network analyzer derived nonlinear characteristics still apply. Note however that the error signals' power is an order of magnitude less when using the scatter plot derived nonlinear characteristics.

Polynomial Order – AM/AM Scatter Plot	Polynomial Order – AM/PM Scatter Plot	Error Signal's Power, mW
13	13	4.5
13	11	4.5
11	9	4.5
9	7	4.6

Table 8. Error signals' power for various order AM/AM scatter plot and AM/PM scatter plot polynomial approximations. First data set.

The next model test used the second input/output signal data set. The same 13^{th} order polynomial approximations were used and no additional phase shift was required to achieve the lowest error signal power. A PSD comparison between the actual output signal and the derived output signal is shown in Fig. 37. The same PSD comparison limited to a 4 MHz bandwidth around the carrier frequency is shown in Fig. 38. As before, the derived output signal's PSD almost exactly models the actual output signal's PSD within the approximately 1.25 MHz bandwidth of the actual input signal and predicts the actual output signal's sideband regrowth within approximately 1 dB. Time domain comparisons between segments of the actual output signal and the derived output signal are not shown since they are similar to those shown in Figs. 34 and 35. The time domain error signal's maximum value is 3.28 volts and the maximum error signal PSD magnitude is about 30 dB down from that of the actual output signal as shown in Fig. 39. As before, additional model tests were performed using various lower order AM/AM scatter plot and AM/PM scatter plot polynomial approximations with Table 9 listing the time domain error signals' power referenced to 50Ω. Note the order of magnitude reduction in the error signals' power.

Polynomial Order – AM/AM Scatter Plot	Polynomial Order – AM/PM Scatter Plot	Error Signal's Power, mW
13	13	5.6
13	11	5.6
11	9	5.6
9	7	5.7

Table 9. Error signals' power for various order AM/AM scatter plot and AM/PM scatter plot polynomial approximations. Second data set.

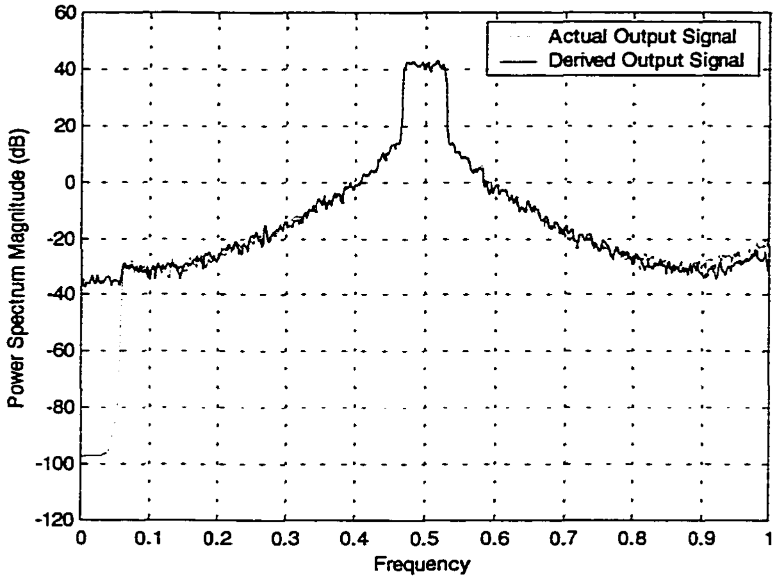

Fig. 37. PSD comparison between actual output signal (light) and output signal derived using 13th order polynomial approximations for both the AM/AM scatter plot and AM/PM scatter plot (dark). Second data set.

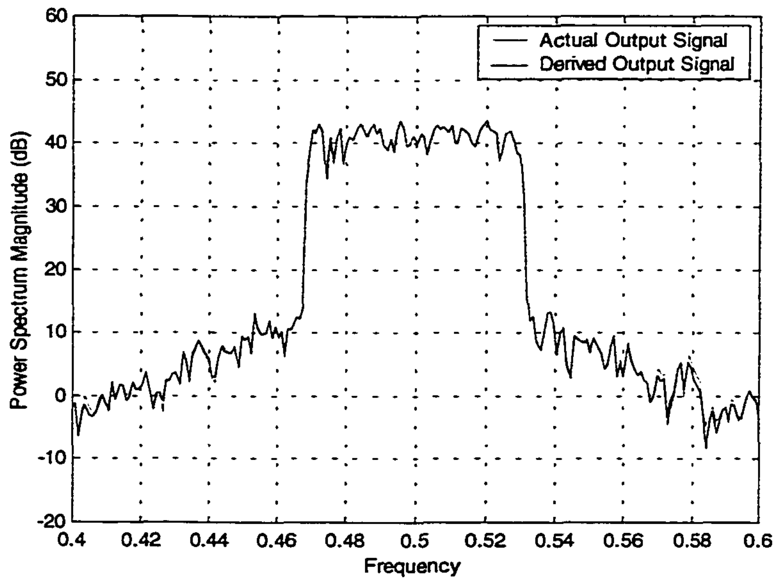

Fig. 38. PSD comparison between actual output signal (light) and output signal derived using 13th order polynomial approximations for both the AM/AM scatter plot and AM/PM scatter plot (dark) limited to a 4 MHz bandwidth around the carrier frequency. Second data set.

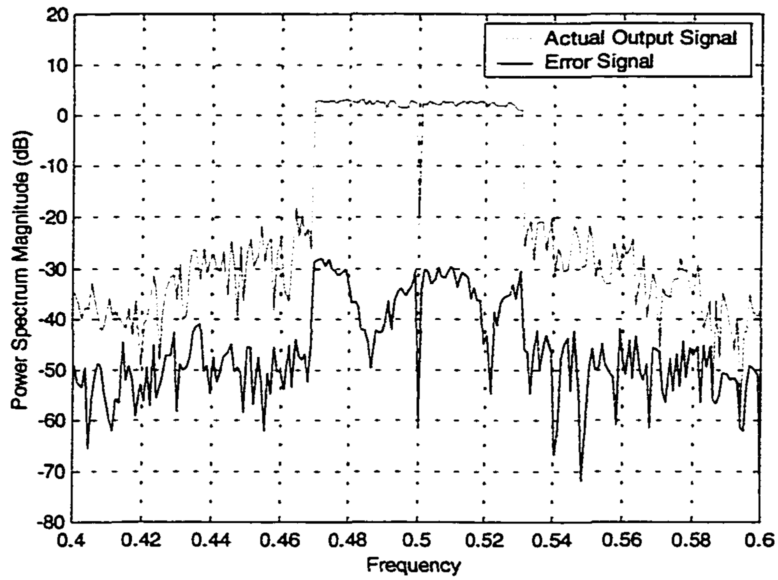

Fig. 39. PSD comparison between actual output signal (light) and error signal derived using 13th order polynomial approximations for both the AM/AM scatter plot and AM/PM scatter plot (dark) limited to a 4 MHz bandwidth around the carrier frequency. Second data set.

Using polynomial approximations of the HPA's AM/AM scatter plot and AM/PM scatter plot instead of its AM/AM conversion and AM/PM conversion derived from network analyzer measurements results in about a 10 dB improvement in the maximum error signal PSD magnitude. The inability to accurately measure phase at low signal magnitudes as evidenced by the rather large variance in the AM/PM scatter plot at low input signal magnitudes is a possible cause of modeling error. Measurement noise is partly to blame for the large variance. This effect can be seen with an input/output signal data set consisting of the same signal. This data set represents the ultimate ultra-linear HPA. The AM/AM scatter plot derived from this input/output data set is a line through the origin with a slope of one. Likewise, the AM/PM scatter is a line through the origin with a slope of zero. Needless to say, the derived output signal is identical to the actual output signal. When additive white Gaussian noise (AWGN) is added to either or both of the input/output signals, the resulting AM/PM scatter plot "broadens out" at low input signal magnitudes. This variance increases with an increase in the magnitude of the AWGN. However, there is a more fundamental reason why the envelope-phase model is not more accurate – memory effects.

The AM/AM scatter plots and AM/PM scatter plots derived from the input/output signal data sets show the presence of hysteresis. Refer to Figs. 40 and 41 for a close-up view of a portion of the AM/AM scatter plot and AM/PM scatter plot derived from the first data set showing the hysteresis in greater detail than the earlier plots in Figs. 27-29. This hysteresis is a manifestation of the HPA's memory effects – modeling the HPA as a memoryless nonlinearity will lead to inaccuracies. The envelope-phase model should provide a better approximation of the HPA's actual output signal than that obtained using polynomial approximations of the AM/AM scatter plot and AM/PM scatter plot if the hysteresis effects could be taken into account. One approach is to use a TDL model to characterize the HPA's AM/AM scatter plot and AM/PM scatter plot.

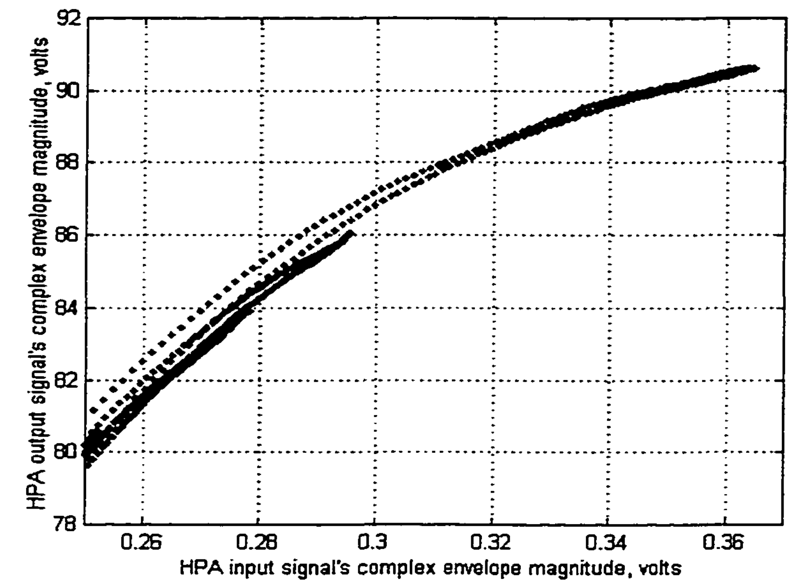

Fig. 40. Portion of AM/AM scatter plot showing hysteresis. First data set.

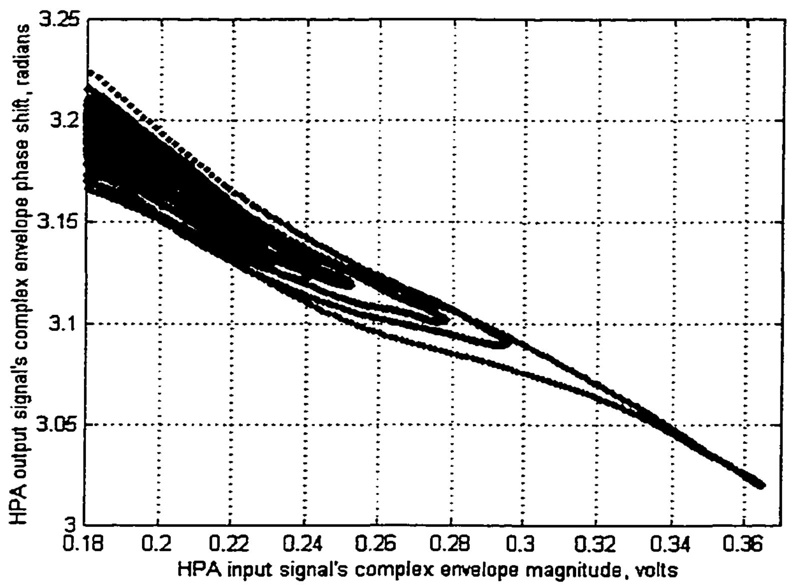

Fig. 41. Portion of AM/PM scatter plot showing hysteresis. First data set.

2.3 TDL MODEL

The envelope-phase model treats an HPA as being a memoryless nonlinearity – it is not. An HPA exhibits memory effects even when driven by a narrowband input signal, especially when the input signal is a high bit rate BPSK signal [21]. A memory model only slightly more complex than the envelope-phase model is the TDL model [22]. The TDL model includes memory, i.e., the present output signal sample is a function of the present input signal sample and previous input signal samples. The TDL model is basically an envelope-phase model that utilizes a sum of polynomial functions of the present input signal sample and previous input signal samples to characterize the HPA's AM/AM scatter plot and AM/PM scatter plot in an approach akin to using multivariate linear regression because the model is *linear in the coefficients* of the polynomials.

The following discussion pertains to an AM/AM scatter plot but is also applicable to an AM/PM scatter plot. The input parameters of the algorithm for fitting a polynomial approximation to the AM/AM scatter plot are the abscissa and ordinate values of the data points comprising the AM/AM scatter plot along with the desired polynomial's order n. The algorithm then computes the polynomial's coefficients such that the polynomial fits the AM/AM scatter plot in a least-squares sense. The input parameters of the algorithm for fitting a TDL model's sum of polynomial approximations to the AM/AM scatter plot also include the abscissa and ordinate values of the points comprising the AM/AM scatter plot along with the desired polynomials' order n. The total number of polynomials is another parameter and it is based on the HPA's memory length. As before, the polynomials' coefficients are computed such that the polynomials fit the AM/AM scatter plot in a least-squares sense. The final parameter determines the number of samples between delayed input samples. For example, if a TDL model is based on the present input sample and ten previous input samples – a memory length of ten – the ten input samples immediately preceding the present input sample can be used. However, a multiplicative factor of five results in the 5^{th}, 10^{th}, ..., 45^{th}, and 50^{th} input samples preceding the present input sample being used. This approach observes the memory effects over a larger time interval without increasing the number of computations needed to find the polynomials' coefficients since the memory length is still ten [22].

The TDL model of an AM/AM scatter plot is shown in Fig. 42. The same model, albeit using different parameters, is used for the AM/PM scatter plot. The following description is for the TDL model of the AM/AM scatter plot – a similar description applies to the AM/PM scatter plot. Referring to Fig. 42, $|\tilde{x}[k]|$ is the current sample of the input signal's complex envelope magnitude. The z^{-1} blocks are unit delays, hence, $|\tilde{x}[k-1]|$ is the previous sample of the input signal's complex envelope magnitude and $|\tilde{x}[k-1]|^2$ is the square of that value. The number of unit delays equals the TDL model's memory length. The ps are the AM/AM scatter plot's polynomials' coefficients found using the technique described in the last paragraph. Combing the constant term in each polynomial forms the constant c_0. The resulting sample of the derived output signal's complex envelope magnitude is $|\tilde{y}[k]|$. When modeling the AM/PM scatter plot, the ps are the AM/PM scatter plot's polynomials' coefficients and the summer's output is the derived output signal's complex envelope phase.

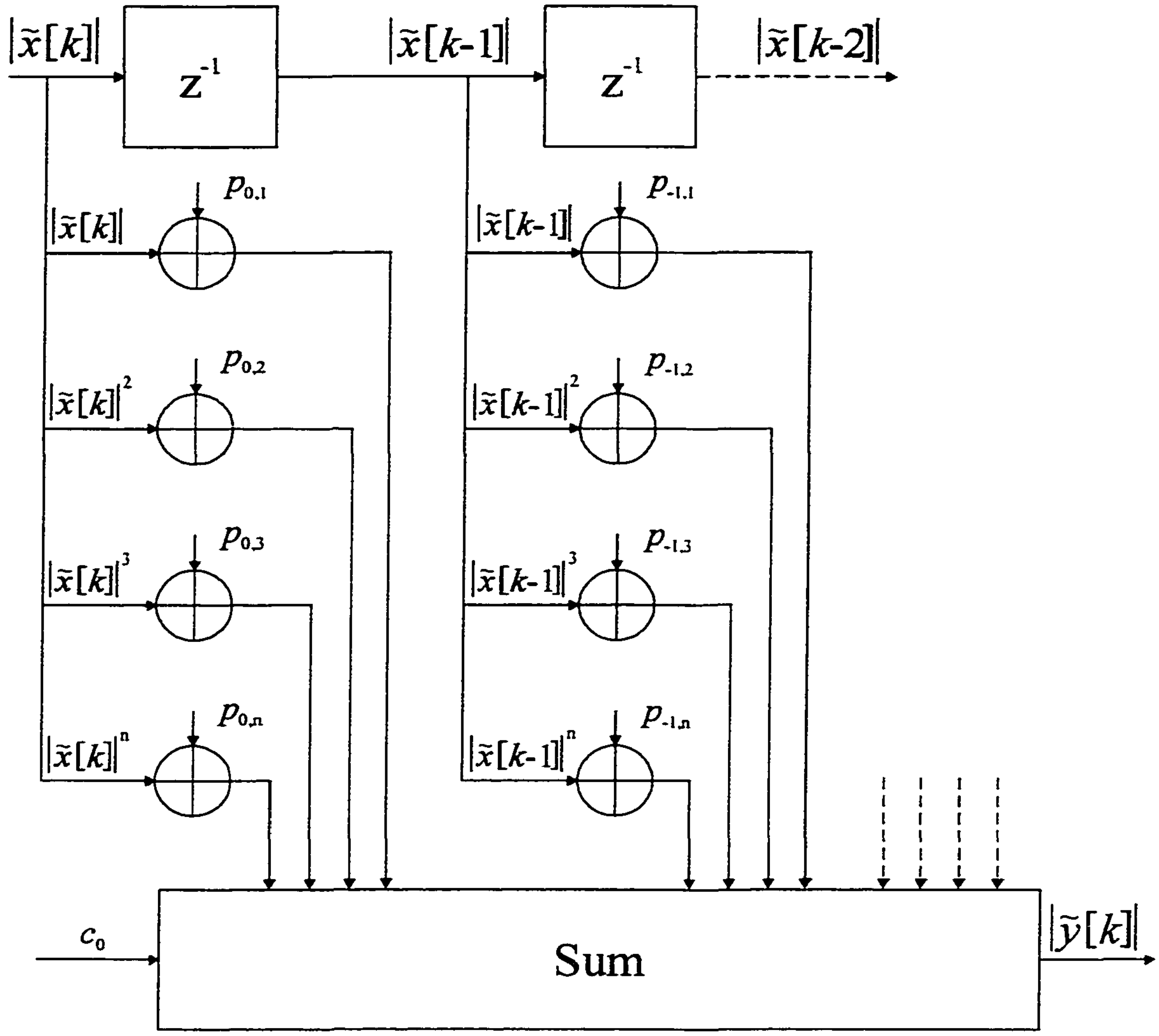

Fig. 42. TDL model of AM/AM scatter plot.

Henceforth, the term TDL model will designate an envelope-phase model utilizing a sum of polynomial functions of the present input signal sample and previous input signal samples to characterize the HPA's AM/AM scatter plot and AM/PM scatter plot unless the context indicates otherwise. For example, the modeled AM/AM (AM/PM) scatter plot may be referred to as the TDL model of the AM/AM (AM/PM) scatter plot or simply the TDL AM/AM (AM/PM) approximation. The TDL model performance was tested using the first input/output signal data set. Note that the TDL model and the envelope-phase model have both been tested using numerous data sets having different peak-to-average power ratios and average power levels. The particular data sets used in this dissertation were chosen for illustrative purposes and the other data sets produced similar results to those presented herein.

Previously, 13^{th} order polynomial approximations were chosen to represent the HPA's AM/AM (AM/PM) conversion and AM/AM (AM/PM) scatter plot. Therefore, a series of 13^{th} order TDL approximations was fitted to the AM/AM scatter plot and AM/PM scatter plot for comparison. Since a TDL approximation requires more input parameters than a polynomial approximation, the following notation is used to represent a TDL approximation: PolynomialOrder_MemoryLength_MultiplicativeFactor. The TDL approximation 13_8_16, for example, consists of nine 13^{th} order polynomial approximations, one polynomial approximation corresponding to the present input signal sample and eight polynomial approximations corresponding to eight previous input signal samples, where all input signal samples are separated by sixteen samples. The TDL AM/AM approximation 13_0_0 is the standard 13^{th} order polynomial approximation of the AM/AM scatter plot. Tables 10 and 11 list the error signals' power, referenced to 50Ω, for various TDL AM/AM approximations and TDL AM/PM approximations of the AM/AM scatter plot and AM/PM scatter plot, respectively. A few trends are apparent from examining the tables.

TDL AM/AM Model Parameters	Error Signal's Power, mW
13_0_0	2.9
13_1_1	2.8
13_1_8	2.8
13_1_16	2.8
13_1_32	2.7
13_4_1	2.7
13_4_8	2.7
13_4_16	2.7
13_4_32	2.6
13_8_1	2.7
13_8_8	2.6
13_8_16	2.6
13_8_32	2.6
13_8_64	2.5
7_1_32	2.8

Table 10. Error signals' power for various order TDL AM/AM approximations. First data set.

TDL AM/PM Model Parameters	Error Signal's Power, μW
13_0_0	20.1
13_1_1	15.7
13_1_2	15.9
13_1_4	16.0
13_1_8	16.1
13_4_1	14.7
13_4_2	15.3
13_4_4	15.5
13_4_8	15.6
13_8_1	14.4
13_8_2	15.1
13_8_4	15.4
13_8_8	15.5
7_1_1	16.4

Table 11. Error signals' power for various order TDL AM/PM approximations. First data set.

The most important conclusion is that the TDL approximations are more accurate than the polynomial approximations – more so in the case of the TDL AM/PM approximations. The best TDL AM/AM approximation results in a 0.6 dB reduction in error signal power compared to the polynomial approximation and the best TDL AM/PM approximation results in a 1.4 dB reduction. Each of these TDL approximations uses a memory length of eight. Note however that using the minimum memory length of one still results in about a 0.2 and 1.1 dB reduction in error signal power for the TDL AM/AM approximation and TDL AM/PM approximation, respectively. In general, increasing the memory length decreases the error signal power. Increasing the multiplicative factor of the TDL AM/AM approximation tends to decrease the error signal power while increasing the multiplicative factor of the TDL AM/PM approximation increases the error signal power. A possible explanation for this behavior is that the input (output) signal's complex envelope phase has a higher rate-of-change between samples than does the signal's complex envelope magnitude. In addition, 7^{th} order TDL approximations of the AM/AM scatter plot and AM/PM scatter plot, each having memory length one, were included to gauge the effect of using lower order polynomial approximations. These TDL approximations still result in about a 0.2 and 0.9 dB reduction in error signal power for the TDL AM/AM approximation and TDL AM/PM approximation, respectively.

Recall the close-up views of a portion of the HPA's AM/AM scatter plot and AM/PM scatter plot shown in Figs. 40 and 41, respectively. The hysteresis was as obvious as the inability of a simple polynomial approximation to model it. A comparison between the portion of the AM/AM scatter plot shown in Fig. 40 and the TDL AM/AM approximation 13_8_64 is shown in Fig. 43. The TDL AM/AM approximation clearly models the hysteresis – at least at high input signal magnitudes. A comparison between the portion of the AM/PM scatter plot shown in Fig. 41 and the TDL AM/PM approximation 13_8_1 is shown in Fig. 44. The TDL AM/PM approximation models the hysteresis but tends to oscillate at high input signal magnitudes. The TDL AM/PM approximation did not require the addition of any constant value of phase shift to each data sample to overlay the AM/PM scatter plot. Note that the error signals referred to in this and the preceding paragraphs are the difference between the AM/AM scatter plot and AM/PM scatter plot and their respective TDL model approximations.

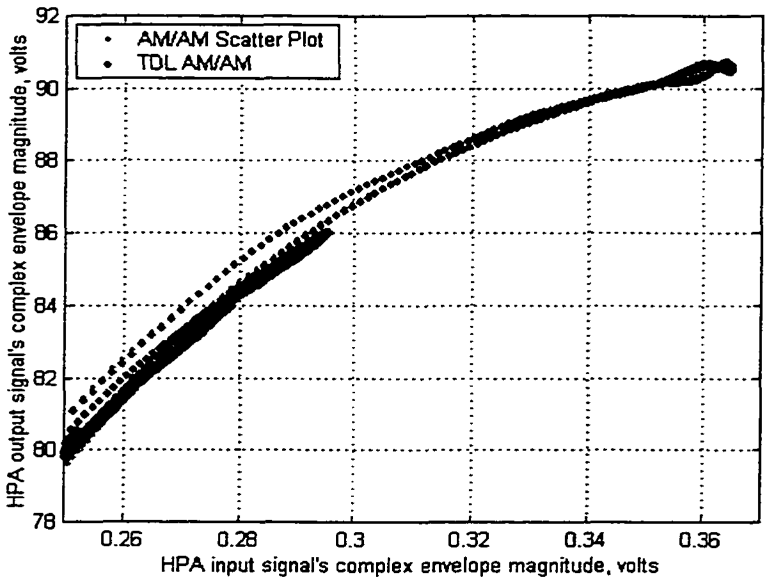

Fig. 43. Comparison between portion of AM/AM scatter plot showing hysteresis (light) and TDL AM/AM approximation 13_8_64 (dark). First data set.

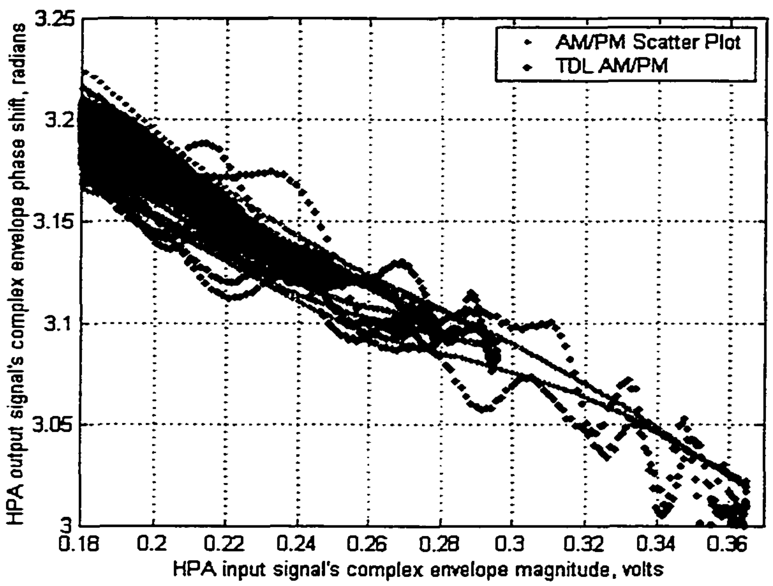

Fig. 44. Comparison between portion of AM/PM scatter plot showing hysteresis (light) and TDL AM/PM approximation 13_8_1 (dark). First data set.

The next model test used the first input/output signal data set and TDL AM/AM approximation 13_8_64 of the AM/AM scatter plot and TDL AM/PM approximation 13_8_1 of the AM/PM scatter plot. No additional phase shift was required to achieve the lowest error signal power. A PSD comparison between the actual output signal and the derived output signal is shown in Fig. 45. The same PSD comparison limited to a 4 MHz bandwidth around the carrier frequency is shown in Fig. 46. The derived output signal's PSD almost exactly models the actual output signal's PSD within the approximately 1.25 MHz bandwidth of the actual input signal. The derived output signal's PSD also predicts the actual output signal's sideband regrowth within approximately 1 dB. These results are almost identical to those shown in Figs. 32 and 33 for the scatter plot derived nonlinear characteristics with the exception that the PSD of the output signal derived from the TDL model nonlinear characteristics is not as good a match to the actual output signal's PSD well outside the bandwidth of interest. A time domain comparison between the same two 100 sample segments of the actual output signal and the derived output signal shown in Figs. 34 and 35 for the scatter plot derived nonlinear characteristics is shown in Figs. 47 and 48 for the TDL model derived nonlinear characteristics. The results are essentially identical for these two 100 sample segments regardless of which nonlinear characteristics are used. The time domain error signal's power is 2.7 mW and its maximum value is 2.87 volts. These values are 1.8 mW lower and 0.05 volts higher than they were for the scatter plot derived nonlinear characteristics. The maximum error signal PSD magnitude is about 32 dB down from that of the actual output signal as shown in Fig. 49 – a 2 dB improvement over the error signal shown in Fig. 36 for the scatter plot derived nonlinear characteristics.

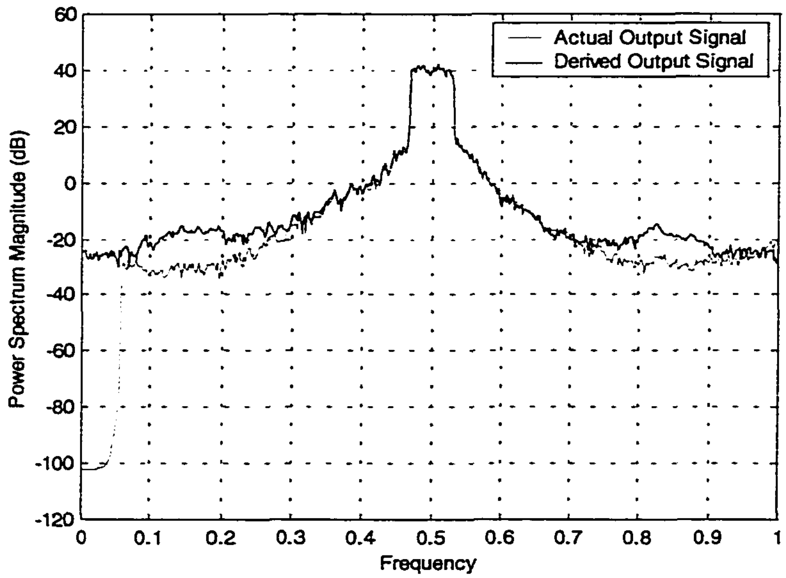

Fig. 45. PSD comparison between actual output signal (light) and output signal derived using TDL AM/AM approximation 13_8_64 and TDL AM/PM approximation 13_8_1 (dark). First data set.

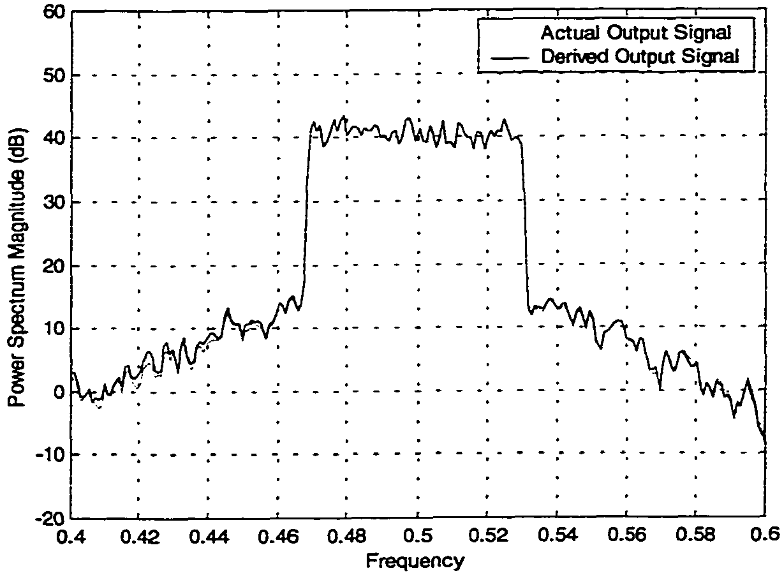

Fig. 46. PSD comparison between actual output signal (light) and output signal derived using TDL AM/AM approximation 13_8_64 and TDL AM/PM approximation 13_8_1 (dark) limited to a 4 MHz bandwidth around the carrier frequency. First data set.

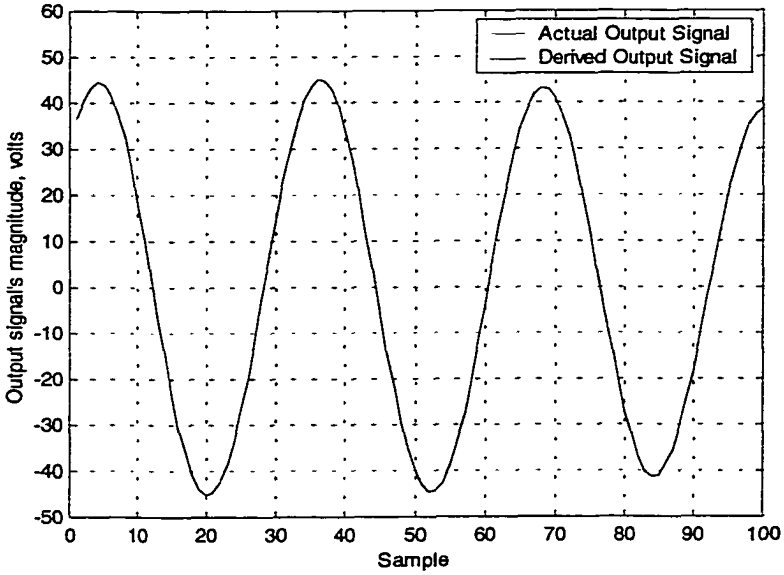

Fig. 47. Time domain comparison between 100 samples of actual output signal (light) and output signal derived using TDL AM/AM approximation 13_8_64 and TDL AM/PM approximation 13_8_1 (dark). First data set.

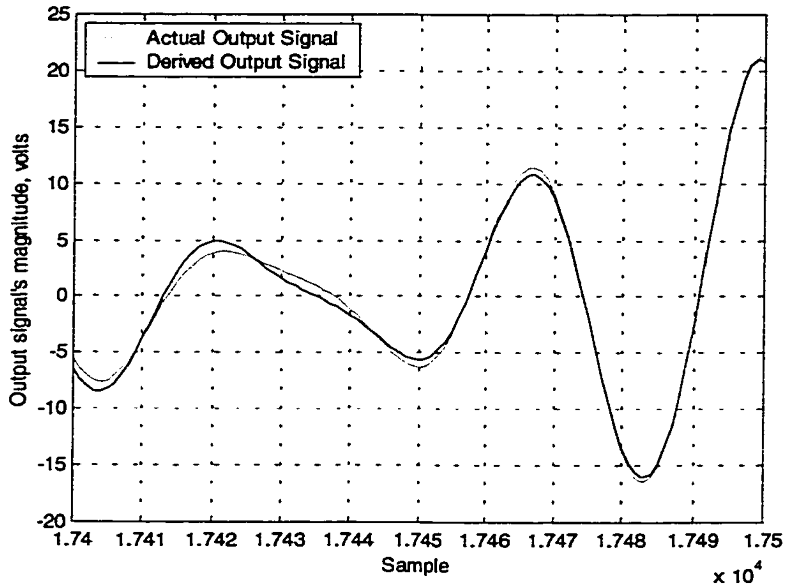

Fig. 48. Time domain comparison between another 100 samples of actual output signal (light) and output signal derived using TDL AM/AM approximation 13_8_64 and TDL AM/PM approximation 13_8_1 (dark). First data set.

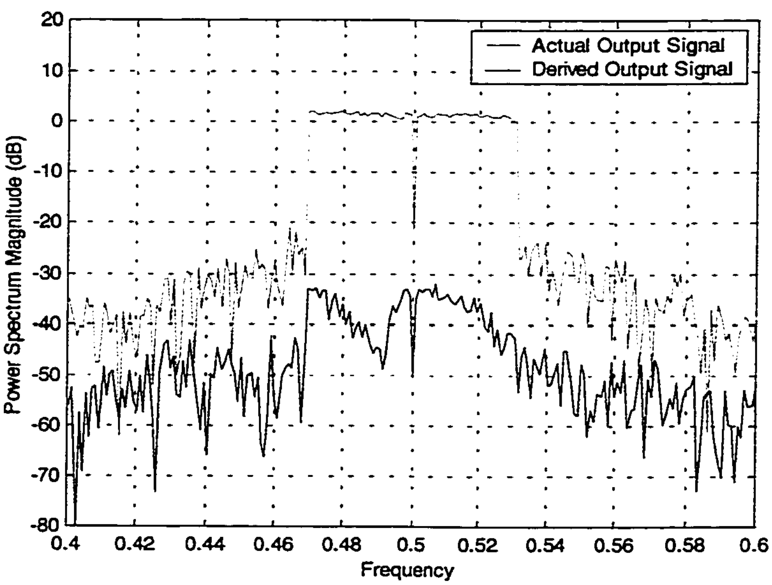

Fig. 49. PSD comparison between actual output signal (light) and error signal derived using TDL AM/AM approximation 13_8_64 and TDL AM/PM approximation 13_8_1 (dark) limited to a 4 MHz bandwidth around the carrier frequency. First data set.

The final model test used the first input/output signal data set and TDL AM/AM approximation 7_1_32 of the AM/AM scatter plot and TDL AM/PM approximation 7_1_1 of the AM/PM scatter plot to gauge the effect of using lower order polynomial approximations and minimum memory length. As before, no additional phase shift was required to achieve the lowest error signal power. A PSD comparison between the actual output signal and the derived output signal is shown in Fig. 50. Note that the derived output signal's PSD is a better match to the actual output signal's PSD well outside the bandwidth of interest than the previous results shown in Fig. 45 for the TDL AM/AM approximation 13_8_64 and TDL AM/PM approximation 13_8_1. Time domain comparisons between segments of the actual output signal and the derived output signal are not shown since they are similar to those shown in Figs. 47 and 48. The time domain error signal's power is 2.9 mW and its maximum value is 2.31 volts. These values are 0.2 mW higher and 0.52 volts lower than they were for the TDL AM/AM approximation 13_8_64 and TDL AM/PM approximation 13_8_1. The maximum error signal PSD magnitude is about 31 dB down from that of the actual output signal as shown in Fig. 51 – 1 dB worse than the error signal shown in Fig. 49 for the TDL AM/AM approximation 13_8_64 and TDL AM/PM approximation 13_8_1.

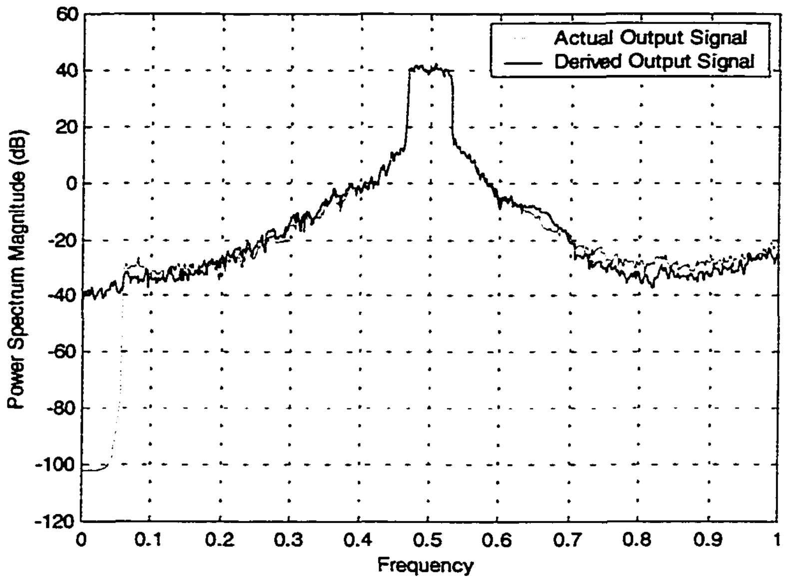

Fig. 50. PSD comparison between actual output signal (light) and output signal derived using TDL AM/AM approximation 7_1_32 and TDL AM/PM approximation 7_1_1 (dark). First data set.

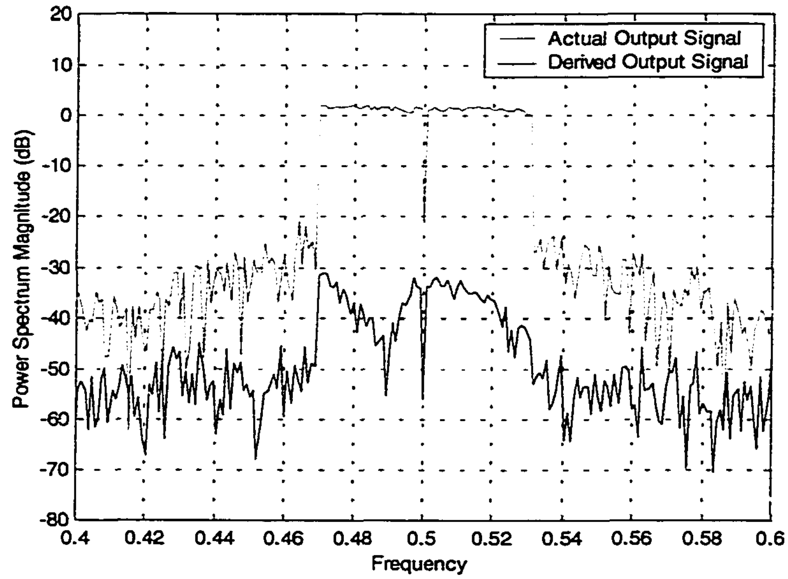

Fig. 51. PSD comparison between actual output signal (light) and error signal derived using TDL AM/AM approximation 7_1_32 and TDL AM/PM approximation 7_1_1 (dark) limited to a 4 MHz bandwidth around the carrier frequency. First data set.

An error analysis was performed to determine if any discernible pattern could be found concerning modeling errors. The approach is to plot the error signal's power (complex envelope magnitude squared divided by fifty), both absolute and normalized, vs. the input signal's complex envelope magnitude using a histogram-like plot. The objective is to determine whether the errors are localized or evenly distributed throughout the input signal's range. A histogram of the HPA's input signal's complex envelope magnitude using 250 bins is shown in Fig. 52. The error signal was formed by subtracting the actual output signal's complex envelope magnitude from the output signal's complex envelope magnitude derived using the TDL AM/AM approximation 13_8_64 and TDL AM/PM approximation 13_8_1. Histograms of the absolute error power and normalized error power, both using 250 bins, are shown in Figs. 53 and 54, respectively. The input signal's complex envelope magnitude histogram is very similar to the absolute error power's histogram, i.e., the absolute error power appears to be proportional to the number of samples occurring within a given range of the input signal's complex envelope magnitude. The normalized error power has a more uniform distribution with the exception of the upper range of the input signal's complex envelope magnitude. This indicates that the TDL model is less accurate when the input signal is in the compression region of the HPA's gain characteristic (> 0.25 volts) as shown in Fig. 30. Similar results were observed for the envelope-phase model using either the network analyzer derived nonlinear characteristics or scatter plot derived nonlinear characteristics.

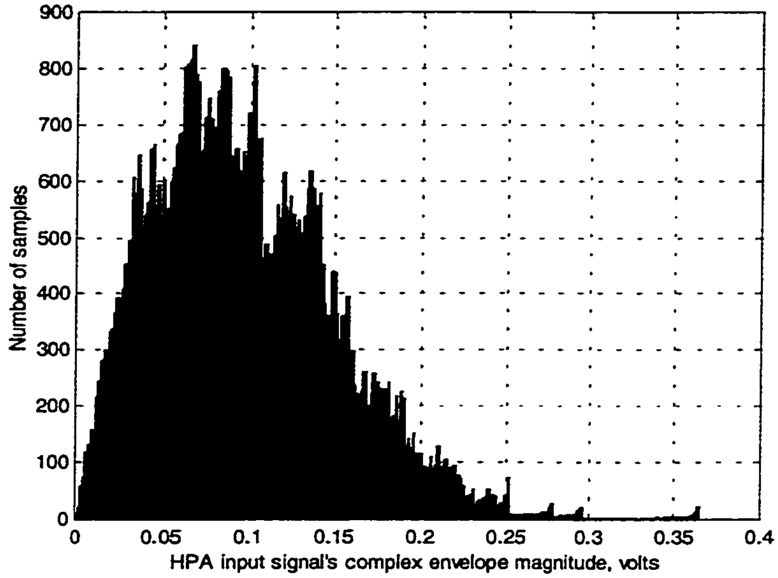

Fig. 52. Histogram of HPA's input signal's complex envelope magnitude using 250 bins. First data set.

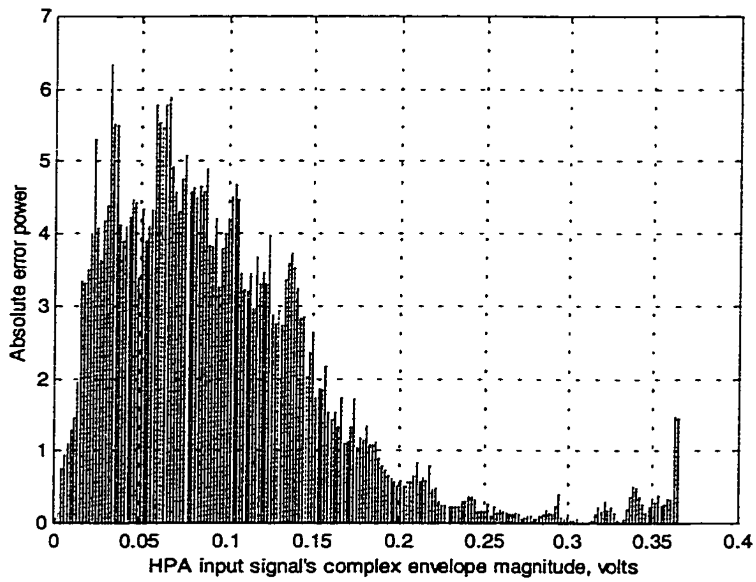

Fig. 53. Histogram of absolute error power for the TDL AM/AM approximation 13_8_64 and TDL AM/PM approximation 13_8_1 using 250 bins. First data set.

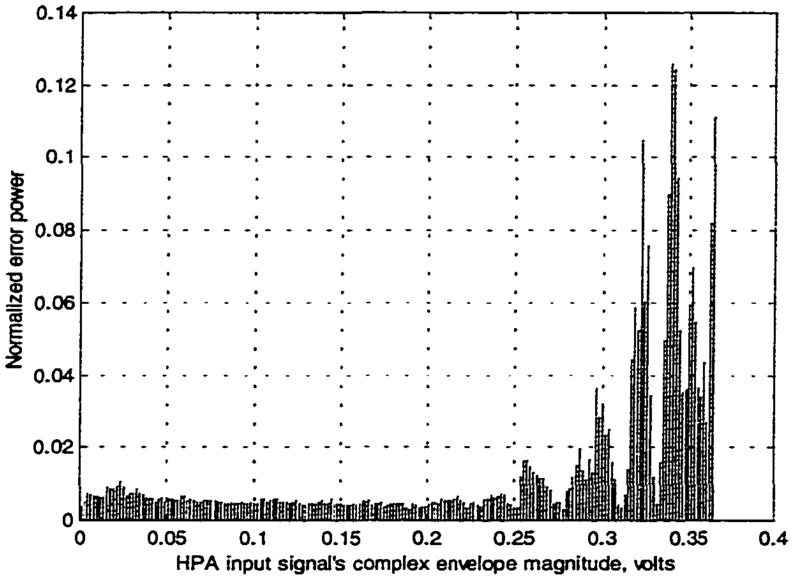

Fig. 54. Histogram of normalized error power for the TDL AM/AM approximation 13_8_64 and TDL AM/PM approximation 13_8_1 using 250 bins. First data set.

Further research could be conducted concerning optimum values for, and interactions among, the TDL model parameters: polynomial order, memory length, and multiplicative factor. For example, could a TDL model having a lower polynomial order than a simple polynomial approximation of a scatter plot provide the same or more accuracy since memory effects are included? The optimal memory length is another area of investigation. The memory length must be long enough to capture the HPA's memory effects but not too long. Both the polynomial order and memory length cannot be arbitrarily large as this greatly increases computation time and introduce inaccuracies. There is probably interaction among the three TDL model parameters and finding the optimum value for each will not be a trivial matter.

Improving the TDL model's accuracy is the subject of current research to be reported in [24]. The introduction of two linear filters into the TDL model results in about a 10 dB improvement in the maximum error signal PSD magnitude. Specifically, the input signal's complex envelope is filtered by one linear filter before the HPA's AM/AM scatter plot and AM/PM scatter plot are derived. The TDL model is then implemented as described previously with the output signal's complex envelope being filtered by the second linear filter. The filtered TDL model requires two additional model parameters: the number of taps for each filter. Like the TDL model in general, there does not appear to be a systematic procedure for picking the combination of model parameters that results in the most accurate filtered TDL model implementation given a particular input/output signal data set.

The TDL model, either the basic or filtered version, is more accurate than the envelope-phase model using either the network analyzer derived nonlinear characteristics or scatter plot derived nonlinear characteristics. Nevertheless, the envelope-phase model using scatter plot derived nonlinear characteristics was used in the IS-2000 forward link simulations to be presented in a later chapter. The envelope-phase model using scatter plot derived nonlinear characteristics is almost as accurate as the basic TDL model within the bandwidth of interest as seen by comparing Figs. 33 and 46. In addition, both models are equally accurate at predicting the output signal's sideband regrowth – an important consideration as will be seen in the following chapter. Although less important, the envelope-phase model is faster than the TDL model with an execution speed proportional to the memory length. This is not inconsequential as an IS-2000 forward link simulation can take up to ten days to run on a Pentium MMX 200 MHz personal computer having 128 MB of memory.

CHAPTER 3 HPA COMPENSATION

In the last chapter an HPA's nonlinear characteristics were represented by its AM/AM scatter plot (conversion) and AM/PM scatter plot (conversion). These nonlinear characteristics visually convey the HPA's deviation from a *perfectly* linear amplifier having linear gain and a constant phase shift. Compensation (linearization) helps abate an HPA's nonlinear behavior while still allowing the HPA to operate efficiently. Two of the more popular compensation techniques are feedforward linearization and digital baseband predistortion. This chapter begins by examining an HPA's nonlinear behavior. The popular compensation techniques are then discussed with an emphasis on digital baseband techniques. The chapter concludes with a detailed analysis of one of these techniques – a digital baseband predistorter based on the "fixed point" approach.

3.1 COMPENSATION TECHNIQUES

It was noted earlier that an HPA's nonlinear behavior causes generation of co-channel and adjacent channel interference due to IMD and spectral regrowth of the sidebands. Sideband regrowth is not only a technical issue but a regulatory concern as well. Sideband regrowth is also easy to observe as seen in Fig. 55. This example and the compensation tests presented later in this chapter use the first input/output signal data set as modified by scaling the output signal's average power to the same level as the input signal's. This results in the HPA's AM/AM scatter plot having approximately unity gain in its linear region as shown in Fig. 56. The AM/PM scatter plot remains unchanged from that shown in Fig. 28.

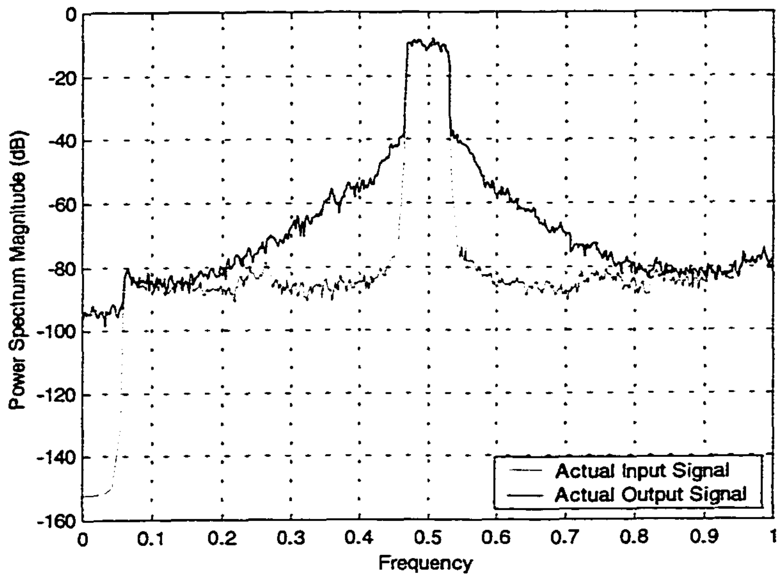

Fig. 55. PSD comparison between actual input signal (light) and actual output signal (dark) showing spectral regrowth of the sidebands. First data set (modified).

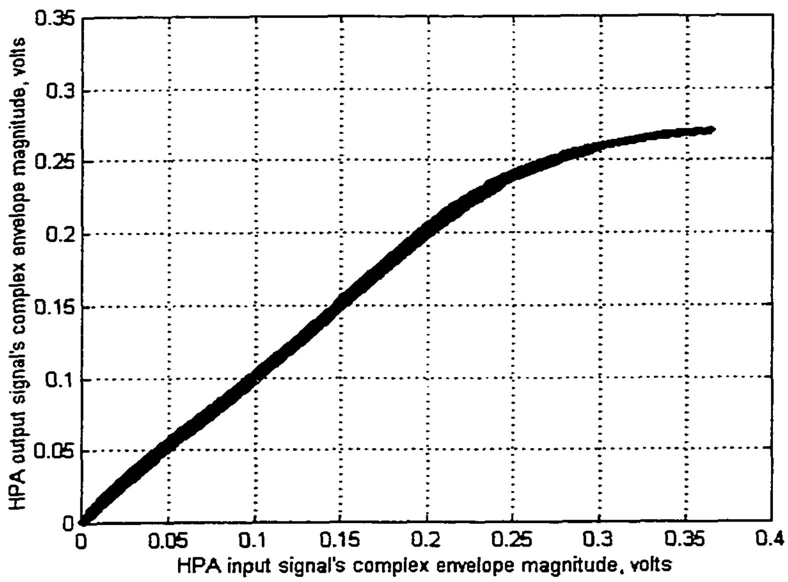

Fig. 56. AM/AM scatter plot. First data set (modified).

Employing HPA compensation can reduce sideband regrowth and IMD. Two of the more popular compensation schemes are feedforward linearization and predistortion. A rudimentary feedforward linearizer does not require an HPA model. The feedforward linearizer operates by first subtracting a delayed version of the HPA's input signal from an attenuated version of the HPA's output signal, thus forming an error signal. The error signal is then amplified in an auxiliary amplifier and subtracted from a delayed version of the HPA's output signal to form a more or less undistorted output signal. The feedforward linearizer is broadband and provides a high level of linearity [25] but is less efficient than other compensation schemes due to losses in its delay paths, couplers, and auxiliary amplifier [9]. The feedforward linearizer, as well as many other compensation schemes, suffers degraded performance due to temperature fluctuations, component aging, supply voltage fluctuations, etc. To combat these environmental variables the feedforward linearizer is made adaptive. Some adaptive feedforward linearizers utilize an HPA model [26]-[27].

Predistortion is another popular compensation scheme that is more efficient than feedforward linearization and capable of providing good broadband operation [25]. The essence of predistortion is to precede an HPA with a nonlinearity having nonlinear behavior that is the inverse of the HPA's nonlinear behavior. Predistorters are classified as either analog or digital. Analog predistorters operate at RF such as the 3^{rd} order polynomial predistorter described in [25]. Digital predistorters operate at baseband and are therefore more attractive than analog predistorters. An example of a digital predistorter is the adaptive gain based predistorter (AGBPD) found in [28]. As was the case with a feedforward linearizer, an adaptive digital predistorter can compensate for environmental variables. An excellent review of different linearization techniques provided in an historical context is found in [9].

Cavers' AGBPD has been thoroughly studied and is the basis for other adaptive digital predistorters [29]-[32]. The AGBPD handles any modulation format and order of HPA nonlinearity. It requires much less memory than earlier digital predistorters and has greatly reduced convergence time. In the block diagram of an AGBPD shown in Fig. 57, $\tilde{x}[k]$ is the desired modulation (i.e., input signal), $\tilde{x}_d[k]$ is the predistorted version of $\tilde{x}[k]$, and $\tilde{y}[k]$ is the actual HPA output signal. The lookup table (LUT) is addressed by the squared magnitude of $\tilde{x}[k]$. The LUT's output is the complex gain by which $\tilde{x}[k]$ is multiplied to yield $\tilde{x}_d[k]$. Ideally, when $\tilde{x}_d[k]$ is amplified by the HPA, thus undergoing nonlinear distortion, the resulting output signal $\tilde{y}[k]$ is a constant multiple of $\tilde{x}[k]$. The LUT is updated by ADAPT which compares a delayed version of $\tilde{x}[k]$ with $\tilde{y}[k]$, i.e., adaptation is accomplished by minimizing the error signal [28].

An AGBPD is a vast improvement over earlier digital predistorters in terms of memory requirement and convergence speed, however, this increased performance is obtained at the expense of increased computations. Despite the improvement over earlier digital predistorters, the AGBPD is not suitable for CDMA signals conforming to the IS-95 standard. The AGBPD was designed primarily for single-carrier systems employing relatively narrowband signals modulated using 16-QAM or QPSK, for example. The AGBPD in [28] was implemented on a Texas Instruments TMS320C25 and has a nominal bandwidth of 30 kHz. The adaptive digital predistorter described in [29] was also implemented on a Texas Instruments TMS320C25 for a system using π/4-shifted DQPSK running at 2000 bits/s. The nominal bandwidth of this single-carrier system is approximately 3 kHz. Neither of these implementations involved multicarrier systems such as orthogonal frequency-division multiplexing (OFDM) and multicarrier CDMA (MC-CDMA) or wideband systems such as IS-95 and IS-2000.

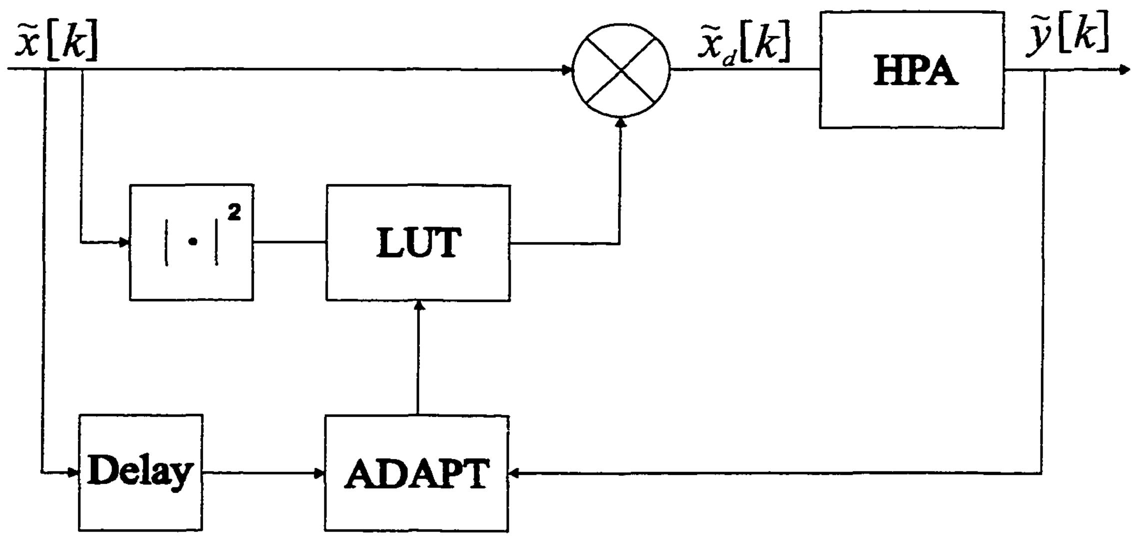

Fig. 57. Adaptive gain based predistorter from [28].

Adaptive digital predistortion techniques using small lookup tables to modify the signal constellation of a single-carrier system are not suitable for compensating an OFDM system because the HPA in an OFDM system is fed by an input signal possibly having an infinite number of amplitude levels whereas the single-carrier system has an input signal having a finite number of amplitude levels [33]. Moreover, updating the lookup table requires an additional QAM demodulator and fast updating is problematical [34]. As a result of the shortcomings of an AGBPD vis-à-vis multicarrier and wideband systems, a new digital predistorter based on the fixed point approach was developed for OFDM systems [34].

3.2 FIXED POINT PREDISTORTION

OFDM systems are used to transmit digital terrestrial broadcasting such as digital HDTV [33]. They employ several orthogonal subcarriers, modulated using QAM or PSK and amplified using a TWTA, to transmit the data. The FFT and inverse FFT (IFFT) algorithms are used to efficiently implement OFDM receivers and transmitters, respectively. Using a digital predistorter based on the fixed point approach can compensate for the TWTA's nonlinear behavior. But what is a "fixed point"? Mathematically, a point x is a fixed point of an arbitrary transformation $T(\cdot)$ if x is invariant under the transformation, i.e., $x = T(x)$. A fixed point may not be unique or even exist for an arbitrary transformation. However, if the transformation is a *contraction mapping*, a unique fixed point exists and can be found using an iterative process [34]. The detailed description of a fixed point based digital predistorter in this and the following paragraphs is based on that given in [34] and uses a slightly modified version of the notation found therein.

Defining a TWTA's nonlinear characteristics as $N(\cdot)$ yields a discrete version of the memoryless nonlinear amplifier model of (41) given by

$$\tilde{y}[k] = g(|\tilde{x}[k]|)e^{j[p(|\tilde{x}[k]|)+\angle(\tilde{x}[k])]} = N(\tilde{x}[k]), \tag{44}$$

where $\tilde{y}[k]$ and $\tilde{x}[k]$ are samples of the TWTA's output and input signals' complex envelope, respectively, and the AM/AM conversion $g(\cdot)$ and AM/PM conversion $p(\cdot)$ depend only on the modulus (magnitude) of the input signal's complex envelope [3] and are calculated using Saleh's rational polynomials (42)-(43). The objective of predistortion is described by

$$g_0 \cdot \tilde{x}[k] = N(\tilde{x}_d[k]), \tag{45}$$

where g_0 is the TWTA's desired linear gain and $\tilde{x}_d[k]$ is the desired predistorted signal's complex envelope. The selection of gain g_0 is based on the particular AM/AM conversion and AM/PM conversion being linearized.

Consider the transformation $T(\cdot)$ given by

$$T(\tilde{x}_d[k]) = \tilde{x}_d[k] + \alpha[g_0 \cdot \tilde{x}[k] - N(\tilde{x}_d[k])], \tag{46}$$

where α is a constant. If the predistorted signal $\tilde{x}_d[k]$ is a fixed point of $T(\cdot)$, then (45) is satisfied. In other words, finding the fixed point of $T(\cdot)$, assuming it exists and is unique, provides the desired predistorted signal. Fortunately, given the TWTA's nonlinear characteristics $N(\cdot)$ as described above, there exists an appropriate α which ensures $T(\cdot)$ is a contraction mapping, hence, $T(\cdot)$ has a unique fixed point. That unique fixed point of $T(\cdot)$, and consequently the desired predistorted signal $\tilde{x}_d[k]$, can be found using an iterative process given in [34] by

$$\tilde{x}_{i+1}[k] = T(\tilde{x}_i[k]) = \tilde{x}_i[k] + \alpha[g_0 \cdot \tilde{x}_0[k] - N(\tilde{x}_i[k])], \tag{47}$$

where $i = 0, 1, 2, \ldots$ and $\tilde{x}_0[k] \equiv \tilde{x}[k]$. Thus, a fixed point based digital predistorter for an OFDM system is obtained by implementing the iterative process defined in (47).

Note that the fixed point predistorter is non-adaptive because it relies on a static model of the TWTA's nonlinear characteristics. Consequently, the compensation provided by a fixed point predistorter is only as good as the underlying nonlinear model – an inaccurate nonlinear model leads to suboptimal compensation. Although the fixed point predistorter was designed to compensate an OFDM system, it should function properly in an MC-CDMA system [33] and by extension in a wideband system such as IS-95 or IS-2000.

The fixed point predistorter designed to compensate OFDM systems (OFDMPD) is the basis for a digital baseband predistorter (FPPD) for CDMA signals developed as part of the research for this dissertation. The OFDMPD uses a TWTA's nonlinear characteristics $N(\cdot)$ derived from Saleh's rational polynomials. The FPPD incorporates an envelope-phase model using scatter plot derived HPA nonlinear characteristics for $N(\cdot)$ instead of relying on Saleh's model. This generalized approach of using scatter plot derived nonlinear characteristics allows the FPPD to compensate TWTAs as well as solid-state HPAs since Saleh's model is not valid for modeling solid-state HPAs. The block diagram in Fig. 58 shows the location of the FPPD with respect to the HPA.

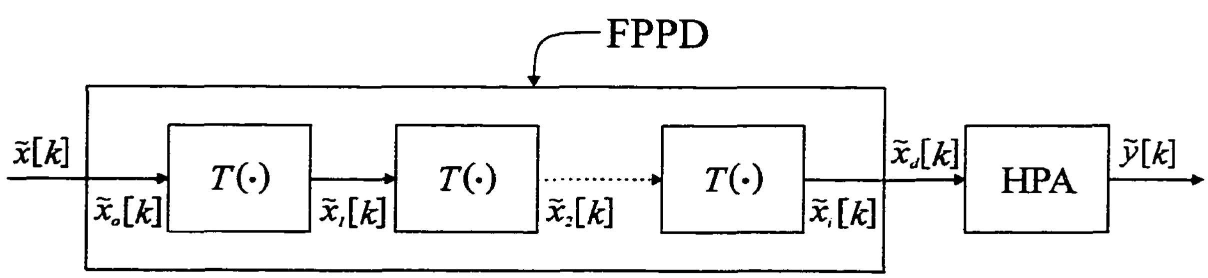

Fig. 58. Fixed point predistorter from [34].

The statement was made in [34] that there exists an appropriate α which ensures that $T(\cdot)$ is a contraction mapping for the TWTA's nonlinear characteristics $N(\cdot)$ derived from Saleh's rational polynomials. Can the same be said for the memoryless nonlinear amplifier model of (44) when $N(\cdot)$ is based on scatter plot derived HPA nonlinear characteristics? The answer is yes. In [35] a TWTA's nonlinear characteristics $N(\cdot)$ are given by (44) which in turn is represented by a *nonlinear transformation with memory* $H(\cdot)$. The transformation $T(\cdot)$ in (46) is also modified by replacing $N(\cdot)$ with $H(\cdot)$. Relying on [36], the authors prove that there exists an appropriate α which ensures $T(\cdot)$ is a contraction mapping. The proof does not require that $g(\cdot)$ and $p(\cdot)$ be in a specific form such as Saleh's model – it only requires that the amplifier's nonlinear characteristics be given by (44). An α should still exist which ensures $T(\cdot)$ is a contraction mapping when the memory length of $H(\cdot)$ becomes zero. Therefore, basing a zero memory length $H(\cdot)$ on scatter plot derived HPA nonlinear characteristics will not prevent $T(\cdot)$ from being a contraction mapping for some value of α.

The FPPD has four parameters: convergence factor α, desired linear gain g_0, number of iterations i, and the HPA's nonlinear characteristics $N(\cdot)$. The HPA's nonlinear characteristics were discussed earlier in this chapter. The desired linear gain is found by examining Fig. 56. The slope of a line connecting the origin to the AM/AM scatter plot's saturation point $(0.3647, 0.2705)$ is 0.742 so the desired linear gain is set to $g_0 = 0.75$. The convergence factor α is less than one so an initial value of 0.8 was chosen in accordance with the simulations presented in [34].

The first series of compensation tests were run with $\alpha = 0.8$, $g_0 = 0.75$, and the number of iterations set to $i = 10, 20, \text{and } 30$. Perfect compensation would result in an HPA output signal equal to 0.75 times the input signal. PSD comparisons between a scaled version (0.75) of the actual input signal and the three compensated output signals are shown in Figs. 59-61. A comparison between any of these plots and Fig. 55 shows a significant reduction in sideband regrowth. This of course begs the question – did the FPPD actually reduce sideband regrowth or was it the result of essentially scaling the input signal's magnitude by 75%. In other words, the original unity gain HPA now has a gain equal to 0.75 because of the choice of $g_0 = 0.75$. This is equivalent to reducing the input signal's amplitude to 75% of its original level. Therefore, comparing a scaled version (0.75) of the actual input signal to an uncompensated output signal generated using this scaled input signal should test the FPPD's effectiveness. A PSD comparison between these two signals is shown in Fig. 62. Except for a slight decrease in the signals' maximum PSD magnitude, the plots are almost identical, i.e., scaling the input signal's magnitude by 75% produced only a very slight reduction in sideband regrowth. A PSD comparison limited to a 4 MHz bandwidth around the carrier frequency between the compensated output signal ($i = 20$) and the uncompensated output signal of Fig. 62 is shown in Fig. 63. The FPPD reduced sideband regrowth by more than 30 dB for an output signal having the same power as an uncompensated output signal.

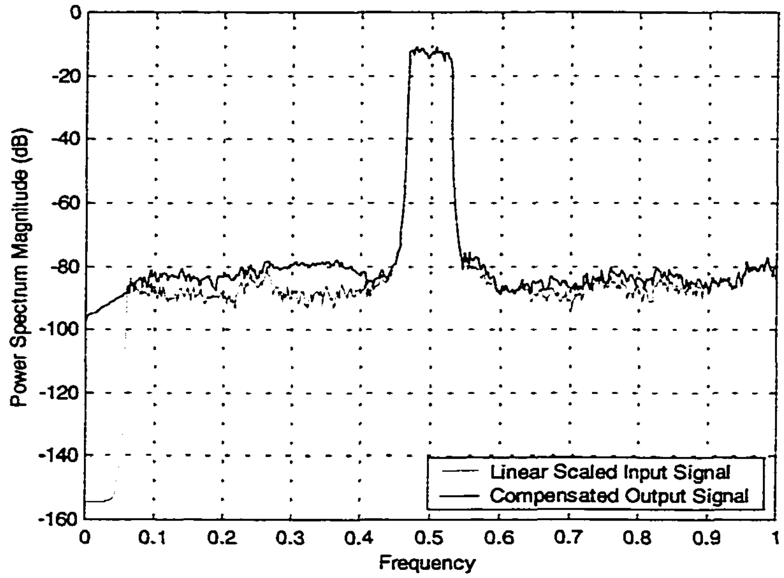

Fig. 59. PSD comparison between scaled input signal (light) and compensated output signal (dark) showing reduced sideband regrowth for $i = 10$. First data set (modified).

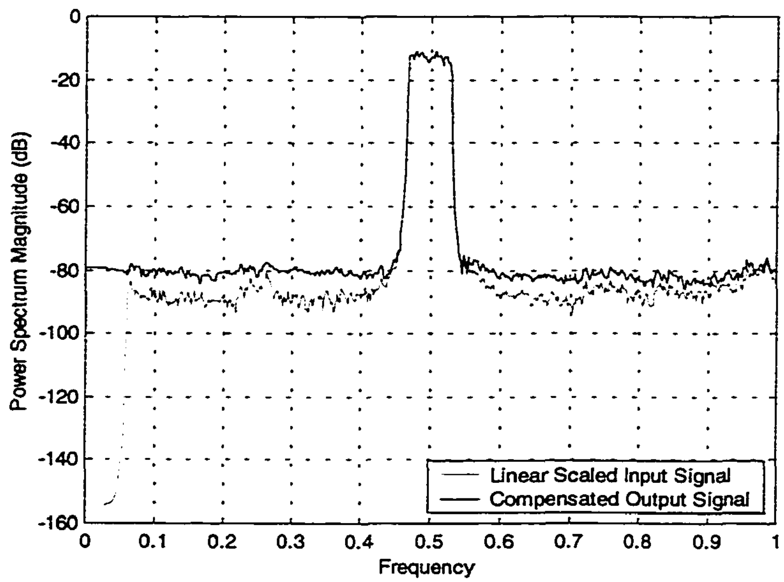

Fig. 60. PSD comparison between scaled input signal (light) and compensated output signal (dark) showing reduced sideband regrowth for $i = 20$. First data set (modified).

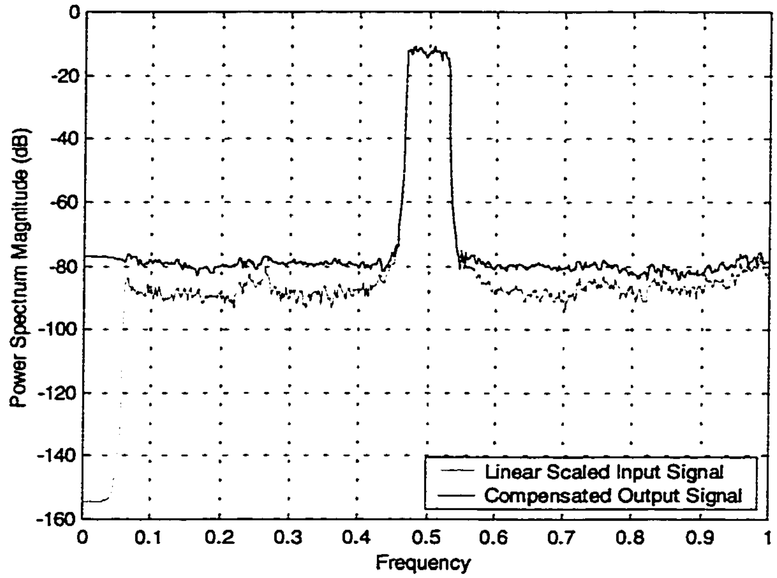

Fig. 61. PSD comparison between scaled input signal (light) and compensated output signal (dark) showing reduced sideband regrowth for $i=30$. First data set (modified).

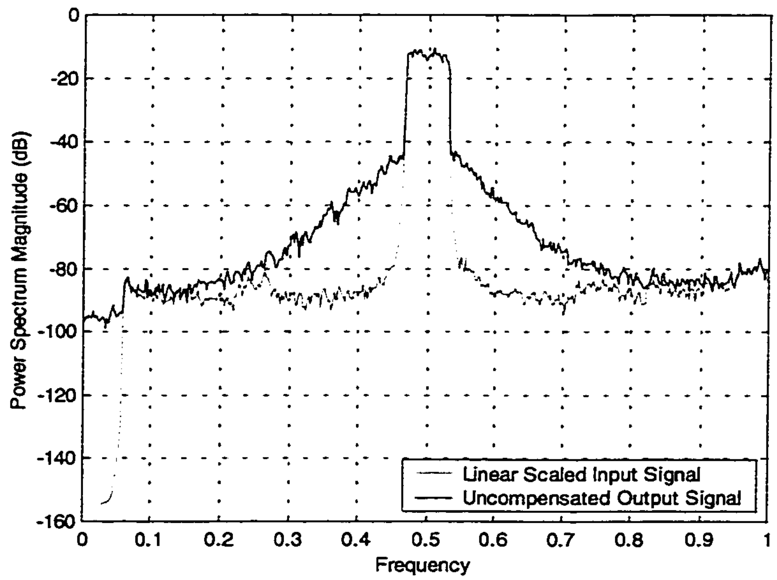

Fig. 62. PSD comparison between scaled input signal (light) and uncompensated output signal (dark) showing sideband regrowth. First data set (modified).

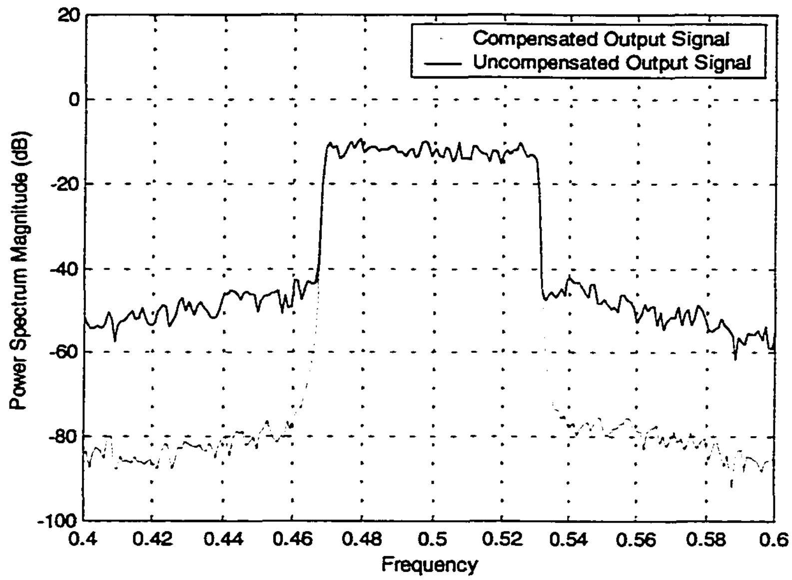

Fig. 63. PSD comparison between compensated output signal (light) and uncompensated output signal (dark) limited to a 4 MHz bandwidth around the carrier frequency showing reduced sideband regrowth. First data set (modified).

The scaled version (0.75) of the actual input signal was subtracted from the three compensated output signals to form a set of error signals. The error signals' power, referenced to 50Ω, are listed in Table 12.

Number of Iterations, i	Error Signal's Power, pW
10	45.3
20	67.1
30	102.2

Table 12. Error signals' power for the three compensated output signals shown in Figs. 59-61 generated using $\alpha = 0.8$, $g_0 = 0.75$, and the number of iterations set to $i = 10$, 20, and 30.

Note that the reduction in sideband regrowth, especially within the bandwidth of interest, was not greatly influenced by the choice of i even though error signal power did increase as i increased due to the activity outside the bandwidth of interest. Setting the number of iterations to $i=10$ in other compensation tests did not provide adequate compensation. Hence, $i=20$ was chosen as the standard number of iterations used in the remainder of the compensation tests in this chapter and the IS-2000 forward link simulations in the next chapter.

The next series of compensation tests were performed with $g_0=0.75$, $i=20$, and the convergence factor α running between 0.1 and 0.99. As before, perfect compensation would result in an HPA output signal equal to 0.75 times the input signal. The scaled version (0.75) of the actual input signal was subtracted from the various compensated output signals to form a set of error signals. The error signals' power, referenced to 50Ω, are listed in Table 13.

Convergence Factor, α	**Error Signal's Power, nW**
0.1	153.17
0.2	2.34
0.3	0.129
0.4	0.051
0.5	0.040
0.6	0.043
0.7	0.054
0.8	0.067
0.9	0.079
0.99	0.088

Table 13. Error signals' power for the various compensated output signals generated using $g_0=0.75$, $i=20$, and a convergence factor α between 0.1 and 0.99.

The lowest error signal power occurred for $\alpha=0.5$. A PSD comparison between a scaled version (0.75) of the actual input signal and the compensated output signal generated using $\alpha=0.5$ is shown in Fig. 64. A comparison between this plot and Figs. 59-61 shows that reduction in sideband regrowth within the bandwidth of interest is not greatly influenced by the choice of α as long as a "reasonable" value is chosen. Reducing the error signal power outside the bandwidth of interest appears to be the major effect of choosing the optimum value of α.

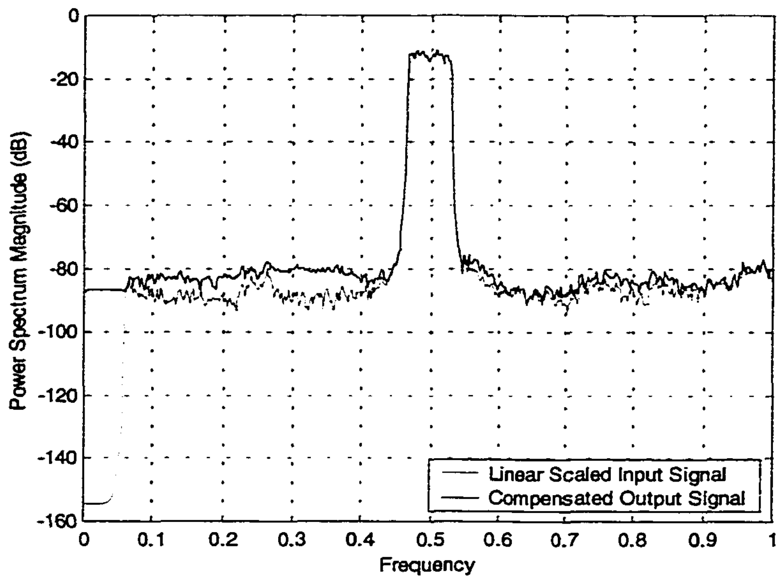

Fig. 64. PSD comparison between scaled input signal (light) and compensated output signal (dark) showing reduced sideband regrowth for $\alpha = 0.5$. First data set (modified).

The final series of compensation tests were run with $i = 20$, $\alpha = 0.8$, and the desired linear gain set to $g_0 = 0.6, 0.8, 0.85, \text{and } 0.9$. Recall that 0.75 (actually 0.742) is the maximum linear gain available from the HPA having the AM/AM scatter plot shown in Fig. 56 if the input signal is restricted to a peak amplitude of 0.3647 volts. Setting the desired linear gain to a value greater than 0.75 should result in a distorted output signal and possible divergence of (47). Scaled versions $(0.6, 0.8, \text{and } 0.85)$ of the actual input signal were subtracted from the three compensated output signals generated using $g_0 = 0.6, 0.8, \text{and } 0.85$, respectively, to form a set of error signals. Note that a compensated output signal was not generated for $g_0 = 0.9$ because (47) diverged. The error signals' power, referenced to 50Ω, are listed in Table 14.

Desired Linear Gain, g_0	Error Signal's Power, nW
0.6	0.0004
0.8	0.7153
0.85	1.3815

Table 14. Error signals' power for the various compensated output signals generated using, $i = 20$, $\alpha = 0.8$, and $g_0 = 0.6$, 0.8, and 0.85.

The lowest error signal power occurred for $g_0 = 0.6$ – a value well below the maximum linear gain of 0.75. PSD comparisons between scaled versions $(0.6, 0.8, \text{and } 0.85)$ of the actual input signal and the three compensated output signals generated using $g_0 = 0.6, 0.8, \text{and } 0.85$, respectively, are shown in Figs. 65-67. A comparison between Figs. 64 and 65 shows that reducing the desired linear gain from 0.75 to 0.6 results in almost perfect compensation. The downside is the approximately 2 dB loss in gain. Setting the desired linear gain to a value greater than 0.75 did result in a distorted output signal as shown in Figs. 66 and 67 and divergence of (47) for $g_0 = 0.9$.

These compensation tests show the interaction among the FPPD parameters: convergence factor, desired linear gain, and number of iterations. Further research could be conducted concerning optimum values for, and interactions among, these parameters. The optimum values for these parameters depend of the input signal's statistics and the HPA's nonlinear characteristics. The interaction among the FPPD parameters will only increase the difficulty of finding these optimum values if they truly exist.

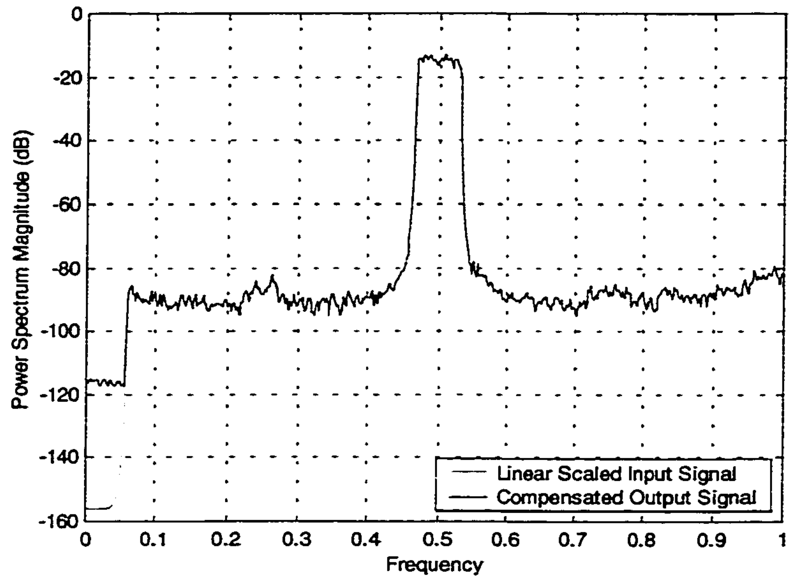

Fig. 65. PSD comparison between scaled input signal (light) and compensated output signal (dark) showing reduced sideband regrowth for $g_0 = 0.6$. First data set (modified).

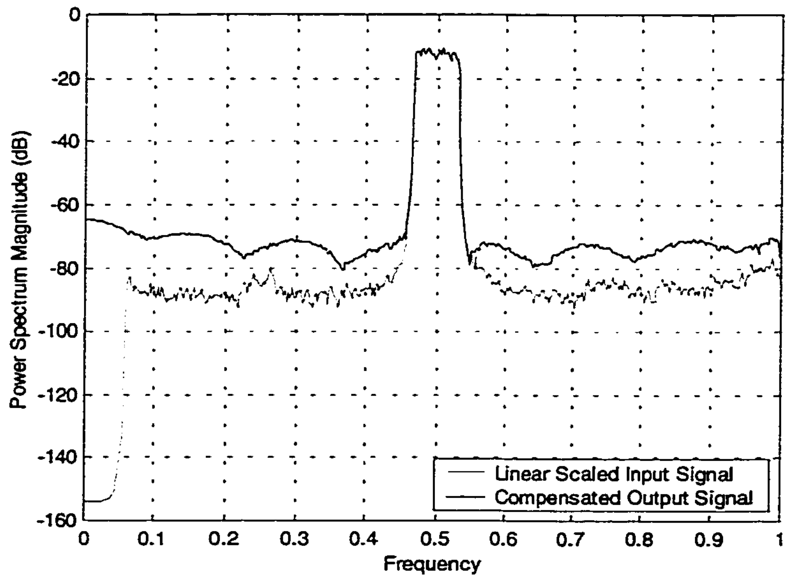

Fig. 66. PSD comparison between scaled input signal (light) and compensated output signal (dark) showing sideband regrowth for $g_0 = 0.8$. First data set (modified).

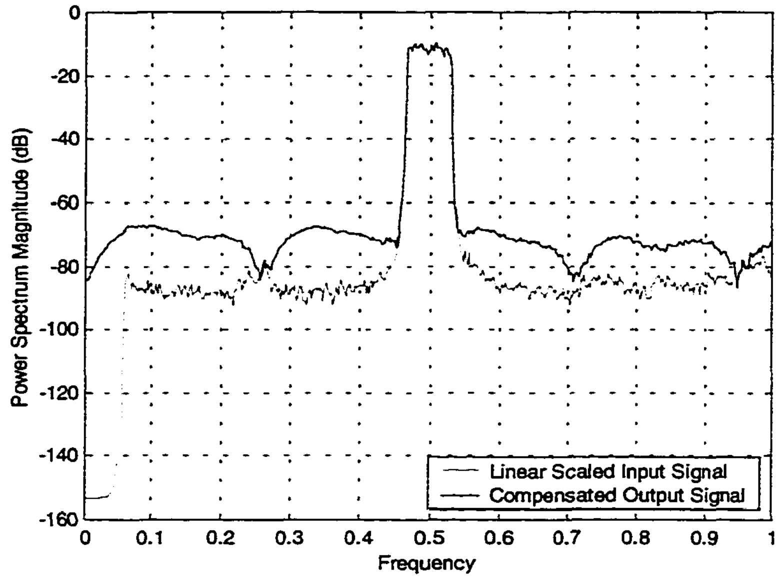

Fig. 67. PSD comparison between scaled input signal (light) and compensated output signal (dark) showing sideband regrowth for $g_0 = 0.85$. First data set (modified).

The performance of an FPPD incorporating an envelope-phase model using scatter plot derived HPA nonlinear characteristics is evaluated using an IS-2000 forward link simulator in the next chapter. The HPA's actual nonlinear characteristics $N(\cdot)$, the fourth FPPD parameter, were used in the simulations presented in this chapter. In the next chapter the effect of using suboptimal nonlinear characteristics is investigated. Suboptimal nonlinear characteristics could arise, for example, if the HPA's AM/AM conversion and AM/PM conversion were derived from network analyzer measurements instead of using the scatter plot technique.

CHAPTER 4 IS-2000 FORWARD LINK SIMULATOR

An FPPD and HPA do not operate in isolation – they are just two of the components in an overall communications system. The last chapter examined the performance of an isolated FPPD and HPA. This chapter examines the performance of an IS-2000 forward link simulator incorporating an FPPD and HPA. The FPPD effectively reduces the HPA's gain to decrease IMD and sideband regrowth. The simulations presented demonstrate how link performance is affected by this effective reduction in HPA gain. This chapter begins by discussing the IS-2000 forward link simulator and its operating parameters. The link performance using a *perfectly* linear HPA and an uncompensated HPA are then examined to provide benchmarks by which to judge the FPPD's effectiveness. The chapter concludes by examining the link performance using an HPA compensated by an FPPD.

4.1 SIMULATOR CHARACTERISTICS AND OPERATION

The IS-2000 forward link simulator is an advanced chip level implementation of the forward link of Radio Configuration 3 [37]. Simulations performed at the chip level instead of the symbol level more accurately model link performance with the tradeoff being greatly increased processing time. The simulator features convolutional coding for error correction, incorporates a power control subchannel, and utilizes Jake's fading model to simulate the transmission channel. The block diagram in Fig. 68 shows the base station portion of the simulator without the FPPD and HPA. The mobile subscriber unit

(MSU) receiver (not shown) uses coherent detection. The received signal consists of two components. The first component is the transmitted signal consisting of the pilot channel and traffic channel. The transmitted signal experiences fading in the transmission channel before being received. The second component is a Gaussian random variable that models the other in-cell traffic channels, out-of-cell (non-serving) base stations, and noise. The pilot channel and traffic channel detection is thus hindered by the interference provided by the zero-mean Gaussian random variable.

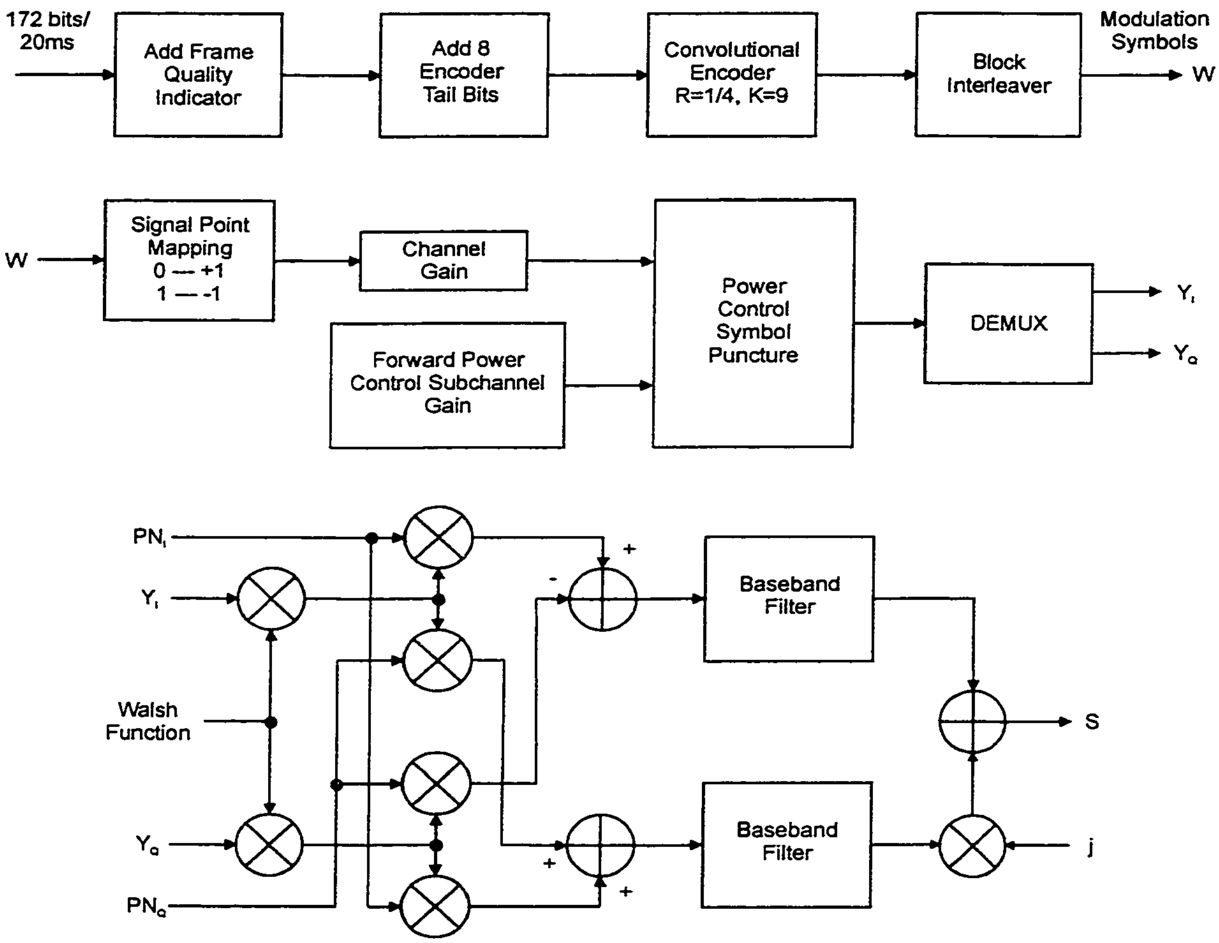

Fig. 68. IS-2000 forward link simulator base station.

Forward link performance is determined by and measured in terms of the following parameters. The PSD of the other in-cell traffic channels measured at the receiver is denoted by I_{or} and is normalized to one. The PSD of the interference measured at the receiver from the out-of-cell base stations and noise is given by I_{oc}. The ratio I_{or}/I_{oc}, known as the geometry, determines the strength of the out-of-cell interference (including noise) relative to the interference from the other in-cell traffic channels. The pilot channel or traffic channel power relative to I_{or} is given by E_c/I_{or}. Note that all power levels are referenced to 1Ω in this chapter.

Forward link performance is measured by the average traffic channel E_c/I_{or} required to achieve a given frame error rate (FER), usually 1%, at a specified MSU speed. The traffic channel E_c/I_{or} is adjusted on a frame-by-frame basis using a power control scheme to achieve the desired FER. The forward link simulator utilizes both an inner (fast) loop and an outer (slow) loop power control scheme. The inner loop updates every 1.25 ms while the outer loop updates once per frame, i.e., every 20 ms. There are sixteen power control groups within each frame. Table 15 lists the simulation parameters used for all forward link simulations presented in this chapter. A detailed description of the IS-2000 forward link simulator is found in [38].

Most comparable forward link simulators, such as those used to measure the effectiveness of different error correction codes or transmit antenna diversity methods for example, do not explicitly incorporate an HPA model. In other words, the lack of an HPA model is equivalent to using a perfectly linear HPA having unity gain, zero degrees of phase shift, and no saturation level. This guarantees that link performance is not hindered by any HPA nonlinear behavior. This simulator includes the envelope-phase model of an HPA (44) to more accurately predict link performance as well as to have an HPA for the FPPD to linearize. The block diagram in Fig. 69 shows the placement of the FPPD and HPA within the base station portion of the simulator.

Carrier frequency	2 GHz
Bit rate	9600 bps
Chip rate	1.2288 Mcps
Frame length	20 ms
Interleaver depth	20 ms (block)
Walsh code length	64
Error control coding	R = 1/4, K = 9
Power control puncturing	Included
Geometry	$I_{or}/I_{oc} = 6$ dB
Pilot channel E_c/I_{or}	–7 dB
Traffic channel E_c/I_{or}	–3/–40 dB (maximum/minimum)
Inner-loop power control rate	800 Hz
Power control command error rate	5%
Inner-loop power control step	+/– 0.5 dB
Outer-loop power control step	Frame error based at 50 Hz
Target frame error rate	1%
Channel estimation window	0.25 ms
Multipath channel	1-path Rayleigh fading

Table 15. IS-2000 forward link simulation parameters.

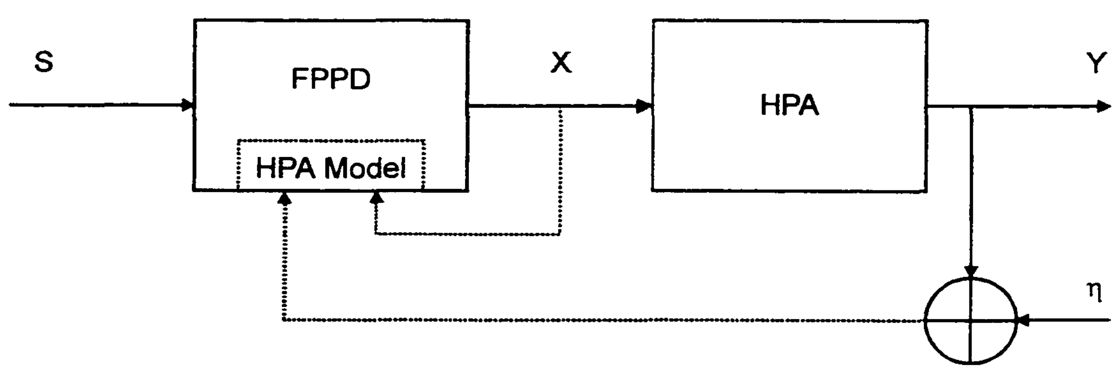

Fig. 69. IS-2000 forward link simulator FPPD and HPA.

Observe the presence of two envelope-phase models in Fig. 69. The first models the HPA's nonlinear characteristics. The FPPD's fourth parameter – the HPA's nonlinear characteristics $N(\cdot)$ – is characterized by the second model. Normally, the second model's parameters are determined by measuring the HPA's input and output signals. In essence, an envelope-phase model characterizes the nonlinear behavior of an HPA that is modeled using an envelope-phase model. This method is not as circular as it appears since *measurement* noise is added to the HPA's output signal from which the FPPD derives the HPA's nonlinear characteristics.

4.2 SIMULATION RESULTS FOR LINEAR HPA

The forward link performances presented in this chapter are measured by the average traffic channel E_c/I_{or} required to achieve a 1% FER for a total of one hundred errors. This means that on average each simulation takes ten thousand frames to complete. As mentioned previously, most comparable forward link simulators effectively use a perfectly linear HPA having unity gain, zero degrees of phase shift, and no saturation level. The forward link performance using a perfectly linear HPA as described above is shown in Fig. 70. The link performance was measured by performing ten simulations at each of seven different MSU speeds (in kilometers per hour): 1, 3, 5, 10, 30, 50, and 100. The average value of the link performance at each speed is indicated by the square and the minimum and maximum values are indicated by the dots on the error bars' ends. These results provide the best performance that can be expected using the simulation parameters shown in Table 15.

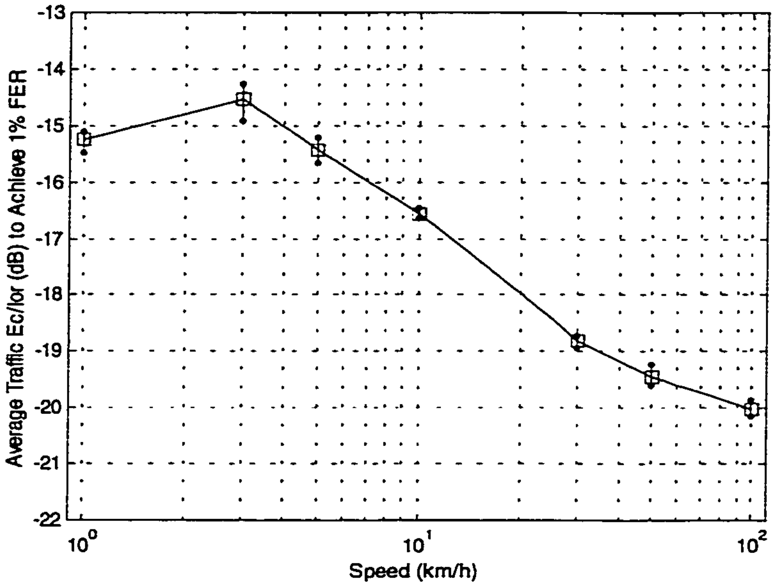

Fig. 70. Forward link performance using perfectly linear HPA.

The results shown in Fig. 70 were obtained by performing ten simulations at each indicated MSU speed. The forward link performance at any particular speed does not vary much from simulation to simulation with the possible exception of 3 km/h. The ten simulations performed at 30 km/h, for example, have the statistics for the average traffic channel E_c/I_{or} required to achieve a 1% FER shown in Table 16.

Minimum E_c/I_{or}	−18.9452 dB
Mean E_c/I_{or}	−18.8160 dB
Maximum E_c/I_{or}	−18.7197 dB
Standard deviation	0.0702 dB

Table 16. Forward link performance statistics for ten simulations performed at 30 km/h using perfectly linear HPA.

The link performance only varies by about 0.1 dB from the mean value of −18.8160 dB for any individual simulation at an MSU speed of 30 km/h. The next step is to introduce an uncompensated HPA into the simulator to determine how a *real* HPA's nonlinear behavior affects link performance.

4.3 SIMULATION RESULTS FOR UNCOMPENSATED HPA

The HPA's nonlinear characteristics were based on its input signal's statistics. Recall that the HPA's input signal is comprised of the pilot channel and traffic channel. The input signal's statistics of interest are the mean complex envelope magnitude and the peak complex envelope magnitude determined on a frame-by-frame basis. Table 17 lists the mean complex envelope magnitude, mean peak complex envelope magnitude, and the maximum peak complex envelope magnitude for a forward link simulation of over ten thousand frames. The mean peak-to-average power ratio is 8.6 dB.

Mean magnitude	0.4419 volts
Mean peak magnitude	1.1974 volts
Maximum peak magnitude	2.3156 volts

Table 17. HPA's input signal statistics.

The HPA's nonlinear characteristics need to provide a measurable increase in the average traffic channel E_c/I_{or} required to achieve a 1% FER in addition to significant sideband regrowth. The AM/AM conversion and AM/PM conversion shown in Figs. 71 and 72, respectively, were chosen based on these considerations and the data in Table 17. These nonlinear characteristics represent those of a typical solid-state HPA. The functions $g(\cdot)$ and $p(\cdot)$ in (44) are represented by a 13th order and an 8th order polynomial approximation, respectively. Note that the AM/AM conversion has approximately unity gain in its linear region.

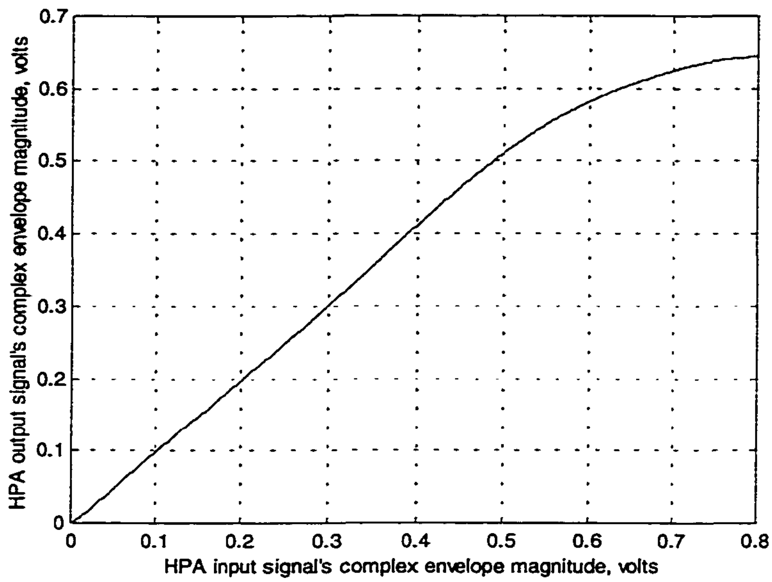

Fig. 71. IS-2000 forward link simulator HPA's AM/AM conversion.

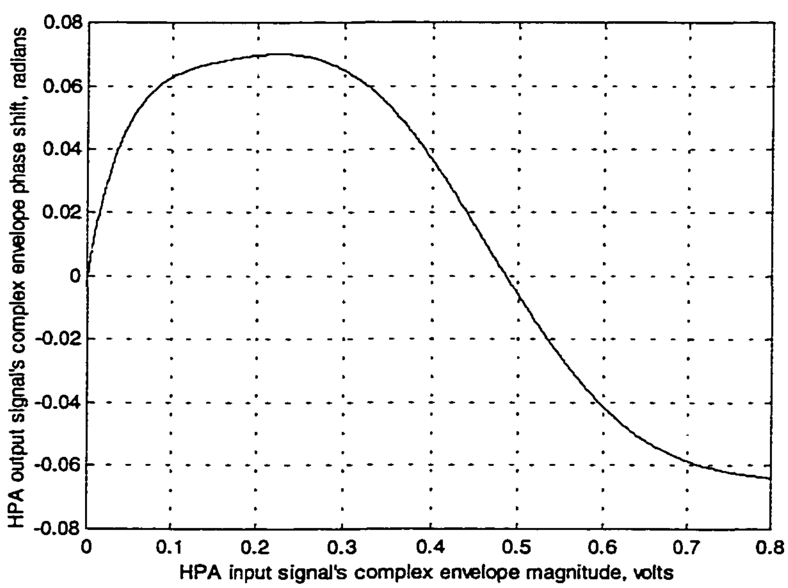

Fig. 72. IS-2000 forward link simulator HPA's AM/PM conversion.

The forward link performance using an uncompensated HPA as described above is shown in Fig. 73. The link performance was measured by performing ten simulations at each of the seven different MSU speeds used previously. The link performance using the perfectly linear HPA is also repeated in Fig. 73. Note that the link performance has decreased by approximately 1.5 dB between 30 and 100 km/h. Below 30 km/h the link performance is much worse and at 1, 3, and 5 km/h the target FER of 1% could not be achieved. These results provide the best performance that can be expected using the simulation parameters shown in Table 15 with an uncompensated HPA and are the benchmark by which the FPPD performance is measured.

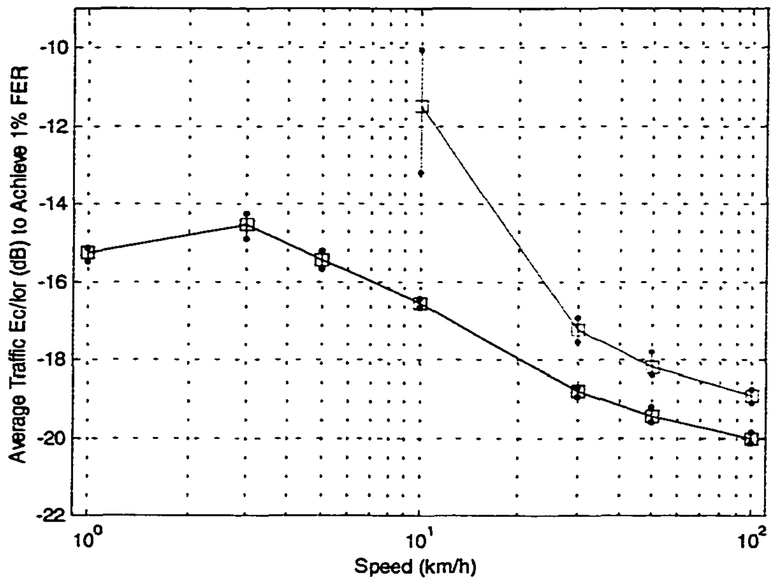

Fig. 73. Comparison between forward link performance using uncompensated HPA (upper trace) and perfectly linear HPA (bottom trace).

The ten simulations performed at 30 km/h have the statistics for the average traffic channel E_c/I_{or} required to achieve a 1% FER shown in Table 18.

Minimum E_c/I_{or}	−17.5402 dB
Mean E_c/I_{or}	−17.2237 dB
Maximum E_c/I_{or}	−16.9178 dB
Standard deviation	0.1926 dB

Table 18. Forward link performance statistics for ten simulations performed at 30 km/h using uncompensated HPA.

The link performance only varies by about 0.3 dB from the mean value of −17.2237 dB for any individual simulation at 30 km/h. The remaining forward link simulations presented in this chapter are performed at an MSU speed of 30 km/h.

Substituting an uncompensated HPA for a perfectly linear HPA results in a 1.5 dB decrease in link performance at 30 km/h – it also affects sideband regrowth. Four frames of the HPA's input signal, each having a different traffic channel E_c/I_{or}, were collected to gauge this effect. The four frames of input signal have a traffic channel E_c/I_{or} (in dB) of between: −40 and −25, −18 and −16, −11 and −9, and −7 and −3. PSD comparisons between the HPA's input signal and its uncompensated output signal for each of these four input signals are shown in Figs. 74-77. The sideband regrowth is significant, especially at the higher power levels.

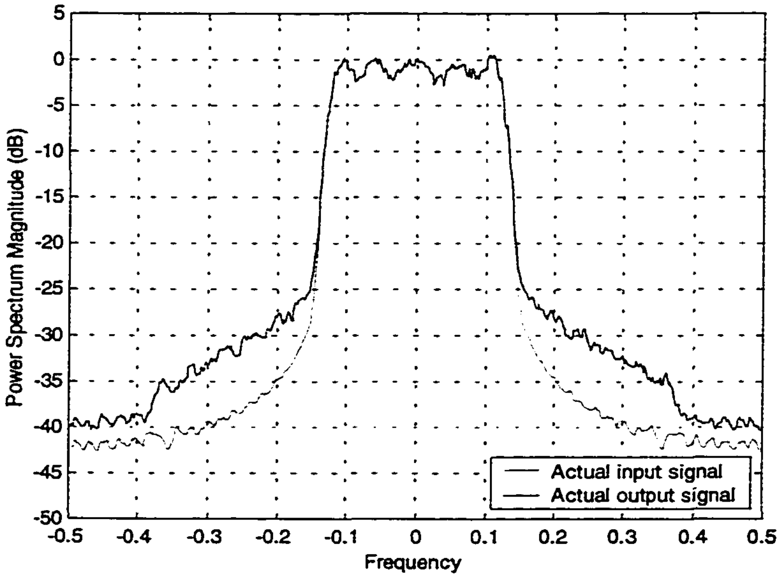

Fig. 74. PSD comparison between input signal (light) and uncompensated output signal (dark) showing sideband regrowth for traffic channel E_c/I_{or} between −40 and −25 dB.

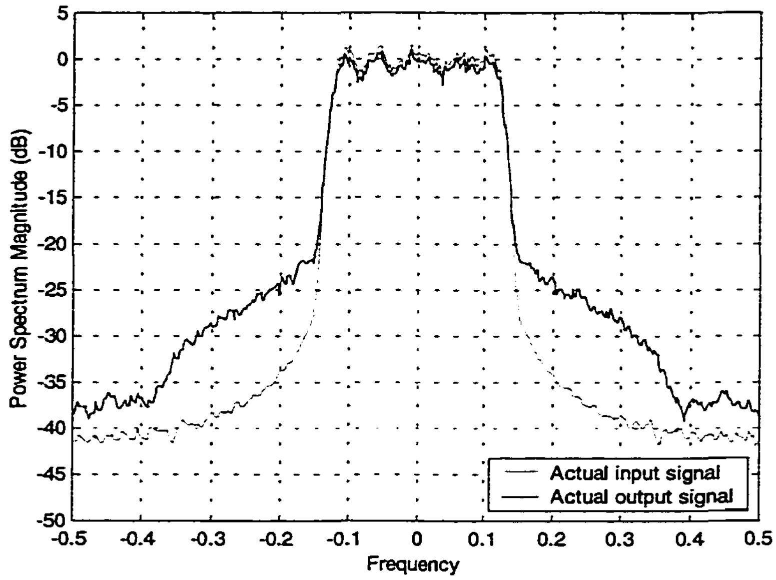

Fig. 75. PSD comparison between input signal (light) and uncompensated output signal (dark) showing sideband regrowth for traffic channel E_c/I_{or} between −18 and −16 dB.

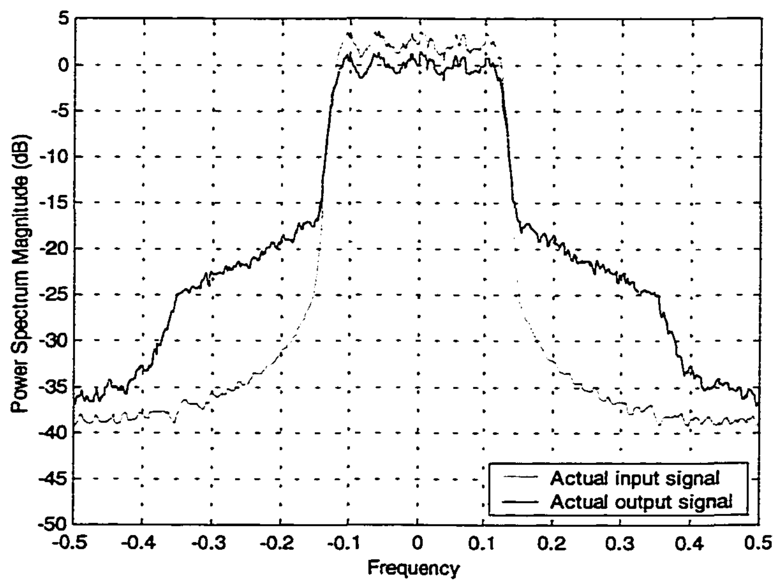

Fig. 76. PSD comparison between input signal (light) and uncompensated output signal (dark) showing sideband regrowth for traffic channel E_c/I_{or} between −11 and −9 dB.

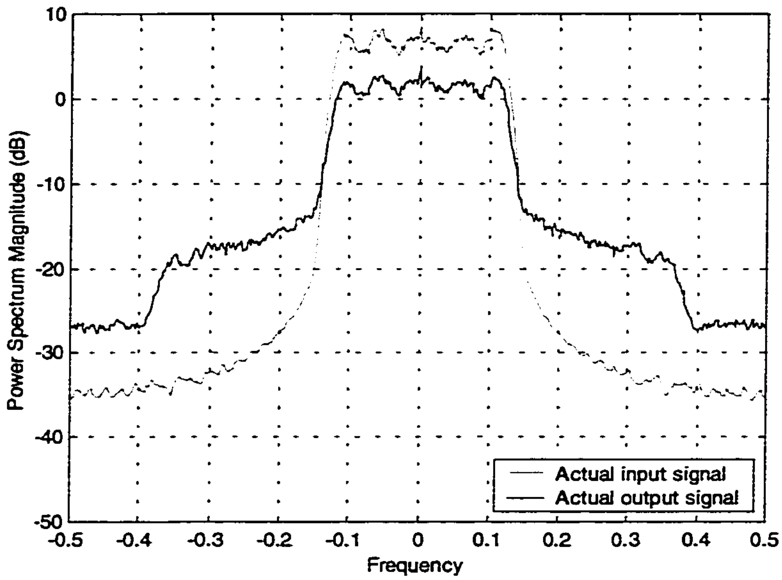

Fig. 77. PSD comparison between input signal (light) and uncompensated output signal (dark) showing sideband regrowth for traffic channel E_c/I_{or} between –7 and –3 dB.

4.4 SIMULATION RESULTS FOR COMPENSATED HPA

Replacing the IS-2000 forward link simulator's perfectly linear HPA with an uncompensated HPA results in reduced link performance and significant sideband regrowth. The next series of simulations incorporate an FPPD into the simulator as shown in Fig. 69 to combat these deleterious effects. Recall that an FPPD has four parameters: convergence factor α, desired linear gain g_0, number of iterations i, and the HPA's nonlinear characteristics $N(\cdot)$. The remainder of the simulations incorporating an FPPD are performed with $\alpha = 0.8$ and $i = 20$. The first simulation establishes the benchmark for FPPD performance by setting $N(\cdot)$ to the HPA's actual nonlinear characteristics shown in Figs. 71 and 72 since optimum performance occurs when the FPPD is provided the HPA's actual nonlinear characteristics. The desired linear gain, $g_0 = 0.8056$, is the slope of the line connecting the origin to the AM/AM conversion's saturation point, i.e., the point $(0.8, 0.6446)$.

An average traffic channel E_c/I_{or} of –17.4587 dB achieved a 1% FER using these FPPD parameters. This forward link performance is essentially the same as that of the uncompensated HPA shown in Table 18. Perfect compensation would result in an HPA output signal equal to 0.8056 times the input signal. PSD comparisons between scaled versions (0.8056) of the four input signals used to produce the results shown in Figs. 74-77 and their respective compensated output signals are shown in Figs. 78-81. Note that Figs. 78-81 cannot be directly compared to Figs. 74-77 since both the input and output signals in the corresponding plots have different power levels. Referring to Figs. 78-81, the sideband regrowth is seen to increase as the traffic channel E_c/I_{or} increases. There appears to be little, if any, reduction in sideband regrowth at the highest traffic channel E_c/I_{or}. This can be explained by examining the compensated HPA's nonlinear characteristics, i.e., the overall nonlinear characteristics of the combined FPPD and HPA.

The compensated HPA's AM/AM scatter plot and AM/PM scatter plot are found using a slightly modified version of the method previously described. First, the input and output signals are not converted to analytic signals because they are already in that form. Second, the alignment of the input signal's complex envelope magnitude and phase with the output signal's complex envelope magnitude and phase is unnecessary because the input and output signals are sampled synchronously. The remaining steps are unchanged from those previously described.

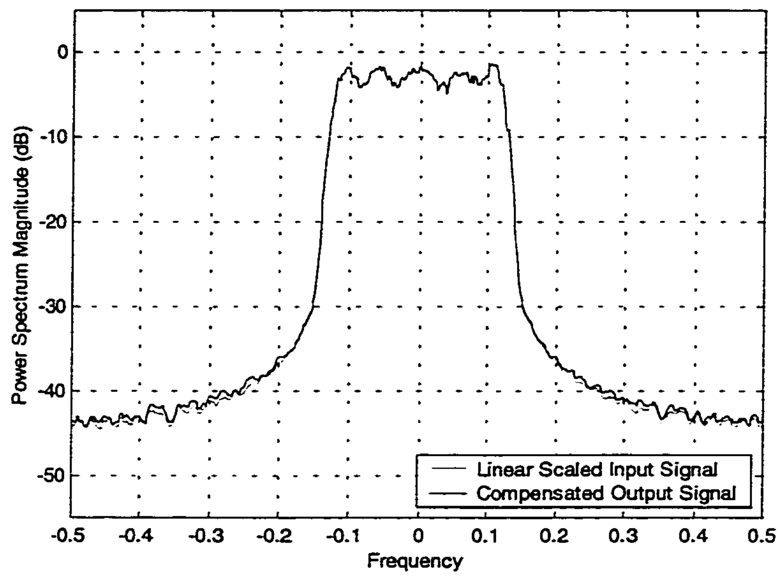

Fig. 78. PSD comparison between scaled input signal (light) and compensated output signal (dark) showing reduced sideband regrowth for traffic channel E_c/I_{or} between –40 and –25 dB. Actual nonlinear characteristics.

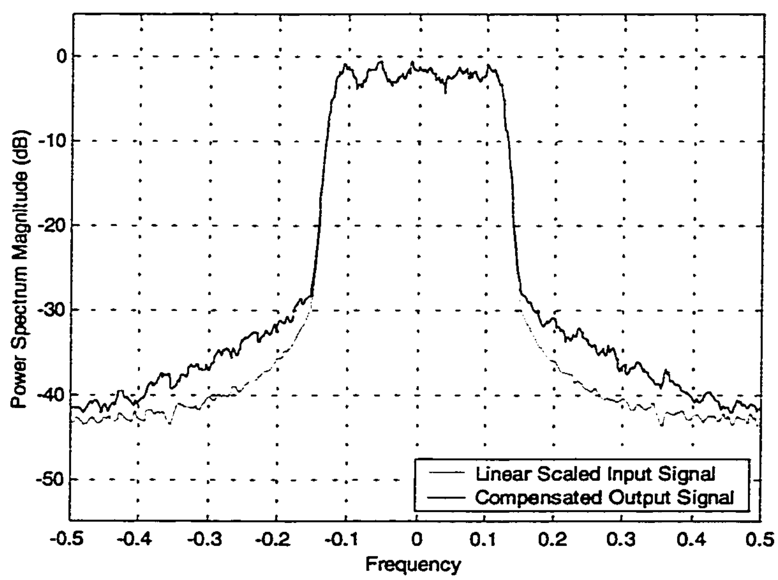

Fig. 79. PSD comparison between scaled input signal (light) and compensated output signal (dark) showing reduced sideband regrowth for traffic channel E_c/I_{or} between –18 and –16 dB. Actual nonlinear characteristics.

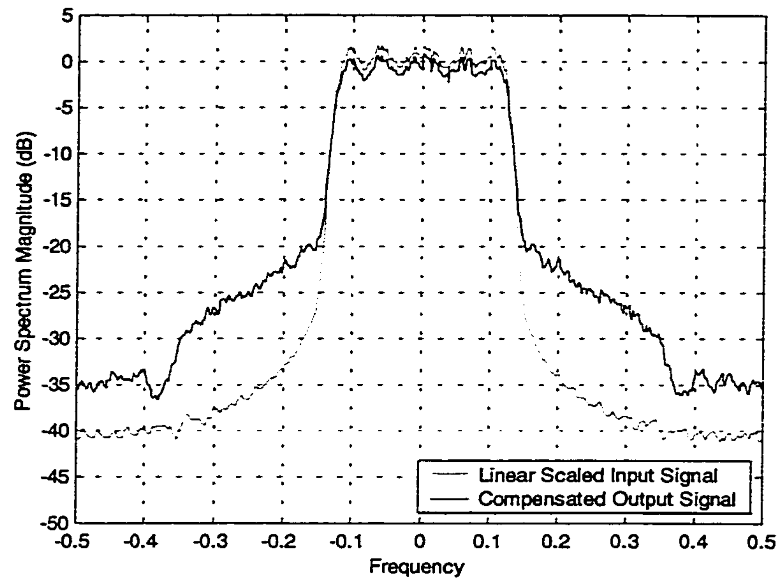

Fig. 80. PSD comparison between scaled input signal (light) and compensated output signal (dark) showing sideband regrowth for traffic channel E_c/I_{or} between –11 and –9 dB. Actual nonlinear characteristics.

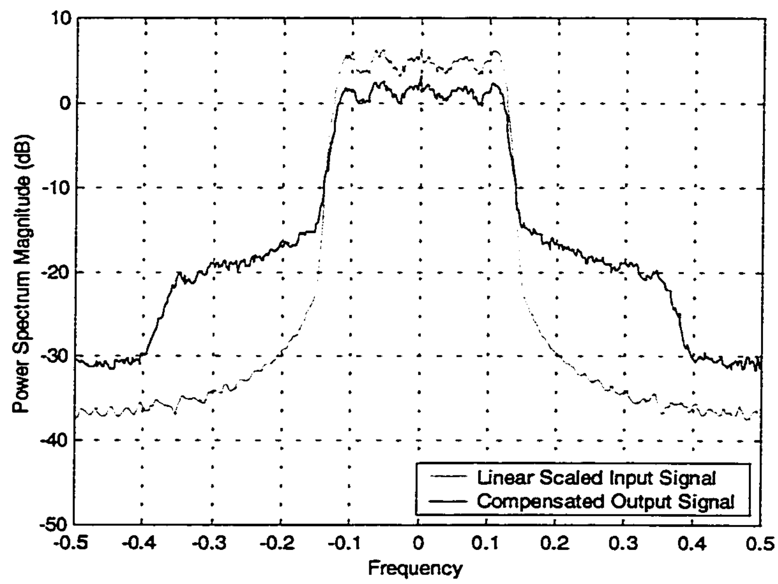

Fig. 81. PSD comparison between scaled input signal (light) and compensated output signal (dark) showing sideband regrowth for traffic channel E_c/I_{or} between –7 and –3 dB. Actual nonlinear characteristics.

The compensated HPA's AM/AM scatter plot and AM/PM scatter plot are shown in Figs. 82 and 83, respectively. These scatter plots were derived using the input signal (to the FPPD) having a traffic channel E_c/I_{or} of between –11 and –9 dB and the resulting HPA output signal. Comparing Figs. 82 and 71 show that the compensated HPA has indeed been linearized up to its saturation point. The compensated HPA also has zero degrees of phase shift as shown in Fig. 83. Note that the gain characteristic displayed in Fig. 82 is that of a clipper. This explains why there is little, if any, reduction in sideband regrowth at the highest traffic channel E_c/I_{or} since an FPPD cannot reduce sideband regrowth caused by a clipper. Even though the gain characteristic is linear up to the saturation point, the numerous input signal samples having a complex envelope magnitude greater than 0.8 volts cause significant sideband regrowth. Note that the input signal has a peak complex envelope magnitude close to 2 volts.

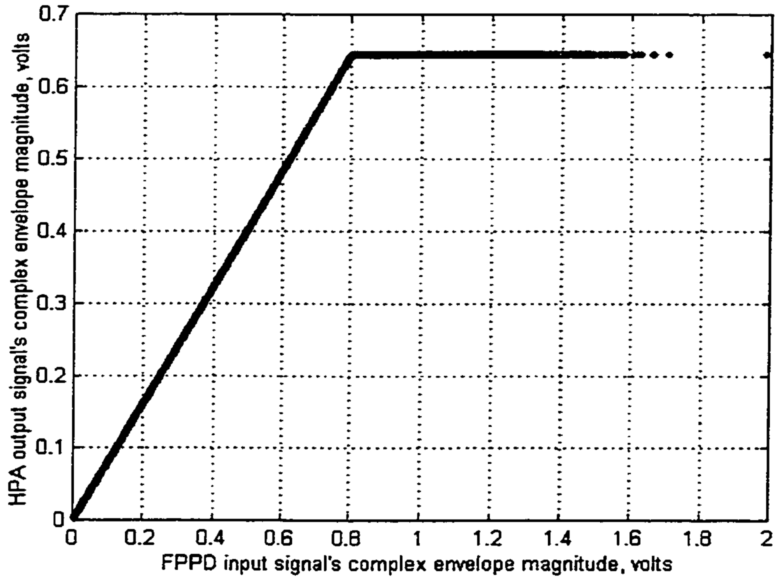

Fig. 82. Combined FPPD and HPA AM/AM scatter plot derived from FPPD input signal and HPA output signal.

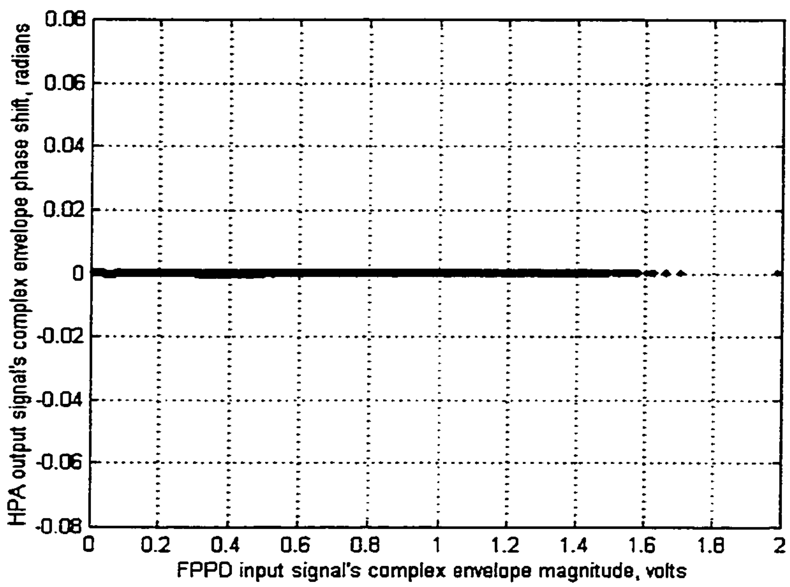

Fig. 83. Combined FPPD and HPA AM/PM scatter plot derived from FPPD input signal and HPA output signal.

Recall that in the last chapter the question arose whether reduced sideband regrowth results from the FPPD or from what is essentially scaling the input signal's magnitude. The FPPD reduced sideband regrowth significantly compared to scaling the input signal's magnitude as shown in Fig. 62 for an input signal that did not undergo clipping – or at least very little. Since the forward link simulator's nonlinear characteristics are very nonlinear considering the input signal's maximum peak complex envelope magnitude, the FPPD should be less effective at reducing sideband regrowth as compared to scaling the input signal's magnitude – especially at the highest traffic channel E_c/I_{or}. The next simulation of an uncompensated HPA having its input signal scaled by 0.8056 shows the effect on link performance and sideband regrowth of scaling the input signal.

An average traffic channel E_c/I_{or} of –17.387 dB achieved a 1% FER using the uncompensated HPA with the scaled input signal. This forward link performance is essentially the same as that of the compensated HPA. PSD comparisons between the compensated output signals and the uncompensated output signals generated using scaled versions (0.8056) of the four input signals used to produce the results shown in Figs. 74-77 are shown in Figs. 84-87. Note that only the uncompensated output signals were generated using scaled input signals. These plots show that the FPPD is indeed less effective at reducing sideband regrowth as compared to scaling the input signal's magnitude at the highest traffic channel E_c/I_{or}. Nevertheless, the FPPD does reduce sideband regrowth when the input signal has a lower traffic channel E_c/I_{or}. In Fig. 84 for example, the sideband regrowth has been reduced approximately 3 dB at 1 MHz from the carrier frequency.

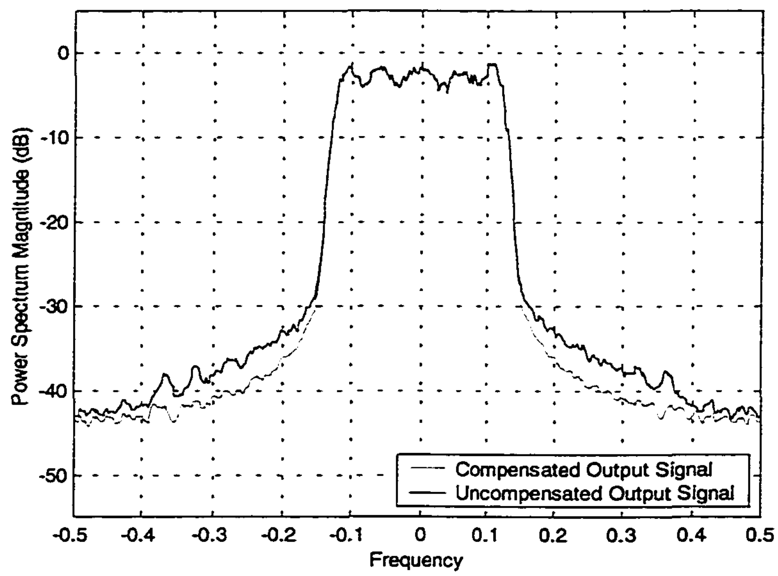

Fig. 84. PSD comparison between compensated output signal (light) and uncompensated output signal (dark) for traffic channel E_c/I_{or} between –40 and –25 dB. Actual nonlinear characteristics.

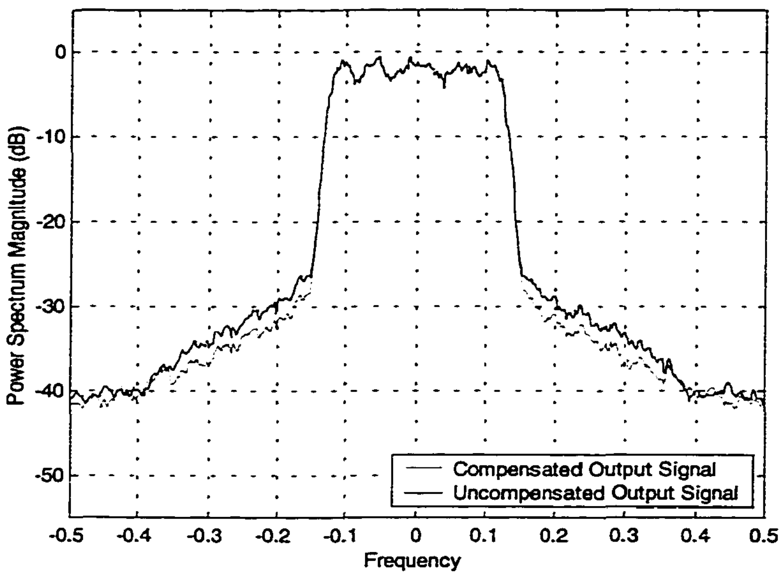

Fig. 85. PSD comparison between compensated output signal (light) and uncompensated output signal (dark) for traffic channel E_c/I_{or} between –18 and –16 dB. Actual nonlinear characteristics.

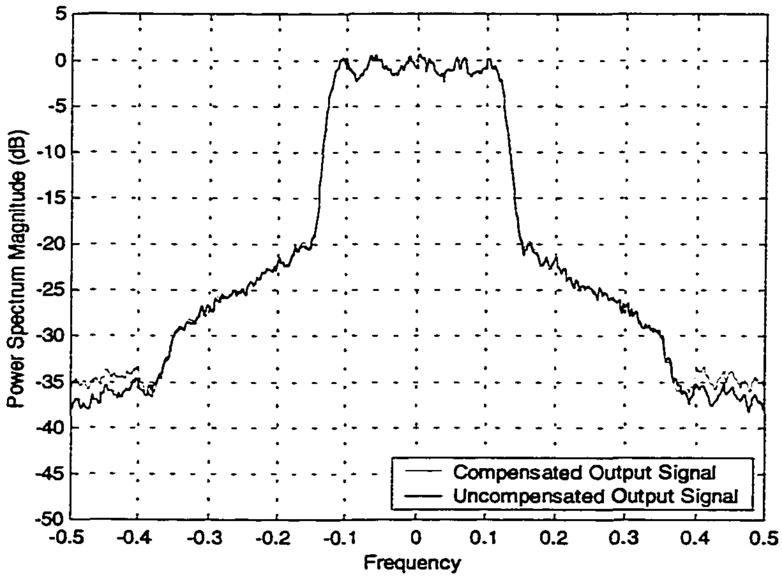

Fig. 86. PSD comparison between compensated output signal (light) and uncompensated output signal (dark) for traffic channel E_c/I_{or} between –11 and –9 dB. Actual nonlinear characteristics.

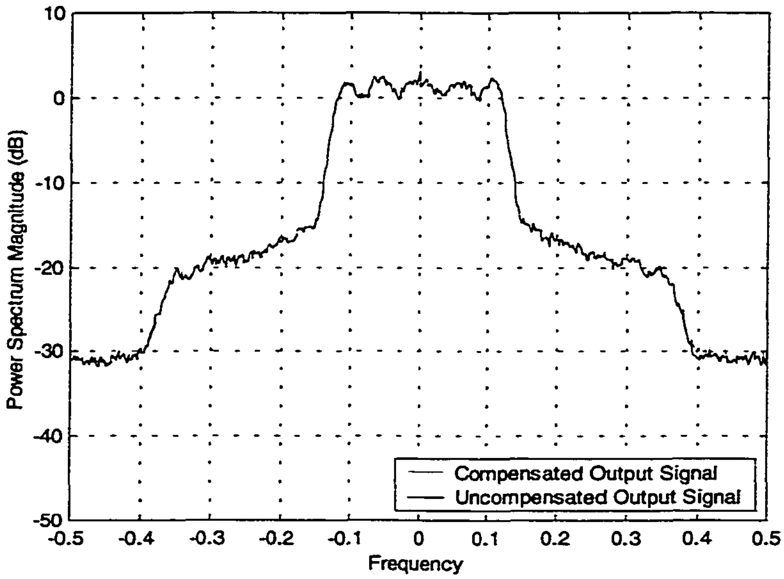

Fig. 87. PSD comparison between compensated output signal (light) and uncompensated output signal (dark) for traffic channel E_c/I_{or} between –7 and –3 dB. Actual nonlinear characteristics.

The next simulation sets $N(\cdot)$ to the HPA's nonlinear characteristics derived from measuring the HPA's input and output signals as shown in Fig. 69. Recall that *measurement* noise is added to the HPA's output signal. Otherwise, the HPA's derived nonlinear characteristics would be almost identical to its actual characteristics. The peak noise magnitude was set about 40 dB lower than the peak output signal's magnitude. A 13^{th} order and an 8^{th} order polynomial approximation was fitted to the HPA's AM/AM scatter plot and AM/PM scatter plot, respectively. The derived AM/AM conversion is almost identical to the actual AM/AM conversion shown in Fig. 71. The derived AM/PM conversion, however, differs from the actual AM/PM conversion as shown in Fig. 88. This is due to the difficulty in measuring the phase of a noisy signal at low magnitudes.

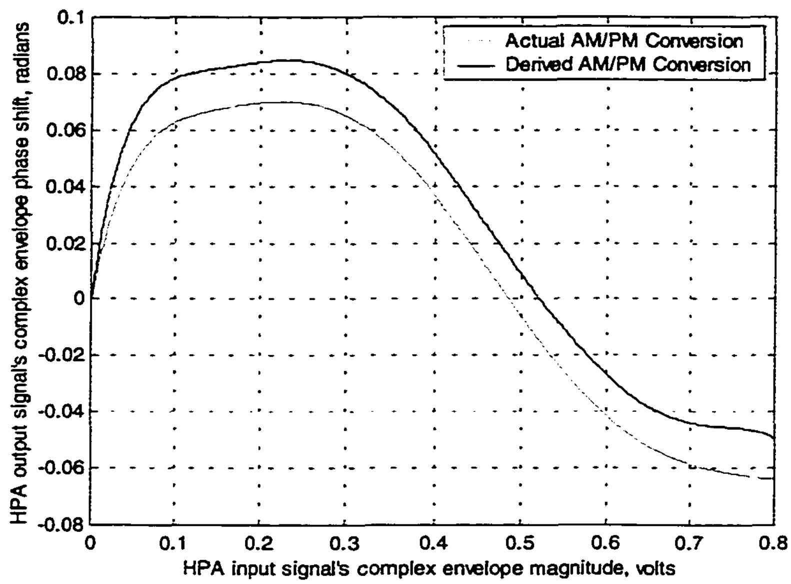

Fig. 88. Comparison between IS-2000 forward link simulator HPA's actual AM/PM conversion (light) and derived AM/PM conversion (dark).

An average traffic channel E_c/I_{or} of −17.2408 dB achieved a 1% FER using the same desired linear gain as the previous simulation. This forward link performance is essentially the same as that of the HPA compensated using the optimum FPPD. Perfect compensation would result in an HPA output signal equal to 0.8056 times the input signal. PSD comparisons between scaled versions (0.8056) of the four input signals used to produce the results shown in Figs. 74-77 and their respective compensated output signals are not shown as they are almost identical to those shown in Figs. 78-81. Hence, the FPPD using nonlinear characteristics derived from the HPA's input and output signals reduces sideband regrowth as much as the optimum FPPD.

The final simulation sets $N(\cdot)$ to the nonlinear characteristics shown in Figs. 89 and 72. Note that Fig. 72 shows the HPA's actual AM/PM conversion. The HPA's AM/AM conversion shown in Fig. 89 simulates the AM/AM conversion that would be derived with a network analyzer using a CW power sweep, i.e., the HPA's 1 dB compression point is 1 dB larger in Fig. 89 than in Fig. 71. The desired linear gain is set 0.882 to match this derived AM/AM conversion.

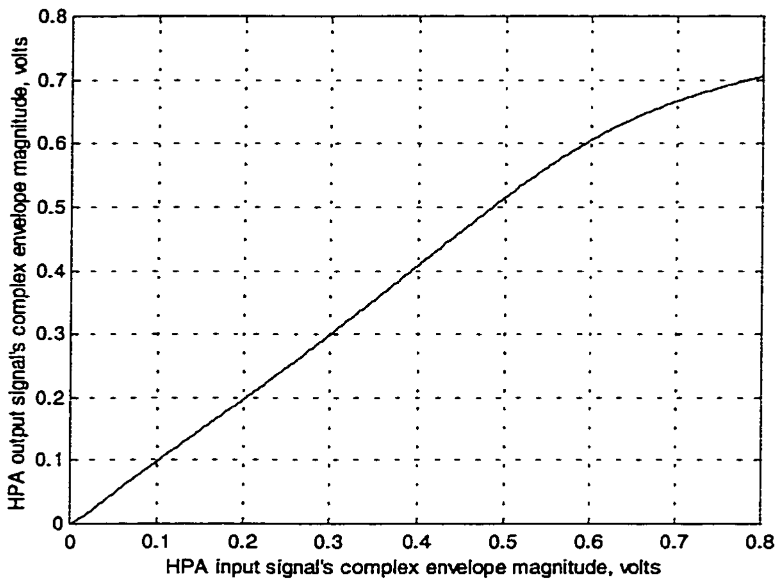

Fig. 89. IS-2000 forward link simulator HPA's AM/AM conversion derived from CW power sweep.

An average traffic channel E_c/I_{or} of –17.5568 dB achieved a 1% FER using these FPPD parameters. This forward link performance is essentially the same as that of the HPA compensated using the optimum FPPD. Perfect compensation would result in an HPA output signal equal to 0.882 times the input signal. PSD comparisons between scaled versions (0.882) of the four input signals used to produce the results shown in Figs. 74-77 and their respective compensated output signals are shown in Figs. 90-93. As was the case with the HPA compensated using the optimum FPPD, the sideband regrowth increases as the traffic channel E_c/I_{or} increases and there is little, if any, reduction in sideband regrowth at the highest traffic channel E_c/I_{or}.

Comparing Figs. 90-93 to Figs. 78-81 shows that using network analyzer derived nonlinear characteristic instead of scatter plot derived nonlinear characteristics results in greater sideband regrowth at lower traffic channel E_c/I_{or}. In Fig. 90 for example, sideband regrowth is approximately 3 dB more at 1 MHz from the carrier frequency than that shown in Fig. 78. Sideband regrowth 1 MHz from the carrier frequency is at least 4 dB more in Fig. 91 as compared to Fig. 79 and about 2 dB more in Fig. 92 as compared to Fig. 80. The sideband regrowth at the higher traffic channel E_c/I_{or} shown in Fig. 93 is essentially unchanged from that shown in Fig. 81.

The IS-2000 forward link simulator using the simulation parameters in Table 15 is a very robust system. The simulator's HPA was given very nonlinear characteristics considering the input signal's maximum peak complex envelope magnitude to adversely influence the forward link performance and cause significant sideband regrowth. These nonlinear characteristics have presented the FPPD with a worst case scenario. Even though the FPPD had little or no effect, good or bad, on the link performance it was able to reduce sideband regrowth at certain power levels. The FPPD should have a more positive influence on link performance for HPA nonlinear characteristics that are a closer match to the input signal's dynamic range, i.e., the saturation point is closer to the input signal's maximum peak complex envelope magnitude. These nonlinear characteristics would result in a greater reduction in sideband regrowth than that obtainable by simply scaling the input signal.

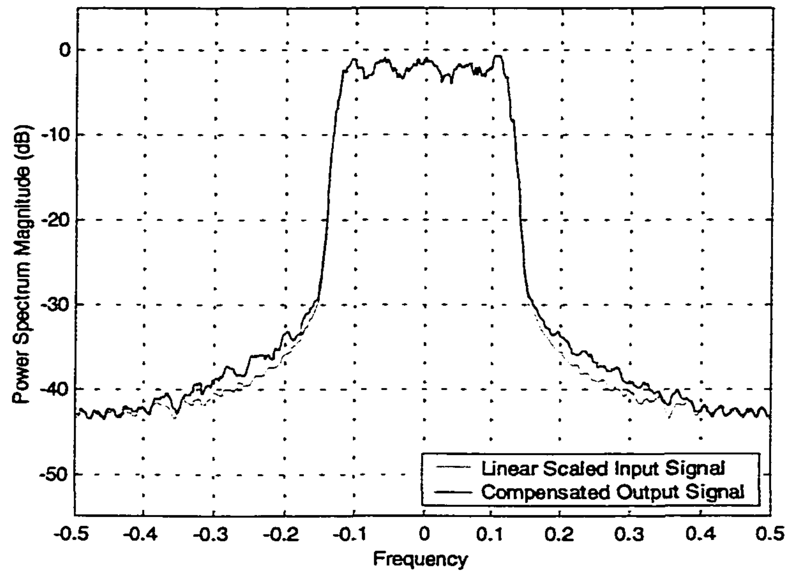

Fig. 90. PSD comparison between scaled input signal (light) and compensated output signal (dark) showing reduced sideband regrowth for traffic channel E_c/I_{or} between –40 and –25 dB. Network analyzer derived nonlinear characteristics.

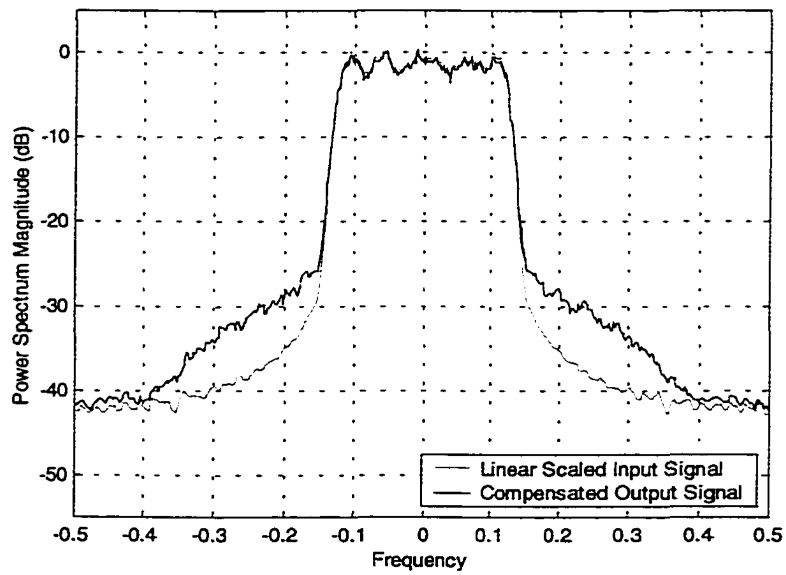

Fig. 91. PSD comparison between scaled input signal (light) and compensated output signal (dark) showing reduced sideband regrowth for traffic channel E_c/I_{or} between –18 and –16 dB. Network analyzer derived nonlinear characteristics.

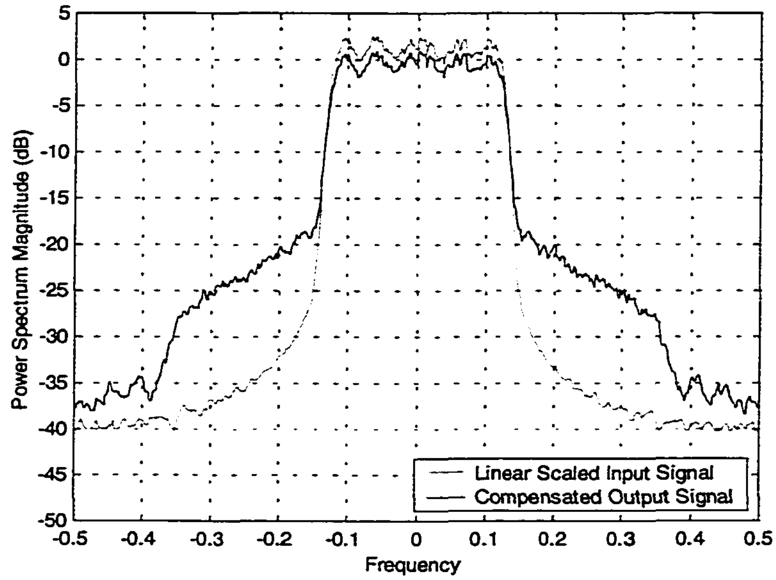

Fig. 92. PSD comparison between scaled input signal (light) and compensated output signal (dark) showing sideband regrowth for traffic channel E_c/I_{or} between –11 and –9 dB. Network analyzer derived nonlinear characteristics.

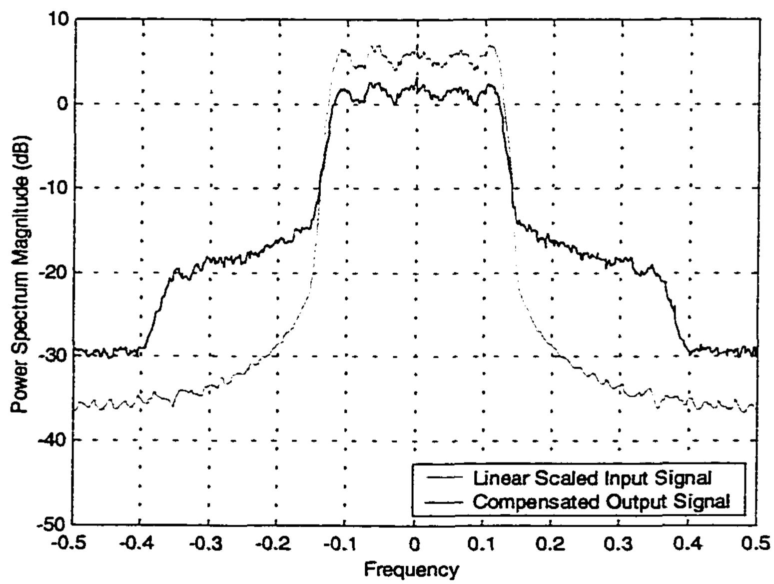

Fig. 93. PSD comparison between scaled input signal (light) and compensated output signal (dark) showing sideband regrowth for traffic channel E_c/I_{or} between –7 and –3 dB. Network analyzer derived nonlinear characteristics.

CHAPTER 5 CONCLUSIONS

The explosive growth in mobile wireless systems during the last decade has resulted in the need for spectrally efficient CDMA cellular telephone systems such as IS-95 and IS-2000. The ultimate objective of this research is the design of a compensator for the wideband HPAs used in such CDMA cellular telephone systems. This ultimate objective requires meeting three other objectives: deriving a simple yet accurate model of an HPA's nonlinear behavior, designing a compensator that incorporates this nonlinear model, and evaluating the compensator's performance using an IS-2000 forward link simulator. All of these objectives have been met.

The first nonlinear HPA model examined was the truncated Volterra series model. The Volterra series model is a memory model that provides a very good output signal approximation using just a few Volterra kernels but requires a special input signal to determine the model's parameters. The subjective nature of choosing the significant Volterra kernels is also a concern. The Volterra series model was abandoned in favor of the simpler envelope-phase model.

The memoryless envelope-phase model has only two parameters: the HPA's AM/AM conversion and AM/PM conversion. These two parameters are usually derived from a network analyzer using a CW power sweep and expressed by polynomial approximations. The envelope-phase model using network derived nonlinear characteristics is capable of producing a maximum error signal PSD magnitude about 20 dB down from that of the actual output signal. More accuracy was needed and deriving the HPA's AM/AM conversion and AM/PM conversion from its modulated input and output signals was a solution.

The HPA's modulated input and output signals are processed to produce scatter plot representations of its AM/AM conversion and AM/PM conversion. The envelope-phase model's two parameters are then found by fitting polynomial approximations to these scatter plot representations. The envelope-phase model has about a 10 dB improvement in the maximum error signal PSD magnitude using polynomial approximations of the HPA's AM/AM scatter plot and AM/PM scatter plot instead of its AM/AM conversion and AM/PM conversion derived from network analyzer measurements. The envelope-phase model is rather insensitive to the polynomial approximation order used for either the AM/AM conversion (scatter plot) or the AM/PM conversion (scatter plot) as long as reasonable values are used.

Examining an AM/AM scatter plot or AM/PM scatter plot shows the presence of hysteresis – a manifestation of the HPA's memory effects. The hysteresis effects can be taken into account if the HPA's AM/AM scatter plot and AM/PM scatter plot are characterized using a TDL model. The TDL model is an envelope-phase model utilizing a sum of polynomial approximations of the present input signal sample and previous input signal samples to characterize the HPA's AM/AM scatter plot and AM/PM scatter plot. The TDL model has about a 2 dB improvement in the maximum error signal PSD magnitude compared to the envelope-phase model. Current research to be reported in [24] indicates that the introduction of two linear filters into the TDL model results in about a 10 dB improvement in the maximum error signal PSD magnitude compared to the basic TDL model. The TDL model, either the basic or filtered version, is more accurate than the envelope-phase model and much more complex. Nevertheless, the envelope-phase model using scatter plot derived nonlinear characteristics was chosen to incorporate into the compensator and to model the IS-2000 forward link simulator's HPA for a variety of reasons including the model's execution speed.

A digital baseband predistorter based on the fixed point approach, the FPPD, was investigated for its ability to compensate CDMA signals. The FPPD reduces sideband regrowth by effectively reducing the HPA's gain while extending the linear region of its gain characteristic. The FPPD incorporates an envelope-phase model having nonlinear characteristics derived from either a network analyzer or the HPA's modulated input and output signals, i.e., using scatter plots. The FPPD's precursor described in [34] is non-adaptive because it relies on a static model of the HPA's nonlinear characteristics. Thus, its performance is only as good as the underlying nonlinear model. This shortcoming is remedied by having the envelope-phase model use the HPA's modulated input and output signals to derived the HPA's nonlinear characteristics. Consequently, the FPPD can adapt to changes in the HPA's nonlinear characteristics caused by environmental variables such as temperature fluctuations, component aging, and supply voltage fluctuations. The FPPD is capable of reducing sideband regrowth by more than 30 dB as compared to backing off the input signal until the compensated output signal and uncompensated output signal have the same power.

The FPPD's performance was evaluated using an IS-2000 forward link simulator. Simulations show that link performance is not degraded by the effective reduction in the

HPA's gain caused by the FPPD. Sideband regrowth is reduced at certain power levels however. The source of the FPPD's envelope-phase model's nonlinear characteristics affect sideband regrowth. Network analyzer derived nonlinear characteristics cause greater sideband regrowth than scatter plot derived nonlinear characteristics that more accurately represent an HPA's behavior when amplifying CDMA signals.

BIBLIOGRAPHY

[1] D. P. Whipple, "The CDMA standard," *Applied Microwave & Wireless*, vol. 6, pp. 24-37, Spring 1994.

[2] *ACOLADE IS-95-A/CDMA Library Overview*, ICUCOM Corporation, Troy, New York, 1996.

[3] S.-W. Chen, W. Panton, and R. Gilmore, "Effects of nonlinear distortion on CDMA communication systems," *IEEE Trans. Microwave Theory Tech.*, vol. 44, pp. 2743-2749, Dec. 1996.

[4] R. N. Braithwaite, "Nonlinear amplification of CDMA waveforms: an analysis of power amplifier gain errors and spectral regrowth," in *Proc. IEEE Veh. Technol. Conf.*, 1998, pp. 2160-2166.

[5] J. de Mingo and A. Valdovinos, "Amplifier linearization using a new digital predistorter for digital mobile radio systems," in *Proc. IEEE Veh. Technol. Conf.*, 1997, pp. 671-675.

[6] *Multi-Carrier Power Amplifiers for W-CDMA Wireless Systems*, Powerwave Technologies, Inc., Irvine, CA, 1998.

[7] A. A. M. Saleh, "Frequency-independent and frequency-dependent nonlinear models of TWT amplifiers," *IEEE Trans. Commun.*, vol. COM-29, pp. 1715-1720, Nov. 1981.

[8] A. R. Kaye, D. A. George, and M. J. Eric, "Analysis and compensation of bandpass nonlinearities for communications," *IEEE Trans. Commun.*, vol. COM-20, pp. 965-972, Oct. 1972.

[9] L. Sundström, *Digital RF Power Amplifier Linearisers - Analysis and Design*, Ph.D. Dissertation, Lund University, Sweden, 1995.

[10] M. Schetzen, "Nonlinear system modeling based on the Wiener theory," *Proc. IEEE*, vol. 69, pp. 1557-1573, Dec. 1981.

[11] S. Benedetto, E. Biglieri, and R. Daffara, "Modeling and performance evaluation of nonlinear satellite links – a Volterra series approach," *IEEE Trans. Aerosp. Electron. Syst.*, vol. AES-15, pp. 494-506, July 1979.

[12] K. Fazel and S. Kaiser, "Analysis of non-linear distortions on MC-CDMA," in *Proc. IEEE Int. Conf. Commun.*, 1998, pp. 1028-1034.

[13] R. Hermann, "Volterra modeling of digital magnetic saturation recording channels," *IEEE Trans. Mag.*, vol. 26, pp. 2125-2127, Sep. 1990.

[14] B. Lin, *Characterization and Modeling of Magnetic Recording Channels*, M.S. Thesis, The University of Oklahoma, Norman, Oklahoma, 1997.

[15] F. J. MacWilliams and N. J. A. Sloane, "Pseudo-random sequences and arrays," *Proc. IEEE*, vol. 64, pp. 1715-1729, Dec. 1976.

[16] N. M. Blachman, "Band-pass nonlinearities," *IEEE Trans. Inform. Theory*, vol. IT-10, pp. 162-164, Apr. 1964.

[17] N. M. Blachman, "Detectors, band-pass nonlinearities, and their optimization: inversion of the Chebyshev transform," *IEEE Trans. Inform. Theory*, vol. IT-17, pp. 398-404, July 1971.

[18] O. Shimbo, "Effects of intermodulation, AM-PM conversion, and additive noise in multicarrier TWT systems," *Proc. IEEE*, vol. 59, pp. 230-238, Feb. 1971.

[19] R. Blum and M. C. Jeruchim, "Modeling nonlinear amplifiers for communication simulation," in *Proc. IEEE Int. Conf. Commun.*, 1989, vol. 3, pp. 1468-1472.

[20] E. Kreyszig, *Advanced Engineering Mathematics*, 5th ed. New York: Wiley, 1983, ch. 19, p. 781.

[21] M. S. Heutmaker, J. R. Welch, and E. Wu, "Using digital modulation to measure and model RF amplifier distortion," *Applied Microwave & Wireless*, Mar. 1997, vol. 9, pp. 34-38.

[22] M. S. Heutmaker, E. Wu, and J. R. Welch, "Envelope distortion models with memory improve the prediction of spectral regrowth for some RF amplifiers," in *48th ARFTG Conf. Dig.*, Dec. 1996, pp. 10-15.

[23] M. S. Heutmaker, E. Wu, C. Herring, and J. R. Welch, "Using digitally-modulated signals to measure the gain compression and phase distortion of a radio frequency amplifier," in *46th ARFTG Conf. Dig.*, Nov. 1995, pp. 56-63.

[24] S. McBeath, *Modeling of Wideband CDMA Power Amplifiers*, M.S. Thesis, The University of Oklahoma, Norman, Oklahoma, 2001.

[25] K. Morris and P. Kenington, “A broadband linear power amplifier for software radio applications,” in *Proc. Veh. Technol. Conf.*, May 1998, vol. 3, pp. 2150-2154.

[26] J. K. Cavers, “Adaptation behavior of a feedforward amplifier linearizer” *IEEE Trans. Veh. Technol.*, vol. 44, pp. 31-40, Feb. 1995.

[27] J.-T. Chen, H.-S. Tsai, and Y.-K. Chen, “Fast adaptive wide-band power amplifier feed-forward linearizer,” in *Proc. Veh. Technol. Conf.*, May 1998, vol. 3, pp. 2167-2171.

[28] J. K. Cavers, “Amplifier linearization using a digital predistorter with fast adaptation and low memory requirements,” *IEEE Trans. Veh. Technol.*, vol. 39, pp. 374-382, Nov. 1990.

[29] A. S. Wright and W. G. Durtler, "Experimental performance of an adaptive digital linearized power amplifier," *IEEE Trans. Veh. Technol.*, vol. 41, pp. 395-400, Nov. 1992.

[30] J. K. Cavers, “The effect of quadrature modulator and demodulator errors on adaptive digital predistorters for amplifier linearization,” *IEEE Trans. Veh. Technol.*, vol. 46, pp. 456-466, May 1997.

[31] J. K. Cavers, “Optimum indexing in predistorting amplifier linearizers,” in *Proc. Veh. Technol. Conf.*, May 1997, vol. 2, pp. 676-680.

[32] J. K. Cavers, “Optimum table spacing in predistorting amplifier linearizers,” *IEEE Trans. Veh. Technol.*, vol. 48, pp. 1699-1705, Sep. 1999.

[33] W. G. Jeon, K. H. Chang, and Y. S. Cho, "An adaptive data predistorter for compensation of nonlinear distortion in OFDM systems," *IEEE Trans. Commun.*, vol. 45, pp. 1167-1171, Oct. 1997.

[34] M.-C. Kim, Y. Shin, and S. Im, “Compensation of nonlinear distortion using a predistorter based on the fixed point approach in OFDM systems” in *Proc. Veh. Technol. Conf.*, May 1998, vol. 3, pp. 2145-2149.

[35] K.-S. Jin, Y. Shin, and S. Im, “Compensation of nonlinear distortion with memory in multi-code CDMA systems” in *Proc. IEEE Int. Conf. Commun.*, 1999, vol. 1, pp. 565-569.

[36] C.-H. Tseng, *Advanced Nonlinear System Identification Techniques and Their Application to Engineering Problems*, Ph.D. Dissertation, The University of Texas at Austin, Texas, 1993.

[37] *Physical Layer Standard for cdma2000 Spread Spectrum Systems*, TIA/EIA/IS-2000.2 (Ballot Version), 1999.

[38] H. J. Xing, *Performance Evaluation of CDMA Systems*, Ph.D. Dissertation, The University of Oklahoma, Norman, Oklahoma, 2001.